Determination of proton- and neutron-induced cross sections for p-process studies

Construction of an online database for the p process

Inauguraldissertation

zur

Erlangung der Würde eines Doktors der Philosophie

vorgelegt der

Philosophisch-Naturwissenschaftlichen Fakultät
der Universität Basel

von

Iris Dillmann
aus Deutschland

Basel, 2006

Genehmigt von der Philosophisch-Naturwissenschaftlichen Fakultät
auf Antrag von

Prof. Dr. F.-K. Thielemann

PD Dr. T. Rauscher

Dr. F. Käppeler (Forschungszentrum Karlsruhe)

Basel, den 21.11.2006

Prof. Dr. H.-P. Hauri
Dekan

"The scientific theory I like best is that the rings of Saturn are composed entirely of lost airline luggage."

(Mark Russell, American political commentator, Comedian and Satirist)

Chapter 1

Abstract and Motivation

The nucleosynthesis of elements beyond iron is dominated by neutron captures in the s and r processes. However, 32 stable, proton-rich isotopes between ^{74}Se and ^{196}Hg cannot be formed in that way, because they are shielded from the s process flow and r process β-decay chains. These nuclei are thought to be produced in the so-called "p process", where proton-rich nuclei are made by sequences of photodisintegrations on existing r- and s-seed nuclei and following β^+ decays. Since the largest part of the p-process reaction network lies in the region of proton-rich unstable nuclei, most of the reaction rates are not yet accessible by experimental techniques and have to be inferred from statistical model calculations, e.g. by using the Hauser-Feshbach codes NON-SMOKER and MOST. The parametrization of these models has to be constrained by measurements on as many nuclei as possible.

However, the number of experimental data available for the p process is very scarce. For example, (γ, n) measurements were up to now mainly performed for 13 isotopes beyond ^{181}Ta, whereas the bulk of (p, γ) and (α, γ) reactions was only measured – with exception of ^{144}Sm(α, γ) – for isotopes up to Sn. The database for particle exchange reactions is much more extensive. In contrast to this, the database for the stellar (n, γ) cross sections of the 32 stable p isotopes is also surprisingly scarce. Before the measurements described in this thesis, 12 cross sections were not known experimentally, and further 9 exhibit uncertainties $\geq 9\%$. Thus, a series of (n, γ) activation measurements on stable p isotopes were carried out at the Karlsruhe Van de Graaff accelerator using the ^{7}Li$(p, n)^7$Be source for simulating a Maxwellian neutron distribution of $kT = 25$ keV. These studies included measurements of 7 total and 3 partial neutron capture cross sections of the stable isotopes ^{74}Se, ^{84}Sr, ^{102}Pd, ^{120}Te, ^{130}Ba, ^{132}Ba, and ^{174}Hf (see Chapter 4).

Chapter 5 is related to proton-induced reactions of palladium isotopes between 2.7 MeV$\leq$E$_p\leq$5 MeV, the energy range relevant for the p process. These measurements were performed using the cyclotron and Van de Graaff accelerator at the Physikalisch-Technische Bundesanstalt (PTB) in Braunschweig/ Germany. In these experiments we determined the total (p,γ) cross sections for ^{102,104}Pd, the total (p, n) cross section of ^{105}Pd, as well as the partial cross sections for ^{105}Pd(p, γ), ^{106}Pd(p, n), and ^{110}Pd(p, n).

Chapter 6 describes the update of the previous stellar neutron cross section compilation of Bao et al. from 2000 with recent measurements. The updated sequel to this compilation is available online and is part of the "Karlsruhe Astrophysical Database of Nucleosynthesis in Stars" (KADoNiS) project, which was started in April 2005 under http://nuclear-astrophysics.fzk.de/kadonis. In 2006 this project was extended with a first collection of experimental cross sections relevant for p-process studies. This part of KADoNiS is still under construction, but a first layout is given here.

The updated KADoNiS database for stellar neutron capture cross sections was further used in Chapter 7 for an update of the local version of a reaction rate library for astrophysics. Where available, this library already contained experimental rates, but neutron capture rates up to ^{81}Br were still based on the first Bao et al. compilation from 1987.

With the updated reaction library p-process network calculations were performed (Chapter 8) with the program "pProSim" to examine the influence of the new experimental neutron rates. Surprisingly the abundances of almost all p-process isotopes got smaller with the updated reaction library. This effect can be mainly traced back to much lower experimental cross sections of nuclei around the shell closures compared to previous NON-SMOKER calculations. It is well known that statistical model predictions cannot be applied here and tend to overpredict neutron cross sections. Since the s-process seed nuclei used for these simulations have larger abundances around the shell closures the influence of these decrease is global and the reaction flow to almost all p isotopes is affected. By comparing the abundance before and after the simulations we additionally realized that the isotopes ^{152}Gd, ^{164}Er, ^{113}In, and ^{115}Sn are destroyed rather than produced in our simulations. Together with possible different contributions from different astrophysical processes to the abundance of ^{180}Ta, it is possible that in future we might have to speak of only "30 p isotopes".

Contents

List of Figures

List of Tables

Chapter 2

Introduction

2.1 Stellar nucleosynthesis

Density waves lead to gravitational instabilities in the interstellar medium, following the formation of stellar progenitors, the so-called "proto-stars". The evolution and final fate of the star emerging from the proto-star depend on its initial mass. If the accumulated mass is less than 8 solar masses (M< 8 M$_\odot$), the fuel is only sufficient for the first two burning stages, hydrogen and helium burning. The latter phase is responsible for the formation of a carbon/oxygen core before the fusion ceases and the star finally ejects its outer layers as planetary nebula, leaving a hot and dense object as remnant which is called a "White Dwarf".

If the initial mass exceeds 8 solar masses (M> 8 M$_\odot$), further burning stages can be ignited, and the star finally ends in a Supernova type II explosion, which leaves as remnant either a neutron star or a black hole.

2.1.1 Stellar burning phases

When the proto-star contracts its temperature and density increases. If the temperature exceeds 5 MK "hydrogen burning" is ignited, in which in principle four protons are transformed into one helium nucleus. For a detailed discussion of the contributing reactions, see [1]. The two main reaction sequences are the "pp chain" and the "CNO" or "Bethe-Weizsäcker cycle", operating at different temperatures with different efficiencies. In our Sun with a core temperature of 15 MK, about 99% of the H is burnt by the pp chain and only 1% by the CNO cycle. At $T \approx$18 MK both mechanisms contribute in equal parts. Beyond that temperature the CNO cycle becomes more efficient. When the H fuel is almost completely consumed, the fusion reactions cease and the gravitational force becomes larger than the thermal pressure. The star contracts and "helium burning" starts to produce carbon and oxygen at core temperatures of 100-200 MK. The main mechanism in this stage is the "triple α reaction", in which three α particles fuse in a two-step reaction to ^{12}C to overcome the "mass-8 gap" (no stable isotope with A=8 exists, e.g. ^{8}Be has a

lifetime in the order of femtoseconds). About 50% of the ^{12}C is further processed by α capture into ^{16}O.

For stars with initial masses of less than 8 M$_\odot$, no more burning phases can be ignited, and the star ejects its outer layers as planetary nebula, and ends as a White Dwarf made of carbon and oxygen, the ashes from the previous He burning. For stars with an initial mass of >8 M$_\odot$, advanced burning stages take place, when the core temperature reaches 500 MK due to the repeated contraction. In "carbon burning" C is processed to Ne and Na via ^{12}C(^{12}C,α)^{20}Ne and ^{12}C(^{12}C,p)^{23}Na. The following "neon burning" phase ignites at 1 GK and first leads to photodisintegration of part of the Ne nuclei and liberates α particles via ^{20}Ne(γ, α)^{16}O. These α particles are captured again by the remaining ^{20}Ne nuclei and form ^{24}Mg. The next burning stage starts at 2 GK. Oxygen burning creates ^{28}Si via ^{16}O(^{16}O,α)^{28}Si. The last burning phase, Si burning, is ignited at 5 GK. High energy photons photodisintegrate the ^{28}Si seeds by ^{28}Si(γ, α)^{24}Mg. The liberated α particles build up heavier nuclei up to Fe and Ni by captures on the remaining ^{28}Si. At these high temperatures, photodissociations are in equilibrium with capture reactions ("nuclear statistical equilibrium", NSE). Thus single reactions are no longer important because the abundances depend only on the temperature and density of the plasma, the neutron-to-proton ratio, as well as on the binding energies of the respective nuclei. Since the nucleus with the highest binding energy is ^{56}Ni (Z=N=28), mainly ^{56}Ni and its stable decay product ^{56}Fe are formed.

2.1.2 Supernova type II explosions

The evolved star has now an onion-shell-like structure due to the different shell burning phases, with an Fe-Ni core surrounded by the unburnt left-overs in the outer layers. The gravitational force again exceeds the thermal pressure and the core shrinks. But since no more energy can be released in fusion processes, the contraction continues and the temperature increases. Fe nuclei are partially photodisintegrated into neutrons and protons, and electron capture on protons leads to formation of neutrons (inverse β-decay, $e+p \rightarrow n+\nu_e$). The neutrinos escape but more significant is the continuing decrease of electron pressure which further decreases the pressure counteracting the contraction and turns it into a collapse. The core collapses and the innermost regions reach nuclear matter density ($\rho \approx 10^{14}$ g cm^{-3}, $T \approx 100$ GK). At this point the collapse is halted because the equation-of-state (EOS) becomes stiff enough to balance its weight. Since the outer layers of the core are still collapsing, they are bounced back at this halted inner core and generate an outwardly directed shock front. This shock wave induces again explosive burning in the outer (C, Ne, O, Si) layers, modifying the ashes, and e.g. creating p-process nuclei by photo-induced reactions in the O/Ne layers .

This catastrophic event, called "Core Collapse Supernova explosion" (e.g. SN type II), leaves either a neutron star, or – if the inner core mass exceeds 3 M$_\odot$ – even a Black Hole.

2.1.3 Nucleosynthesis of heavy elements

The main products of the last hydrostatic burning stage are nuclei in the Fe-Ni region. During all burning stages nucleosynthesis beyond Fe by charged-particle reactions is hindered by the increasing Coulomb barriers. Thus for an efficient production of elements beyond Fe, reactions with neutral particles, i.e. neutrons, are required. Astrophysical models can explain the origin of most nuclei beyond the iron group in a combination of processes involving neutron captures on long (s process) or short (r process) time scales [2, 3]. Both processes contribute in about equal parts to the total elemental abundances beyond iron.

Historically, the s process was subdivided into a "weak" and a "main" component, corresponding to different mass region, temperatures and neutron exposures. The reaction flow proceeds along the valley of stability, by subsequent neutron captures and β-decays on the time scale of hundreds of years. The endpoint of the s process is ^{209}Bi, which produces by neutron capture ^{210}Bi, which decays into the α-instable ^{210}Po.

The weak s process is responsible for the production of elements with A <90. The neutrons are produced via the ^{22}Ne$(\alpha, n)^{25}$Mg reaction at T=200-300 MK. These conditions are reached in massive stars with core He and carbon shell burning. The main s process occurs during He shell flashes of low-mass TP-AGB stars ("thermally pulsing asymptotic giant branch" stars) and produces isotopes in the mass region $90 < A <$209. It is based on the neutron production via the ^{13}C$(\alpha, n)^{16}$O reaction, at lower temperatures compared to the weak component ($T \approx$100 MK) and low neutron densities of 10^7 cm^{-3}. When the maximum temperature of $T \approx$300 MK is reached towards the end of these He flashes, the second neutron source ^{22}Ne$(\alpha, n)^{25}$Mg becomes operational for a few years with peak neutron densities of 10^{10} cm^{-3}. However, the last reaction delivers only a small fraction of the neutrons and does not alter the abundance distribution.

The astrophysical site of the r process, the rapid neutron capture process, is still under debate. The most favoured site are regions in SNII explosions close to the forming neutron star but also neutron star mergers could provide the respective conditions. In the r process high neutron fluxes ($\gg 10^{20}$ s^{-1} cm^{-2}) are needed within less than a second to drive the reaction path from the Fe-Ni seeds deep into the neutron rich region. Similar to Si burning with its full NSE, an (γ, n)-(n, γ) equilibrium is reached in the r process, favoring nuclei with high binding energies (neutron separation energies). With the given high neutron-to-proton ratio, the favored nuclei are those with closed neutron shells (N=50, 82, 126), if such a shell appears within a given isotopic chain. The next higher Z chain is fed by β^- decay of the nuclei with the highest abundance and again a (γ, n)-(n, γ) equilibrium is established within it. The r-process path reaches up to the actinides in the U-Th region. During the following freeze-out about 50% of the stable elemental abundances are created by β-decay chains from the respective r-process progenitor isotopes.

2.1.4   The p process

However, 32 proton-rich stable isotopes between ^{74}Se and ^{196}Hg cannot be formed
in processes described above. They are thought to be produced in the so-called "γ
process", where proton-rich nuclei are made by sequences of photodissociations and
β^+ decays [4, 5, 6]. The p nuclei nuclei are 10 to 100 times less abundant than the s
and r nuclei in the same mass region (see Sec. 2.1.5). The astrophysical site of the
p process is also still under discussion, since up to now no astrophysical model can
explain the solar p abundances of all p nuclei within one scenario. They cannot be
produced in large amounts by the aforementioned neutron capture reactions since
they are either shielded by stable isotopes from the r-process decay chains or lie
outside the s-process flow.
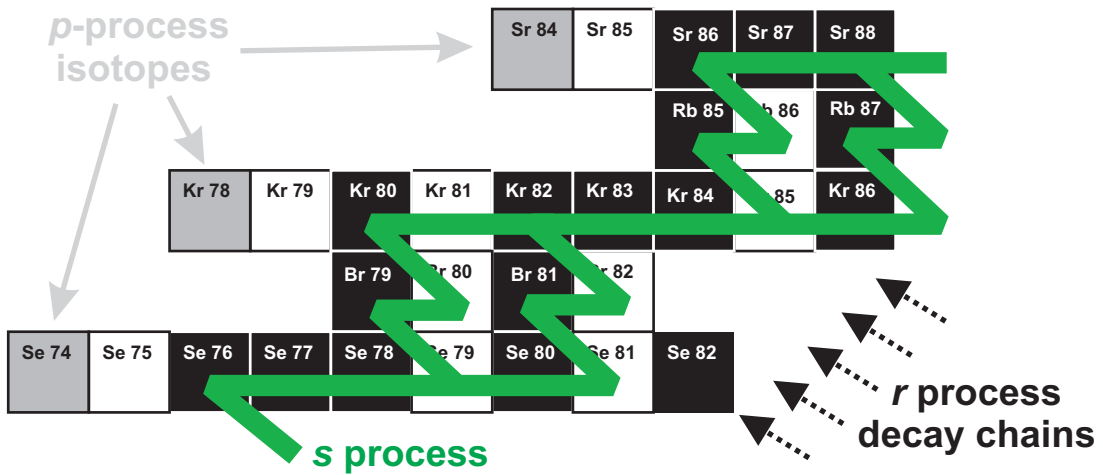
Figure 2.1: Example for the location of s, r and p isotopes. The p isotopes lie outside
s-process flow and are shielded from the r process β-decay chains by stable isotopes.

The currently most favored astrophysical site for the p process is explosive burning
in type II supernovae. The explosive shock front heats the outer O/Ne shell of
the progenitor star to temperatures of 2-3 GK, sufficient for providing the required
photodisintegrations. More massive stellar models (M$\geq$20 M$_\odot$) reach the required
temperatures for efficient photodisintegration already at the end of hydrostatic O/Ne
burning [7]. Historically, the p process was thought to proceed via proton captures,
but today they are found to play no role, since the required amount of free protons
is not available in these Ne and O layers within the p-process timescale of a few
seconds, and proton captures are too slow for elements with large Z. Now the
name "γ process" is more accurate, since pre-existing seed nuclei from the s and r
processes are photodissociated and proton-rich isotopes produced by (γ,n) reactions.
When (γ,p) and (γ,α) reactions become comparable or faster than neutron emission
within an isotopic chain, the reaction path branches out and feeds nuclei with lower
charge number Z (see Fig. 2.2). The decrease in temperature at later stages of the p
process leads to a freeze-out via neutron captures and mainly β^+ decays, resulting in
the typical p-process abundance pattern with maxima at ^{92}Mo (N=50) and ^{144}Sm

(N=82).
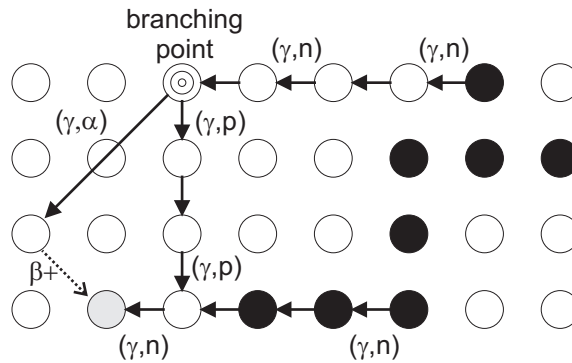
Figure 2.2: Favoured p-process mechanism via photodisintegrations.

2.1.5 Solar abundances

The solar abundances relative to Si=10^6 from Anders and Grevesse [8] and Lodders [9] are listed in Table 2.1 for each p isotope. Fig. 2.3 compares the abundances of s and r isotopes with these abundances. As can be seen, the p nuclei are about 2 orders of magnitude less abundant than the respective r and s nuclei in the same mass region, with exception of ^{92,94}Mo and ^{96,98}Ru. Not included in this list are ^{152}Gd, ^{164}Er and ^{180}Ta, which have s-process contributions $\geq$50% and thus are no pure p-process nuclei. The peaks belong to the neutron-magic (^{92}Mo: N=50, ^{144}Sm: N=82) p isotopes. All p isotopes are even-even nuclei, with exception of ^{113}In (Z=49), ^{115}Sn (N=65), ^{138}La (Z=57, N=81), and ^{180}Ta (Z=73, N=107).

Table 2.1: Solar p abundances (relative to Si$= 10^6$) from Anders and Grevesse [8] and Lodders [9]. * New values from [10]: ^{124}Xe: 6.57×10^{-3}; ^{126}Xe: 5.85×10^{-3}.

Isotope	Lodders (2003)	Anders/Grevesse (1989)	Change [%]
Se-74	5.800×10^{-1}	5.500×10^{-1}	5.2
Kr-78	2.000×10^{-1}	1.530×10^{-1}	23.5
Sr-84	1.312×10^{-1}	1.320×10^{-1}	-0.6
Mo-92	3.860×10^{-1}	3.780×10^{-1}	2.1
Mo-94	2.410×10^{-1}	2.360×10^{-1}	2.1
Ru-96	1.053×10^{-1}	1.030×10^{-1}	2.2
Ru-98	3.550×10^{-2}	3.500×10^{-2}	1.4
Pd-102	1.460×10^{-2}	1.420×10^{-2}	2.7
Cd-106	1.980×10^{-2}	2.010×10^{-2}	-1.5
Cd-108	1.410×10^{-2}	1.430×10^{-2}	-1.4
Sn-112	3.625×10^{-2}	3.720×10^{-2}	-2.6
In-113	7.800×10^{-3}	7.900×10^{-3}	-1.3
Sn-114	2.460×10^{-2}	2.520×10^{-2}	-2.4
Sn-115	1.265×10^{-2}	1.290×10^{-2}	-2.0
Te-120	4.600×10^{-3}	4.300×10^{-3}	6.5
Xe-124	$6.940\times10^{-3}*$	5.710×10^{-3}	17.7
Xe-126	$6.020\times10^{-3}*$	5.090×10^{-3}	15.4
Ba-130	4.600×10^{-3}	4.760×10^{-3}	-3.5
Ba-132	4.400×10^{-3}	4.530×10^{-3}	-3.0
Ce-136	2.170×10^{-3}	2.160×10^{-3}	0.5
La-138	3.970×10^{-4}	4.090×10^{-4}	-3.0
Ce-138	2.930×10^{-3}	2.840×10^{-3}	3.1
Sm-144	7.810×10^{-3}	8.000×10^{-3}	-2.4
Dy-156	2.160×10^{-4}	2.210×10^{-4}	-2.3
Dy-158	3.710×10^{-4}	3.780×10^{-4}	-1.9
Er-162	3.500×10^{-4}	3.510×10^{-4}	-0.3
Yb-168	3.230×10^{-4}	3.220×10^{-4}	0.3
Hf-174	2.750×10^{-4}	2.490×10^{-4}	9.5
W-180	1.530×10^{-4}	1.730×10^{-4}	-13.1
Os-184	1.330×10^{-4}	1.220×10^{-4}	8.3
Pt-190	1.850×10^{-4}	1.700×10^{-4}	8.1
Hg-196	6.300×10^{-4}	4.800×10^{-4}	23.8
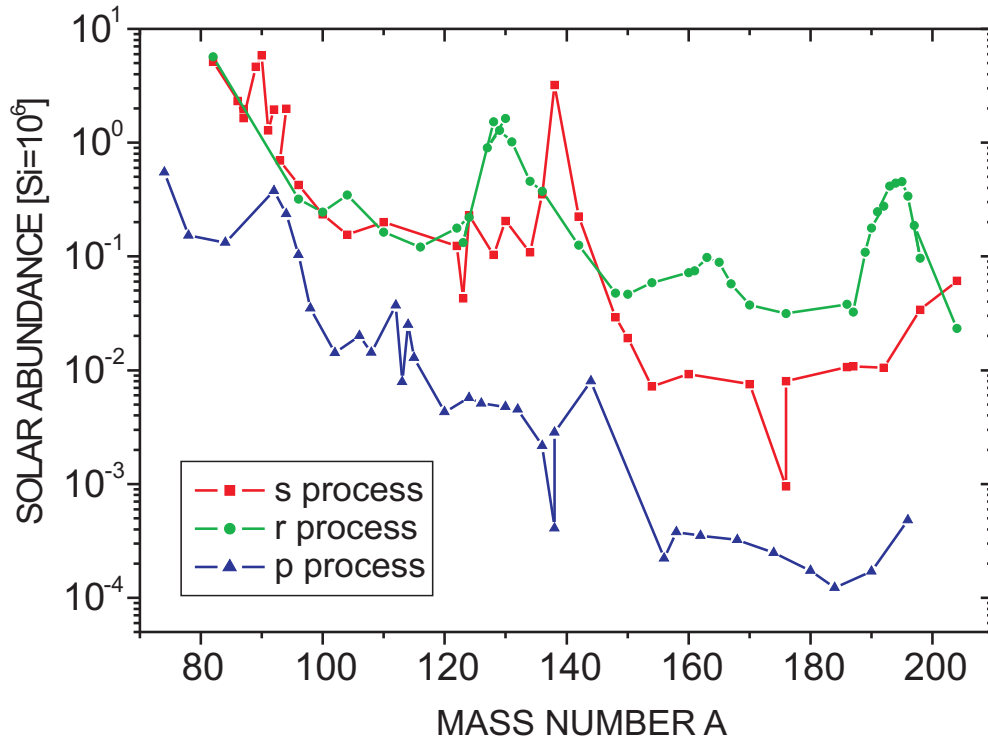
Figure 2.3: Solar abundances from Anders and Grevesse [8].

2.2   The p-process "puzzles"

Despite all efforts in the last years, no p-process model can reproduce the solar abundances in one single astrophysical scenario – as can be seen in the derived overproduction factors (Eq. 8.2) in Chapter 8. These factors should be equal to unity if the abundances correspond to the respective solar abundances. Following the nucleosynthesis as described before in pre-explosive or explosive O/Ne burning, good agreement within a factor of 2-3 for the bulk of p nuclei with the solar p abundances is found (Fig. 2.4), with exception of the low ($A <$100) and intermediate ($150 \leq A \leq 165$) mass range, which are underproduced by factors of 3-4 [6, 31, 7].

The light p nuclei ^{74}Se, ^{78}Kr, ^{84}Sr, ^{92,94}Mo, and ^{96,98}Ru are obviously underproduced due to a lack of corresponding s-process seeds with $A \geq$90. This is a major problem of the aforementioned p-process model, since the Mo and Ru isotopes with isotopic abundances between 2 and 15% determine the largest fraction of all p isotopes.

The second problem concerns the production of two of the rarest isotopes in the solar system, the odd-odd nuclei ^{138}La and ^{180}Ta^{m}. ^{138}La is the only isotope which cannot be produced – even in minor amounts – by neutron captures and is thus said to be a "pure p nucleus". It is thought to be underproduced due to the unfavorable interplay between its production (^{139}La$(\gamma, n)^{138}$La) and destruction channel (^{138}La$(\gamma, n)^{137}$La). Since up to now no experimental information on either the neutron capture or the photodisintegration exists, the predicted yields have to rely en-
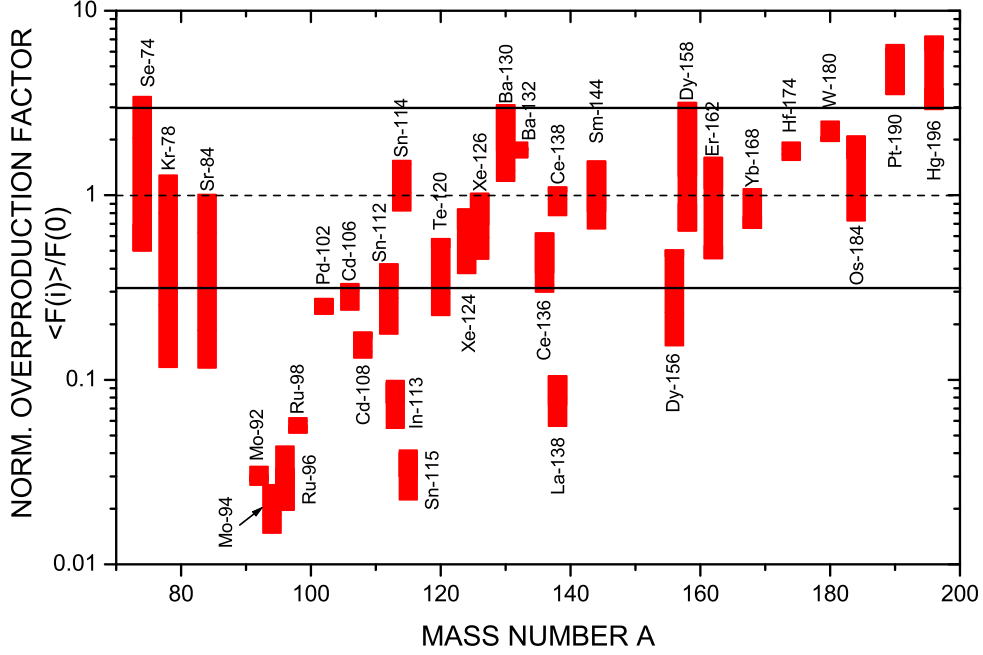
Figure 2.4: Example for ranges of variations of the normalized overproduction factors for p-process layers in different SN II models (13-25 $M_\odot$) with explosive O/Ne burning [6, 31].

tirely on theoretical calculations. The question arises whether this problem is due to inadequate astrophysical modelling or nuclear physics input. The latter could only be investigated when an appropriate enriched sample of ^{138}La becomes available for experiments (for further discussion, see also Chapter 9). However, since its solar abundance cannot be reproduced by the p process alone, alternative scenarios involving neutrinos during core collapse supernovae have been proposed [11, 12, 13, 14]. Woosley et al. [12] were able to overproduce the solar ^{138}La/^{139}La ratio by a factor of 50 with the "ν process". The parent nuclei, e.g. ^{139}La for neutral current reactions or ^{138}Ba for charged current reactions, are excited by elastic scattering of highly energetic neutrinos, and decay into the daughter nucleus (^{138}La). In [14] it was noted that for ^{138}La the neutral current reaction is insignificant and the respective charged current reaction on ^{138}Ba dominates. But here the key problem is the necessary enhancement of ^{138}Ba seed nuclei by a prior s-processing.

In the case of ^{180}Ta the charged-current ν-process produces 50% of the abundance whereas the other half is split between the γ process and the neutral current flux. The main problem here is the fact that these calculations do not distinguish between the 9^- isomeric state and the 1^+ ground state but that the solar abundance corresponds to the long-lived, quasi-stable ($t_{1/2} \geq 10^{15}$ y) ^{180}Ta^m and not to the

8.15 h ground state. However, the main problem of the ν process is the uncertainty in the neutrino cross sections. Additionally, it should be noted that ^{180}Ta^m has an s-process contribution of $\geq$50% (like ^{152}Gd and ^{164}Er) and is normally not regarded as a p nucleus.

2.2.1 Alternative p-process scenarios

Because of all these persisting problems, alternative scenarios for the site of the p process have been suggested, each with their own, inherent difficulties [11, 15, 16]. An enhancement of s-process seeds due to a prior "weak" s processing by He-shell flashes would only increase the seeds up to $A\approx$80, insufficient to produce light p nuclei up to A=100.

Howard and Meyer [15] tried to solve these deficiencies with a modified SNIa explosion. SNIa occur in binary systems when a White Dwarf accretes material from an accompanying Red Giant star, until it reaches the "Chandrasekhar limit" of 1.4 M$_\odot$. Then a thermonuclear detonation is ignited, disrupting the White Dwarf. According to the proposal, the accreted layer could be highly enriched (10^3-10^4 above solar) in s-process nuclei acting as seeds for a subsequent γ process due to He-shell flashes in the companion star. However, the thermonuclear runaway provides the temperatures conditions necessary for the γ process only in the carbon burning zones whereas in all other layers the temperatures are too low. Another deficiency of this SNIa model is that predicted yields depend strongly on the accretion rate of the White Dwarf, which has not been calculated self-consistently up to now. Howard et al. additionally claimed that a high proton abundance is created from carbon burning (^{12}C(^{12}C,p)^{23}Na) which can induce (p,γ) reactions near N=50 at T= 2-3 GK. In this way, they produce 50% of ^{92}Mo by successive proton captures on ^{86}Kr. The other half of ^{92}Mo should be produced by (γ,n) of ^{98}Mo. Despite the s-process seed enhancement, the SNIa model cannot solve the underproduction of Mo and Ru isotopes neither those of ^{138}La and ^{180}Ta^m. Another problem is that SNII explosions seem to occur six times more often than SNIa explosions and thus a much higher mass fraction of p nuclei would have to be ejected in each event.

Another attempt has been made via the rp process in X-ray bursts [16], which – like SNIa explosions – occur in binary, cataclysmic systems but with a neutron star and a Red Giant. The neutron star accretes material from its companion and burns it explosively. Due to the large gravitational potential on the surface of a neutron star, densities of $\rho\geq$10^6 g cm^{-3} can produce temperatures up to 2 GK, sufficient to ignite explosive hydrogen burning and run the rp path along the proton dripline. The endpoint of the rp process lies in the Sn-Sb-Te region ($A\approx$107) [17] where the radioactive proton-rich progenitors of the lightest p nuclei are located. The major problem of this scenario is the question whether the required amounts of material to reproduce the solar p abundances can be ejected into the interstellar medium, since the explosion energy of X-ray bursts is much smaller than the gravitational binding energy of the neutron star.

The theoretically predicted Thorne-Zytkow objects [18] can be excluded from the list of possible sites for the p process since they are found to be unlikely to form due

to their gravitational instability.

A very recent model [19] introduces a new possible p-process scenario to produce light p nuclei. This "νp process" can occur in core-collapse supernovae or γ-ray bursts. Here, strong neutrino fluxes can create proton-rich ejecta via ν_e+n $\rightleftharpoons$ p+e$^-$ and $\bar{\nu}_e$+p $\rightleftharpoons$ n+e$^+$. Due to the smaller mass of the proton, these equilibria are shifted towards the proton side. When this proton-rich matter expands and cools, mainly nuclei with $N=Z$ (e.g. ^{56}Ni, α particles and protons) are formed. Without further consideration of neutrino interactions and captures, the reaction flow is stopped at the rp-process waiting-point ^{64}Ge because its β-decay half-life ($t_{1/2}=$ 64 s) is much longer than the expansion time-scale of $\approx$10 s. The production of isotopes beyond that waiting-point is only possible by inclusion of (anti-)neutrino interactions. Antineutrino capture on the dominant, free protons create free neutrons with densities of $\rho_n=10^{14}$-10^{15} cm^{-3} for several seconds at T=1-3 GK. These neutrons are now predominantly captured by the proton-rich (neutron-deficient) nuclei which exhibit large neutron capture cross sections. With this mechanism the bottle neck at the waiting-point ^{64}Ge can be bypassed by (n,p) reactions, which are faster than the respective β-decay timescale. The production of light p nuclei is proportional to the electron abundance Y_e. Fig. 3 in [19] shows that nuclei with A>64 are only produced at Y_e> 0.5 and shows a strong dependence within a Y_e window of 0.5-0.6. The higher the Y_e, the higher the production of p nuclei up to Cd.

2.2.2 Nuclear physics input

However, it is not yet clear whether the observed underproductions are due to a problem with astrophysical models or with the nuclear physics input, i.e. reaction rates. Thus, a necessary requirement towards a consistent understanding of the p process is the reduction of uncertainties in nuclear data. By far most of the several hundreds of required photodisintegration rates and their inverses need to be inferred from Hauser-Feshbach statistical model calculations [20] using the codes NON-SMOKER [21, 22, 23] and MOST [24, 25]. Experimental data can improve the situation in two ways, either by directly replacing predictions with measured cross sections in the relevant energy range or by testing the reliability of predictions at other energies when the relevant energy range is not experimentally accessible.

This Ph.D. work aims at removing some of these uncertainties by replacing theoretical cross section predictions with new experimental results (Chapter 6). For the moment, this has only been done for (n,γ) reactions (and their respective inverse (γ,n) channels). In a second step, these new results are used to carry out p-process simulations and to compare the impact of the new experimental values with the previous dataset (Chapter 8).

Section 6.2.2 gives an overview of reactions in or close to the respective p-process energy window. As can be seen, most of these reactions originate from measurements performed within the last 10 years but the total number compared to the extent of a p-process network is still very scarce. For example, up to now (γ,n) measurements for p-process studies were mainly performed for 13 isotopes beyond ^{181}Ta, whereas

the bulk of (p, γ) and (α, γ) reaction studies is concentrated – with exception of ^{144}Sm(α, γ) – in isotopes up to Sn. The database for particle exchange reactions (e.g. (p, n), (α, n)) is much more extensive.

In contrast to this, the database for the (n, γ) cross sections of the 32 stable p isotopes measured at kT= 30 keV [26] is also surprisingly scarce. However, since we are not able to measure these neutron capture cross sections with our experimental neutron source (see Sec. 3.1) directly at p-process energies, we have to extrapolate our results by means of theoretical predictions (see Sec. 4.2).

2.3 Basic expressions in Nuclear Astrophysics

2.3.1 Hauser-Feshbach theory

The statistical model can be applied for determining nuclear cross sections in those energy regions where the average resonance width $<\Gamma>$ becomes larger than the average level spacing D=$1/\rho$ [27]. This region of compound nucleus reactions can be calculated in a statistical model using average resonance properties ("Hauser-Feshbach approach" [20]). Since charged-particle reactions relevant for astrophysical applications occur at higher particle energies (within the Gamow peak) than neutron induced reactions and the number of states increases exponentially with excitation energy, the statistical model can be easily applied here. The accuracy of the statistical model code NON-SMOKER [22] is within a factor of 2 for charged-particle reactions, and ≈ 1.4 for neutron-capture cross sections.

Direct reactions can dominate the cross sections at very high projectile energies (E$\geq$20 MeV), when the formation of a compound nucleus is suppressed due to the short time-scale. However, direct capture plays also a role at low energies for light nuclei with low level densities and isotopes with low particle separation energies. The latter case occurs for very neutron- (r process) or proton-rich (rp process) nuclei close to the driplines. For neutron induced reactions the statistical model can only be used when the Q value or the level density is sufficiently high. This holds for intermediate and heavy nuclei close to stability, with exception of neutron-magic isotopes which exhibit a wider level spacing. If the level density becomes too low, the consequence is an overestimation of the cross section with the statistical model. The recommended limit are 10 available levels (narrow, non-overlapping resonances) within the effective energy window (e.g. 10 MeV^{-1}) [28] to achieve an accuracy of 20% . In the case of s-wave neutron resonances, a smaller number of resonances can be already sufficient, since these resonances are usually broader.

The statistical model is based on the Bohr independence hypothesis [29] which states that the projectile forms a compound nucleus (CN) in the reaction $i^\mu(j, o)f^\nu$ with the target i and shares the energy among all the nucleons. The final decay of the compound nucleus into the product nucleus f is assumed to be independent of the formation but respecting the conservation laws (energy, angular momentum, parity, nucleon number):

$$\sigma_{CN}^{if} = \sigma_{form}^i \ b_{dec} = \sigma_{form}^i \ \frac{\Gamma^f}{\Gamma^{tot}}. \tag{2.1}$$

In this equation σ^i_{form} is the formation cross section, b_{dec} the branching ratio (how much decays from the entrance channel i into the exit channel f), and Γ^{tot} the total width ($=\Gamma^i + \Gamma^f +...$). σ^i_{form} is calculated in the optical model but with an average transmission coefficient $<T>$, which is connected to the average level density ρ via $<T>=2\pi\rho<\Gamma>$. Analogous to the Breit-Wigner formula but by replacing resonance parameters with average quantities, one gets (for $i=$ target and $j=$ projectile)

$$\sigma^{\mu\nu}_{CN}(E_{if}) = \frac{\pi \; \hbar^2}{2\mu_{if} \; E_{if}} \; \frac{1}{(2J^\mu_i + 1)(2J_f + 1)} \; \sum_{J\pi}(2J+1) \; \frac{< T^\mu_j >< T^\nu_f >}{< T_{tot} >} \; W^{if}. \quad (2.2)$$

With $<T_{tot}>=\sum_{\nu,f}<T^\nu_f>$, the transmission into all possible (bound and unbound) states ν in the product nucleus. The Hauser-Feshbach cross section σ^{if}_{CN} is equal to the averaged Breit-Wigner cross section $<\sigma_{BW}>$, when the width fluctuation coefficient W^{if} is 1. This factor

$$W^{if}(E, J, \pi) = \Big\langle \frac{\Gamma^i_{J,\pi}(E) \; \Gamma^f_{J,\pi}(E)}{\Gamma^{tot}_{J,\pi}(E)} \Big\rangle \quad (2.3)$$

describes non-statistical correlations between the width in the channels i and f. It differs from unity close to channel openings and enhances the weaker channel and can cause deviations from the "normal" trend in the reaction rate and cross section curves.

As can be seen, the average transmission coefficient $<T>$ is the key quantity in the statistical model. It describes the absorption via an imaginary part of the optical nucleon-nucleon potential.

2.3.2   Reaction rates and Maxwellian averaged cross sections

Experiments measure only the cross section $\sigma^{lab} = \sum_\nu \sigma^{0\nu}(E_{if})$, from the target being in the ground state ($E^\mu_i=0$) into all excited states E^ν_f in the product nucleus. In an astrophysical environment with temperature T interacting particles are quickly thermalized by collisions in the stellar plasma, and the respective energy distribution can be described by a Maxwell-Boltzmann velocity distribution having its maximum value at the energy kT.

For astrophysical applications, the laboratory cross section σ^{lab} has to be converted to the stellar cross section σ^* involving thermally excited targets by applying a correction factor, the so-called "stellar enhancement factor" $SEF(T) = \frac{\sigma^*}{\sigma^{lab}}$. The stellar cross section $\sigma^*=\sum_\mu \sum_\nu \sigma^{\mu\nu}$ accounts for all transitions from excited target states μ to final states ν in thermally equilibrated nuclei, whereas the laboratory cross section $\sigma^{lab}=\sum_0 \sum_\nu \sigma^{0\nu}$ includes only captures from the target ground state. These factors are tabulated, e.g. in Refs. [22, 23, 26]. While there are only comparatively few cases with low-lying nuclear states in the s process where the correction is important, the SEF can be larger at the much higher p-process temperatures. This is illustrated in Tables 4.3 and 4.4.

The stellar cross section of the reaction $i^\mu(j,o)f^\nu$ from the target state i^μ to the excited state f^ν is given by

$$\sigma^*(E_{if}) = \frac{\sum_\mu (2J_i^\mu + 1)\ exp(-E_i^\mu/kT)\ \sum_\nu \sigma^{\mu\nu}(E_{if})}{\sum_\mu (2J_i^\mu + 1)\ exp(-E_i^\mu/kT)}. \tag{2.4}$$

The summation over the excited states ν replaces $<T_f^\nu>$ by $<T_f>$:

$$< T_f >= \sum_{\nu_0}^{\nu_f} < T_f^\nu > \ \ + \ \int_{E_f}^{E-S_{f,o}} \sum_{J,\pi} T_o\ \rho\ dE_f \tag{2.5}$$

$S_{f,o}$ being the channel separation energy and the experimentally known states from ν_0 to ν_f. The summation over excited states beyond the last experimentally known state ν_f is replaced by the integration over the level density $\rho = \rho(E_f, J_f, \pi_f)$. Different statistical models differ due to different (particle- and γ-) transmission coefficients T and the respective level densities.

The reaction rate per particle pair is derived by folding σ^* from Eq. 2.4 with the Maxwell-Boltzmann velocity distribution:

$$< \sigma^* v >= \sqrt{\frac{8}{\pi\mu}}\ \frac{1}{(kT)^{3/2}}\ \int_0^\infty \sigma(E)\ E\ exp(-\frac{E}{kT})\ dE. \tag{2.6}$$

$< \sigma^* v >$ is a constant for s-wave neutron captures and it is then appropriate to measure the cross section at one single energy. However, with increasing neutron energy, neutron partial waves with higher angular momentum ($l_n > 0$) contribute to the reaction rate. By multiplication of Eq. 2.6 with the Avogadro constant N_A and using appropriate units the stellar reaction rate in the usual units of $[cm^3\ s^{-1}\ mole^{-1}]$ is obtained.

For neutron captures an averaged cross section over the respective Maxwellian distribution is often given instead of a cross section. This "Maxwellian averaged cross section" (MACS) is defined by

$$< \sigma >_{kT} = \frac{2}{\sqrt{\pi}}\ \frac{1}{(kT)^2}\ \int_0^\infty \sigma(E)\ E\ exp(-\frac{E}{kT})\ dE. \tag{2.7}$$

Applying detailed balance, the respective inverse rate (e.g. (γ, n)) can be determined from the stellar (n, γ) rate (j=n) by

$$N_A < \sigma^* v >_{\gamma,n} = \frac{(2J_i + 1)(2J_n + 1)}{2J_f + 1}\ \sqrt{\left(\frac{A_i}{A_f}\right)^3}\ \times$$

$$\times\ \frac{G_i(T)}{G_f(T)}\ exp\left(-\frac{Q_{n,\gamma}}{kT}\right) N_A < \sigma^* v >_{n,\gamma} \tag{2.8}$$

with the Avogadro number N_A, nuclear spins J, mass numbers A, temperature-dependent partition functions $G(T)$, and the reaction Q value in the exponent. Measuring or calculating a rate in the direction of positive Q value ensures best numerical accuracy and consistency between forward and backward reaction. This is important when implementing those rates in reaction networks for nucleosynthesis models.

2.3.3 Gamow energy and Gamow window for charged-particle reactions

For charged-particle reactions – compared to neutron-induced reactions – higher energies and temperatures are required to overcome the repulsive Coulomb barrier [1]:

$$V_c(r) = \frac{Z_{targ}Z_{proj}\ e^2}{r}. \tag{2.9}$$

In the understanding of classical mechanics, no reaction can occur for E<E_c. With the inclusion of quantum mechanical tunneling through the Coulomb barrier (barrier penetration or tunnel effect), one can introduce the tunneling probability

$$P = exp(-2\pi\eta) = exp(-2\pi\frac{Z_{targ}Z_{proj}\ e^2}{\hbar v}) \tag{2.10}$$

with the Sommerfeld parameter η. The exponent can be approximated in numerical units by

$$2\pi\eta = 31.29\ Z_{targ}Z_{proj}\ \sqrt{\frac{\mu}{E_{c.m.}}}. \tag{2.11}$$

The center-of-mass energy $E_{c.m.}$ is in $[keV]$ and the reduced mass μ in [amu] (atomic mass units). The tunneling probability P is proportional to the cross section, hence $\sigma(E) \propto$ exp($-2\pi\eta$), and the cross section drops rapidly for E<E_c. σ(E) can also be written with the de Broglie wavelength as $\sigma(E) \propto \pi(\frac{\lambda}{2\pi})^2 \propto \frac{1}{E}$. Therefore it can be advantageous to write the cross section as

$$\sigma(E) = \frac{1}{E}\ exp(-2\pi\eta)\ S(E). \tag{2.12}$$

Here, $S(E)$ is called the "astrophysical S factor" (in units of $[keV\ barn]$) and contains all nuclear effects. For non-resonant reactions, $S(E)$ is a smoothly varying function of energy and can be used for extrapolations to astrophysical energies. If Eq. 2.12 is inserted in Eq. 2.6, one obtains

$$< \sigma v > = \sqrt{\frac{8}{\pi\mu}}\ \frac{1}{kT^{3/2}}\ \int_0^\infty S(E)\ exp(-\frac{E}{kT} - \frac{b}{\sqrt{E}})\ dE. \tag{2.13}$$

The factor b is given by

$$b = \frac{\sqrt{2\mu}\ \pi\ e^2\ Z_{targ}Z_{proj}}{\hbar} = 0.989\ Z_{targ}Z_{proj}\ \sqrt{\mu} \tag{2.14}$$

in units of [MeV$^{1/2}$]. b^2 is also called the "Gamow energy", E_G. The term $exp(-\frac{E}{kT})$ in Eq. 2.13 corresponds to a Maxwell-Boltzmann distribution, which vanishes at high energies, whereas $exp(-\frac{b}{\sqrt{E}})$ describes the penetration through the Coulomb barrier, which becomes very small at low energies. The superposition of the two terms leads to a peak with a maximum at the energy E_0, the so-called "Gamow peak" (see Fig. 2.5).
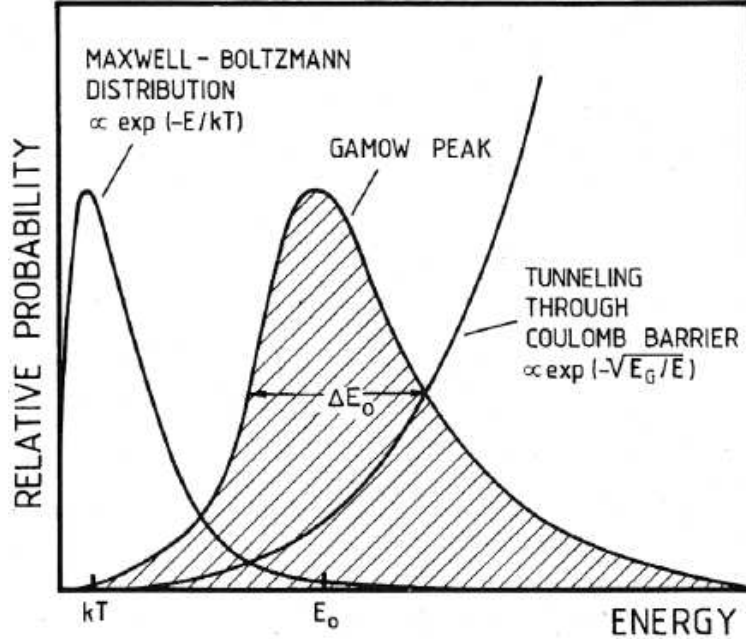
Figure 2.5: Schematic picture of the Gamow peak, in which most astrophysical reactions occur. The Gamow peak originates from a superposition of the Maxwell-Boltzmann distribution and the increasing probability of barrier penetration with higher energies. Picture taken from [1].

With the assumption that the S factor is constant within the Gamow window, it can be pulled out of the integral. Then, by taking the first derivative of the integrand, the effective mean energy E_0, the maximum of the Gamow peak, can be extracted:

$$E_0[keV] = (\frac{bkT}{2})^{2/3} = 1.22 \; (Z_{targ}^2 \; Z_{proj}^2 \; \mu \; T_6^2)^{1/3}. \tag{2.15}$$

The exponential term in Eq. 2.13 can be approximated with a Gaussian function:

$$exp(-\frac{E}{kT} - \frac{b}{\sqrt{E}}) = I_{max} \; exp[-(\frac{E - E_0}{\Delta/2})^2]. \tag{2.16}$$

I_{max} denotes the maximum value of the integrand of Eq. 2.13 and can be calculated by

$$I_{max} = exp(-\frac{3E_0}{kT}). \tag{2.17}$$

The effective width Δ of the Gamow window is the region, where most of the reactions take place:

$$\Delta[keV] = 4 \; \sqrt{\frac{E_0 \; kT}{3}} = 0.749 \; (Z_{targ}^2 \; Z_{proj}^2 \; \mu \; T_6^5)^{1/6}. \tag{2.18}$$

With these terms, the reaction rate can be approximated by

$$< \sigma v >= \sqrt{\frac{2}{\mu}} \; \frac{\Delta}{kT^{3/2}} \; S(E_0) \; exp(-\frac{3E_0}{kT} . -\frac{b}{\sqrt{E}}) \; dE. \tag{2.19}$$

If the S factor is a slowly varying function of energy within the energy window E_0, it can be described with a Taylor series:

$$S(E) = S \; \frac{dS}{dE}E + \frac{d^2S}{dE^2}E^2 + ... \tag{2.20}$$

Inserting this in Eq. 2.13, after some transformations (see [1]) one arrives at an S factor with a temperature dependence:

$$S(E_0) = S \sum_{n=0}^{5} \; a_n \; T^{n/3}. \tag{2.21}$$

In the same way the reaction rate can also be expressed in terms of the temperature:

$$< \sigma v >= A \; T^{-2/3} \; exp(-B \; T^{-1/3}) \sum_{n=0}^{5} \; a_n \; T^{n/3}. \tag{2.22}$$

This corresponds to the widespread parametrized form for reaction rate fits, as e.g. used in reaction libraries [30] (see Sec. 7).

For the stellar temperature T, nuclear reactions occur predominantly in a narrow energy window $E_0 \pm \Delta/2$. However, it has to be emphasized, that the abovementioned numerical solutions are only approximations, which are satisfactory for a first localization and width of the Gamow window. Since the real shape of the Gamow peak is asymmetric towards higher energies (see Fig. 2.5), it differs from the estimated Gaussian shape. For light nuclei good agreement is found but towards heavier nuclei rather large deviations are possible due to the contribution of higher partial waves. Thus, an exact calculation including the experimental cross sections is preferrable.

2.4 p-process network calculations

As an example for a p-process reaction network calculation and for comparison with the network calculations performed in Chapter 8, the model of Rayet et al. [31] is discussed in detail in the following. In this study, a parametrized explosion model was used to investigate the synthesis of p nuclei in oxygen burning layers of massive exploding stars. This network includes elements between carbon (Z=6) and bismuth (Z=83) and treats self-consistently the neutron-, proton-, and α-particle production and captures. The seed nuclei distribution corresponds to an s-process production in the He burning core of a massive star. One focus of these calculations was also set on the influence of neutron-induced reactions on the p-process yields. However, this study is not able to solve the enigma of the underproduction of the most abundant p nuclei ^{92}Mo, ^{94}Mo and ^{96}Ru.

2.4.1 Temperature and density profiles

Rayet et al. assume that the explosion can be simulated by a sudden adiabatic expansion to a peak temperature T_{max} and peak density ρ_{max} with following exponential decrease. This behavior can be described by

$$T(t) = T_{max} \, exp(-\frac{t}{3 \, \tau_{ex}}) \tag{2.23}$$

$$\rho(t) = \rho_{max} \, exp(-\frac{t}{\tau_{ex}}), \tag{2.24}$$

with τ_{ex} being the expansion timescale. The factor 3 in the denominator is derived from the polytropic index $n = 3$. For stars with convection which exhibit an adiabatic density-temperature structure (entropy S=constant) applies $T = T(\rho)$ and $P = P(\rho)$. The equation-of-state (EOS) for a relativistic, completely degenerated Fermi gas is

$$P = K \cdot \rho^{4/3}, \tag{2.25}$$

with the polytropic exponent $\Gamma = 1 + \frac{1}{n} = 4/3$ and the polytropic index $n=3$. K is the polytropic constant. Thus for a given star the relation between central temperature and central density is

$$T_c \propto \rho_c^{1/3}, \tag{2.26}$$

The investigated range of peak temperatures for the p-process simulation of Rayet et al. was $2.2 \leq T_{max} \leq 3.2$ GK, whereas ρ_{max} was 10^6 g cm^{-3}, appropriate for O/Ne layers in type II supernovae. The expansion time scale was set to τ_{ex}=0.446 s, which is equal to the hydrodynamic free expansion time scale $\tau_{HD} \approx 446 \, \rho_{max}$.

2.4.2 Seed nuclei

The initial composition for elements with $Z \leq 20$ was adopted from Woosley et al. [32], taking hydrostatic neon burning yields of ^{16}O, ^{24}Mg, and ^{28}Si with mass fractions of $\approx$0.77, 0.11, and 0.07, respectively. Abundances for elements with $Z \geq 20$ were taken from the He exhaustion in a 60 M$_\odot$ star with 3% metallicity, as calculated by Prantzos et al. [33] with a full s-process network. It should be noted here that these abundances have been obtained with a Maxwellian averaged cross section for ^{22}Ne of $<\sigma>_{30 \, keV}$=0.04 mb [34], whereas the present recommended value for this reaction is 0.058 mb [35], a factor of 1.45 higher.

2.4.3 Nuclear reaction network

The aforementioned seed nuclei are linked by a complex reaction network, including (n,γ), (n,p), (n,α), (p,γ), (p,α), (α,γ), and the respective inverse rates. Additionally, the 3α, ^{12}C(^{12}C,x)y, ^{12}C(^{16}O,x)y, and ^{16}O(^{16}O,x)y reactions are included. Altogether, this network involves $\approx$1050 nuclei which are connected by $\approx$10860 reactions. Since the largest part of such a p-process reaction network is located in the region of proton-rich unstable nuclei, most of the reactions are not yet accessible by experimental techniques and have to be inferred from statistical model calculations.

2.4.4 p-process reaction flow

It has been pointed out by [31] that different mass regions require different temperature windows to produce p nuclei. Light p nuclei (N≤50) are produced at high (peak) temperatures of T_{max} ≥3 GK, whereas intermediate (50≤N≤82) and heavy (N≥82) nuclides are produced at T_{max}=2.5-3 GK and T_{max} ≤2.5 GK, respectively.

Starting from r or s-process seed nuclei the main reaction path flows towards proton-rich nuclei via (γ, n) (see Fig. 2.2). As the neutron separation energy increases, this flow is hindered until it branches out, when (γ,p) and (γ, α) reactions become comparable or faster than neutron emission within an isotopic chain. These "branching points", indicated in Fig. 2.6 as downward arrows, depend strongly on the temperature and are shifted deeper into the proton-rich region with increasing mass number. This photodisintegration mechanism is the favoured way of producing heavy p nuclei.

For lighter nuclei the (γ, n) flow is impeded by (n, γ) reactions, which even dominate for even-even isotopes due to their high neutron separation energies. Rayet et al. [31] investigated this influence of neutron reactions for temperatures T= 2.2 - 3.2 GK by comparing overabundance factors if (n,γ) reactions on Z>26 nuclides were considered or completely suppressed. As a result, the overabundances were found to change by up to a factor 100 (e.g. for ^{84}Sr) if the (n,γ) channel was artificially suppressed. This rather high sensitivity indicates the need for reliable (n,γ) rates to be used in p-process network calculations.

2.4.5 Neutrons in the p process

The role of (n,γ) reactions in the p process was underestimated for a long time, although it is obvious that they have an influence on the final p-process abundances and can play a two-fold role.

On one hand, they can compete with (γ, n) reactions and thus hinder the photodisintegration flux towards lighter nuclei, especially at lower-Z isotopes and even-even isotopes in the vicinity of branching-points (see Fig. 2.6). The influence of a variation of reaction rates on the final p abundances has been studied previously [36, 37, 38]. It turned out that the p abundances are very sensitive to changes of the neutron-induced rates in the entire mass range, whereas the proton-induced and α-induced reaction rates are important at low and high mass numbers, respectively.

Additionally, neutron captures play a secondary role as freeze-out reaction. While the peak temperatures in the p process (T=2-3 GK) correspond to neutron energies of kT=170-260 keV, this temperature drops exponentially right after the explosion (see Fig. 8.2; there the temperature reaches $T \approx$ 1.5 GK after 1 sec).

For these high neutron energies no stellar neutron sources with Maxwellian distributions exist so far. The available neutron sources correspond to kT= 5.1 keV [39] $(^{18}O(p, n)^{18}F$ at E_p= 2582 keV), kT= 25 keV [40] $(^{7}Li(p, n)^{7}Be$ at E_p= 1912 keV) , and kT= 52 keV [41] $(^{3}H(p, n)^{3}He$ at E_p= 1099 keV). Quasi-monoenergetic neutron spectra can be produced for E_n= 150 and 220 keV with the $^{7}Li(p, n)$ reaction at higher proton energies but with lower neutron yields compared to the
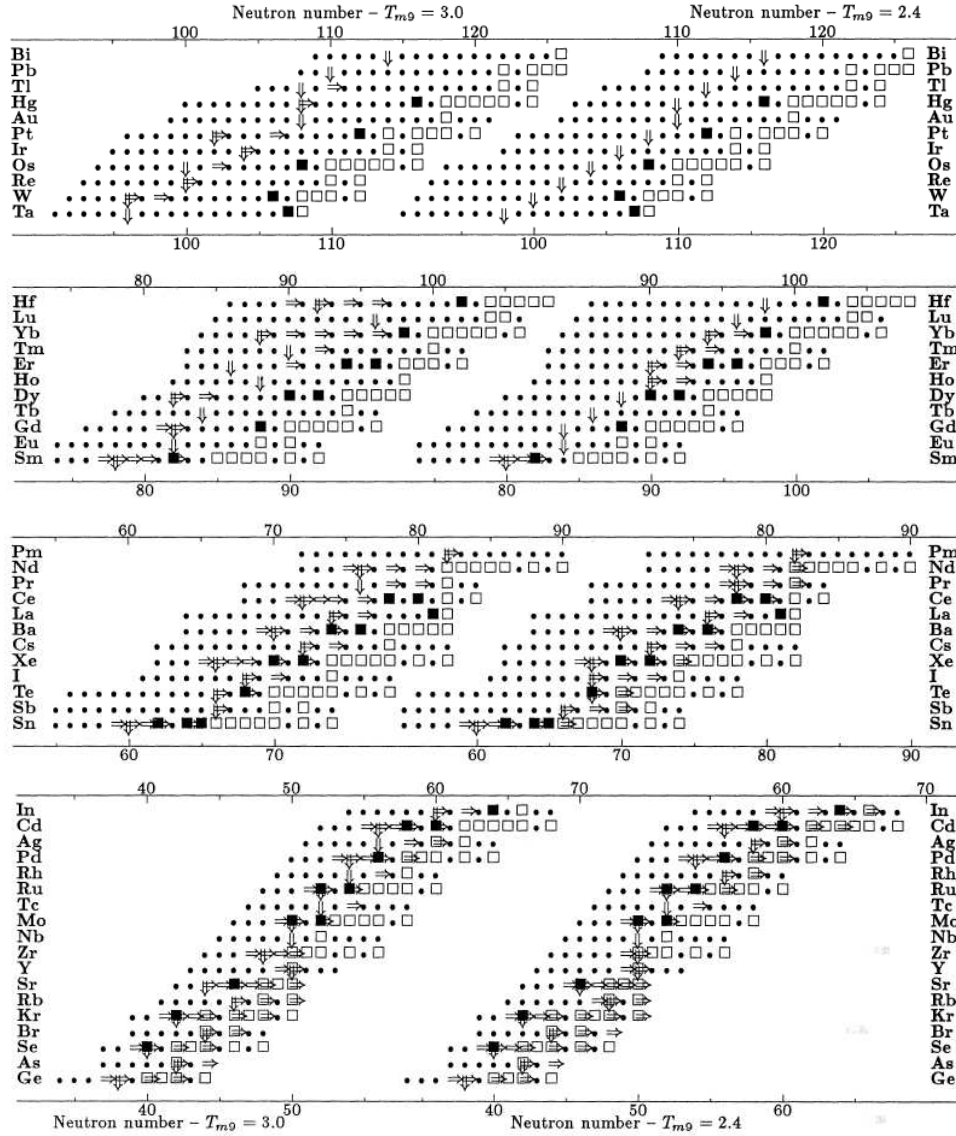
Figure 2.6: Schematic representation of the nuclear flows during the p process $\approx 10^{-5}$ s after the explosion. At this time, the amount of $n, p,$ and α particles reaches the maximum value. The left part of the picture corresponds to a peak temperature of $T_{max} = 3.0$ GK, the right part to $T_{max} = 2.4$ GK. Open boxes indicate r and s nuclei, filled boxes p nuclei and circles radioactive nuclei belonging to the network. Upward arrows indicate branching points, where (γ, p) and (γ, α) start to dominate over (γ, n) reactions. Arrows pointing to the right show isotopes, where the (γ, n) flow is impeded by neutron capture. Picture taken from [31].

quasi-Maxwellian spectrum at $kT=25$ keV. Thus most stellar neutron capture cross sections have to be measured at lower energies, and then extrapolated to higher energies with help of the energy-dependencies deduced from the statistical Hauser-Feshbach model or evaluated data libraries (see Chapter 3).

The neutron capture targets examined in the framework of this thesis (^{74}Se, ^{84}Sr, ^{102}Pd, ^{120}Te, ^{130}Ba, ^{132}Ba, and ^{174}Hf) are all even-even. Neutron capture is thus the complementary reaction to the photodissociation of the (A+1) radioactive isotope, which cannot (yet) be studied in this direction due to lack of proper samples. Although recent efforts are directed to the calculation or measurement of photo-disintegration cross sections and rates, astrophysical photodisintegration rates can easily be inferred from capture rates by detailed balance [22] (see Sec. 2.3.2).

Chapter 3

Experimental technique and data analysis

3.1 Neutron capture measurements

3.1.1 Experimental setup

All neutron capture measurements were carried out at the Karlsruhe 3.7 MV Van de Graaff accelerator using the activation technique. Neutrons were produced with the ^{7}Li$(p,n)^7$Be source by bombarding 30 μm thick layers of metallic Li or crystalline LiF on a water-cooled Cu backing with protons of 1912 keV, 31 keV above the ^{7}Li(p,n) reaction threshold at 1881 keV. The resulting quasi-stellar neutron spectrum approximates a Maxwellian distribution for $kT=$ 25.0 $\pm$ 0.5 keV [42], but is truncated at $E_n=$ 106 keV (see Fig. 3.1). Under these conditions, all neutrons are collimated into a forward cone of 120° opening angle. Neutron scattering through the Cu backing is negligible, since the transmission is $\approx$98% in the energy range of interest. As discussed in [42], a Maxwellian distribution for $kT=$ 30 keV could be approximated by raising the proton energy, thus avoiding the extrapolation from 25 keV to 30 keV with energy-dependent cross sections but then the neutron beam is no longer collimated in forward direction and corrections due to neutron scattering in the target area become necessary.

The use of different neutron target materials was necessary due to the unfavorable behavior of Li in long-time activations ($t_{act} \geq$3 d). Lithium is an air-sensitive metal with a very low (T=180°C) melting point. Thus for target mounting and exchange it was necessary to keep the fresh targets under liquid nitrogen or argon. During the activation, the Li layer was partially evaporated and destroyed by the impinging protons which was clearly visible by the steep decrease of the neutron yields at the beginning. This disadvantage made it necessary to change Li targets during long-time activations every 2-3 days. LiF in contrast has a much higher (T=848°C) melting point and can be handled under "normal" conditions. The decrease in the neutron yield during the activation is less pronounced and can approach a nearly constant flux. Nevertheless, one has to consider that a 30 μm thick layer of LiF
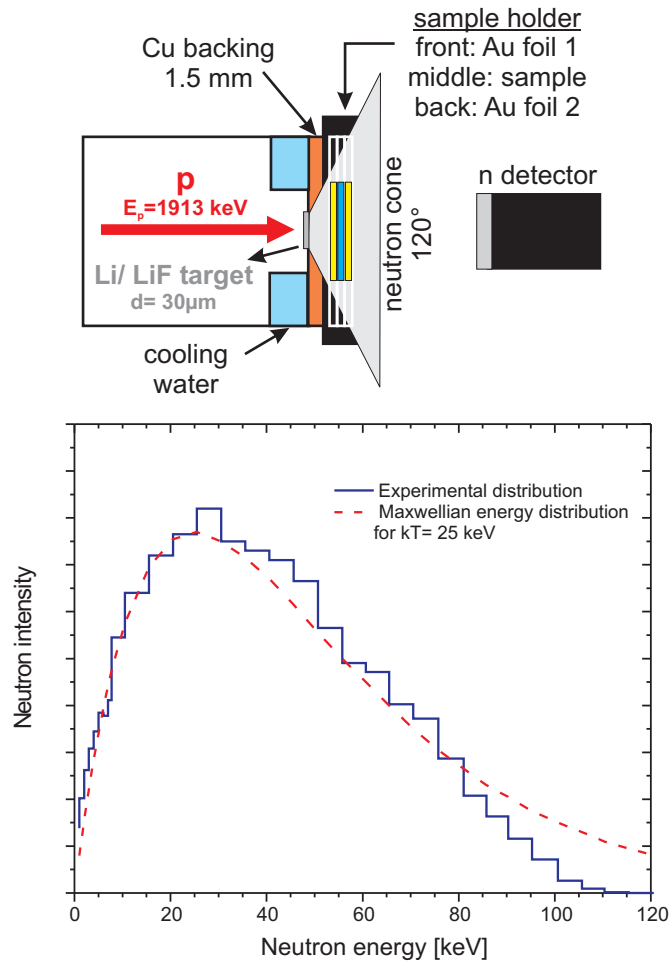
Figure 3.1: Top: Schematic view of the activation setup with the Li/LiF target and the sample-gold sandwich. Bottom: Comparison of the experimental neutron distribution from the $^7Li(p,n)^7Be$ source with a Maxwellian distribution of kT=25 keV.

contains only half the amount of Li atoms compared to a metallic Li layer. Therefore LiF targets are only useful for long-time activations ($t_{act}{\geq}3$ d).

For all activations samples with natural composition were used. The sample material was either metallic or a compound (Table 3.1). In order to verify the stoichiometry and to remove possible water due to the hygroscopic behavior, the samples of $Sr(OH)_2$ and SrF_2 were dried at 300°C and 800°C, respectively.

Thin pellets were pressed from the respective powders or granules and enclosed in 15 μm thick aluminium foil or, in the case of the Pd and Hf samples, cut from thin foils. The samples are then sandwiched between 10-30 μm thick gold foils of the same diameter in close geometry to the neutron target. In this way the neutron flux can be determined relative to the well-known capture cross section of ^{197}Au [42]. The activation measurements were carried out with the Van de Graaff accelerator operated in DC mode with a current of ≈100 μA (for the Li targets) or

even higher currents (up to 150 μA) for the LiF targets. The mean neutron flux over the period of the activations was $\approx$1.5-3$\times 10^9$ s^{-1} at the position of the samples. To ensure homogeneous illumination of the entire surface the proton beam was wobbled across the Li target throughout the irradiation. The activation of the samples was performed in close contact with the Li target at the position of the highest flux (see Fig. 3.1). The neutron flux was recorded during the whole irradiation in intervals of 60 s or 90 s using a ^{6}Li-glass detector for later correction of the number of nuclei which decayed during the activation (factor f_b in Eq. 3.2).

Table 3.1: Isotopic abundances and used sample materials. Isotopic abundances are from Ref. [43], unless noted otherwise. [1] Best value from [44]. [2]Best value from [45].

Element	Isotope	Isotop. abund. [%]	Sample material
Se	^{74}Se	0.89 (4)	Se (metal)
Sr	^{84}Sr	0.56 (1)	$Sr(OH)_2$, SrF_2, $SrCO_3$
Pd	^{102}Pd	1.02 (1)	Pd (metal)
Te	^{121}Te	0.096 (1)[1]	Te (metal)
Ba	^{130}Ba	0.106 (1)	$BaCO_3$
	^{132}Ba	0.101 (1)	$BaCO_3$
Hf	^{174}Hf	0.1620 (9)[2]	Hf (metal)

3.1.2   Detectors

For the measurement of the induced activities after the irradiation two detector setups were available. A single high purity Germanium (HPGe) detector with a well defined geometry of (76.0±0.5 mm from the HPGe detector, distance XX) and 10 cm lead shielding was used in all cases for the counting of the gold foils, as well as for the activities of ^{75}Se, ^{85}Sr, ^{121}Te, ^{131}Ba, ^{133m}Ba, and ^{175}Hf. Energy and efficiency calibrations have been carried out with a set of reference γ-sources in the energy range between 60 keV and 2000 keV (Fig. 3.2).

The activities of ^{103}Pd and ^{133g}Ba were measured with a gamma detection system consisting of two HPGe Clover detectors [46] as shown in Fig. 3.3. Each Clover detector consists of four independent HPGe n-type crystals in a common cryostat. The crystals are 50 mm in diameter and 70 mm in length. The front part of the crystals in one of the Clovers is slightly tapered. Energetic decay electrons were absorbed by thin plastic sheets in front of the detectors. The total crystal volume of the detector system is about 1000 cm^3. The two Clovers are placed face to face in close geometry and form nearly a 4π array by touching the 5.2 mm thick sample holder. This holder is designed to guarantee an exact and reproducible positioning of the sample in the very center of the system. The whole assembly is covered with 10 cm of lead in order to decrease the room background. All crystals of the two Clovers have independent outputs, which are amplified via spectroscopy amplifiers with a shaping time of 6 μs. Each amplifier is connected to a 8192 channel Analog-to-Digital Converter (ADC). The ADC signals are registered by the data acquisition card of a PC and events are analyzed by the MPAWIN software. This tool kit allows to visualize each spectrum of the eight HPGe detectors, which are analyzed independently. The total count rate of each γ line is then derived by summing up all eight single count rates. The efficiency calibration of the Clover was carried out with a set of weak standard calibration sources [46] and verified before the measurement. A typical efficiency curve is given in Fig. 3.3.

For the measurement of the ^{103}Pd and ^{133g}Ba activity with the Clover setup, the correction factors K_γ, K_E and K_S have been calculated by means of Monte Carlo simulations using the GEANT4 software [47, 48]. These factors account for the γ-ray self absorption, the extended geometry of the sample, and the summing effect of the detector due to cascade transitions, respectively. The calculated values are tabulated in Tables 3.8 and 3.13.

For the measurement of all other samples with the single HPGe, only the γ-ray self-absorption k$_\gamma$ has to be considered [40]. For disk shaped samples with a thickness d and γ-ray absorption coefficients μ [49], one obtains $k_\gamma = \frac{1-e^{-\mu d}}{\mu d}$. For the thin (10-30 μm) gold foils, this correction factor was close to 1.

Table 3.2: Decay properties of the product nuclei. Shown here are only the strongest transitions. * Transitions not used in analysis.

Isotope	Final state	$t_{1/2}$	E_γ [keV]	I_γ [%]	Reference
^{75}Se	Ground state	119.79 (4) d	121.1*	17.2 (3)	[50]
			136.0	58.3 (7)	
			264.7	58.9 (3)	
			279.5*	25.0 (1)	
			400.7*	11.5 (1)	
^{85}Sr	Ground state	64.84 (2) d	514.0	95.7 (40)	[51]
	Isom. state (EC)	67.63 (4) min	151.2	12.9 (7)	
	Isom. state (IT)		231.9	84.4 (22)	
^{103}Pd	Ground state	16.991 (19) d	357.5	2.21×10^{-2} (7)	[52]
			497.1*	0.40×10^{-2} (1)	
^{121}Te	Ground state	19.16 (5) d	573.1	80.3 (25)	[53]
	Isom. state (IT)	154 (7) d	212.2	81.4 (1)	
	Isom. state (EC)		1102.1	2.54 (6)	
^{131}Ba	Ground state	11.50 (6) d	123.8	29.0 (3)	[54]
			216.1	19.7 (2)	
			373.2	14.0 (2)	
			496.3	46.8 (2)	
	Isom. state (IT)	14.6 (2) min	108.5*	55.4 (X)	
^{133}Ba	Ground state	10.52 (13) y	81.0*	34.1 (3)	[55]
			302.9*	18.3 (6)	
			356.0	62.1 (2)	
	Isom. state (IT)	38.9 (1) h	275.9	17.8 (6)	[56]
^{175}Hf	Ground state	70 (2) d	343.4	84.0 (30)	[57]
^{198}Au	Ground state	2.69517 (21) d	411.8	95.58 (12)	[58]

Efficiency HPGe
Distance XX, 88-1408 keV

Data: Data1_B
Model: Eff-expdec2
Equation: P1*exp(-x/P2) + P3*exp(-x/P4)
Weighting:
y   w = 1/(data1_d)^2

Chi^2/DoF   = 1.66267
R^2   = 0.99772

P1   0.02351   ±0.0007
P2   125.17612 ±3.27758
P3   0.00211   ±0.0001
P4   905.76856 ±34.71461
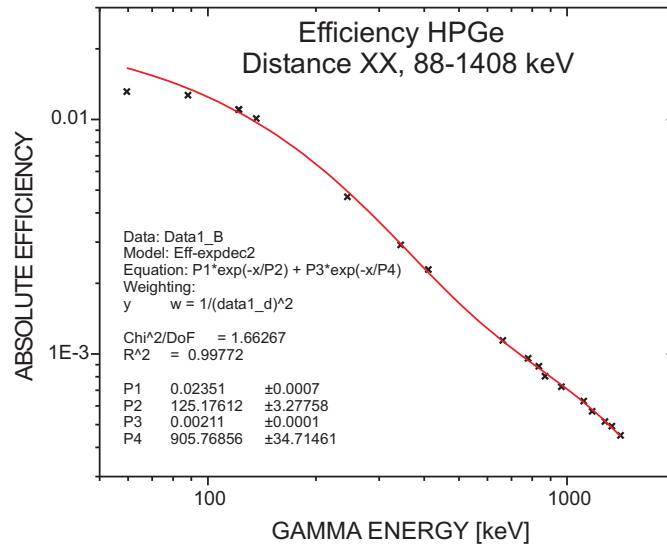
Figure 3.2: Efficiency curve for the single HPGe detector.

Efficiency Clover
(88 keV- 1836 keV)

Equation: P1*exp(-x/P2) + P3*exp(-x/P4)
Weighting: y   w = 1/(exp_c)^2

R^2 = 0.99908

P1   0.16316   ±0.00958
P2   1595.91772 ±111.85256
P3   0.67521   ±0.02732
P4   183.89746 ±9.70299
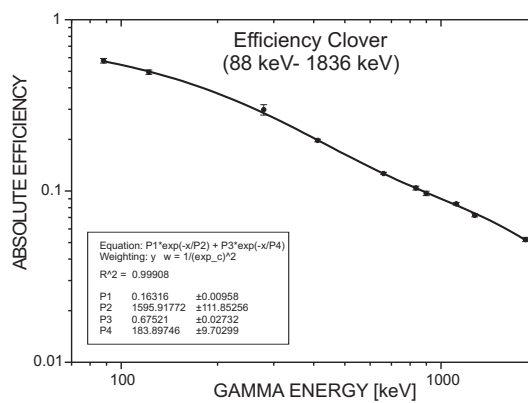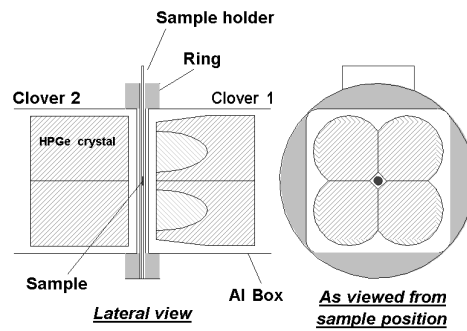
Figure 3.3: Top: Gamma detection system (Clover). Bottom: Efficiency curve for the Clover detectors in close geometry.
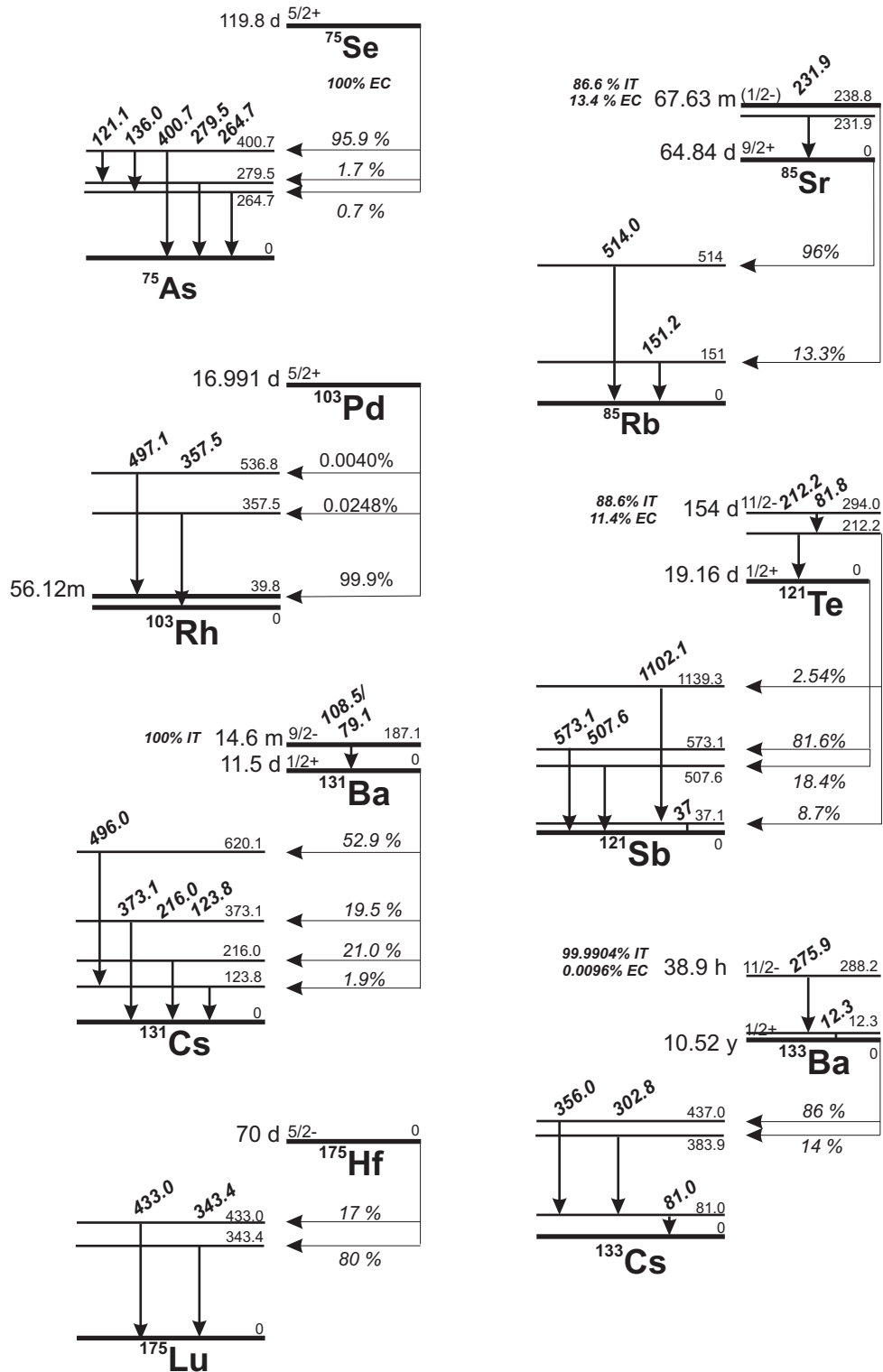
Figure 3.4: Decay schemes of ^{75}Se, ^{85}Sr, ^{103}Pd, ^{121}Te, ^{131}Ba, ^{133}Ba, and ^{175}Hf.

3.2 Data analysis

The total amount of activated nuclei N_{act} at the end of the irradiation can be deduced from the number of events C in a particular γ-ray line registered in the HPGe detector during the measuring time t_m [40]:

$$N_{act} = \frac{C(t_m)}{\varepsilon_\gamma \; I_\gamma \; k \; (1 - e^{-\lambda \; t_m}) \; e^{-\lambda \; t_w}} \qquad (3.1)$$

The factor t_w corresponds to the waiting time between irradiation and activity measurement. The factors ε_γ and I_γ account for the HPGe efficiency and the relative γ intensity per decay of the respective transition. The factor k stands for k_γ or K_{Total}, as described before.

The factor

$$f_b = \frac{\int_0^{t_a} \phi(t) \; e^{-\lambda(t_a - t)} \; dt}{\int_0^{t_a} \phi(t) \; dt} \qquad (3.2)$$

accounts for the decay of the activated nuclei during the irradiation time t_a as well as for variations in the neutron flux. This factor can be calculated from the neutron flux history recorded throughout the irradiation with the ^{6}Li glass detector in 91 cm distance from the target.

The number of activated nuclei N_{act} can also be written as

$$N_{act}(i) = N_i \; \sigma_i \; \Phi_{tot} \; f_b(i), \qquad (3.3)$$

where $\Phi_{tot} = \int \phi(t) dt$ is the time-integrated neutron flux and N_i the number of atoms in the sample. As our measurements are carried out relative to ^{197}Au as a standard, the neutron flux Φ_{tot} cancels out:

$$\frac{N_{act}(i)}{N_{act}(Au)} = \frac{\sigma_i \; N_i \; f_b(i)}{\sigma_{Au} \; N_{Au} \; f_b(Au)}$$
$$\Longleftrightarrow \sigma_i = \frac{N_{act}(i) \; \sigma_{Au} \; N_{Au} \; f_b(Au)}{N_{act}(Au) \; N_i \; f_b(i)}. \qquad (3.4)$$

The reference value for the experimental ^{197}Au cross section in the quasi-stellar spectrum of the ^{7}Li$(p,n)^7$Be source is 586±8 mb [42]. By averaging the induced activities of the gold foils, one can determine the neutron flux Φ_{tot} at the position of the sample and deduce the experimental cross section σ_i of the investigated sample as shown in Eq. 3.4.

3.2.1 Ground-state correction

In the activations of ^{84}Sr, ^{120}Te, ^{130}Ba, and ^{132}Ba, the neutron capture populates both, ground and isomeric states, in the product nucleus. Due to the short half-life of 14.6 min, the partial cross section to ^{131}Ba^m could not be measured in these activations. Thus, only the total capture cross section of ^{130}Ba is derived. The

isomeric state in ^{133}Ba is de-excited with 99.99% probability by isomeric transitions with a half-life of 38.9 h and the ground-state activity with 10.52 yr half-life can be easily measured afterwards to derive the total cross section.

However, in cases where the half-lives of ground and isomeric state are in the same order of magnitude, as for ^{121}Te where the isomeric state (88.6% IT, 11.4% EC) is even longer-lived than the respective ground-state, the analyzing procedure is more complicated. The same holds for ^{85}Sr, where the isomeric state is depopulated by both, electron captures (13.4%) and isomeric transitions (86.6%). To disentangle the contributions from isomeric and ground state to the total cross section the following correction has been applied.

For ^{84}Sr the partial cross section to the isomeric state can be easily calculated in the "normal" way, while the partial cross section to the ground state has to be corrected for those nuclei which decayed during activation and measuring time already by isomeric transitions.

For ^{120}Te the partial cross section to the ground state can be deduced from the γ-spectra of the first few days, where only a negligible contribution from the isomeric state is expected.

The amount of isomer and ground state nuclei after the activation time t_a is described by

$$Z_m(t_a) = N \ \sigma_m \ \Phi_{tot} \ f_m^b \tag{3.5}$$

$$Z_g(t_a) = N \ \Phi_{tot} \ (\sigma_g \ f_g^b \ + \ Y \ \sigma_m \ \lambda_m \ g_m). \tag{3.6}$$

Y is the branching ratio of the isomeric transition (0.866 for ^{85}Sr^m), and the factor g_m is calculated with:

$$g_m = \frac{\int_0^{t_a} e^{-\lambda_g(t_a-t)} \ dt \ \int_0^t \phi(t^*) \ e^{-\lambda_m(t-t^*)} dt^*}{\int_0^{t_a} \phi(t) \ dt}. \tag{3.7}$$

The relation between the activity of the ground state and the measured count rate C_g can be calculated by

$$C_g(t_w + t_m) \ = \ k_\gamma \ \varepsilon_\gamma \ I_\gamma \int_{t_w}^{t_w+t_m} A_g(t) \ dt. \tag{3.8}$$

$A_g(t)$ is further described as

$$A_g(t) \qquad = A_g(t_a) \ e^{-\lambda_g t} \ +$$
$$+ \ Y \ \frac{\lambda_g}{\lambda_g-\lambda_m} \ A_m(t_a) \ (e^{-\lambda_m t} - e^{-\lambda_g t}). \tag{3.9}$$

Inserting $A_i = Z_i \ \lambda_i$, solving the integral and converting to $Z_g(t_a)$ leads to

$$Z_g(t_a) = \frac{C(t_w + t_m)}{k_\gamma \ \varepsilon_\gamma \ I_\gamma \ (e^{-\lambda_g t_w} - e^{-\lambda_g(t_w+t_m)})} \ - \tag{3.10}$$

$$- \ \frac{Y \ \frac{\lambda_g}{\lambda_g-\lambda_m} \ Z_m(t_a) \ (e^{-\lambda_m t_w} - e^{-\lambda_m(t_w+t_m)})}{e^{-\lambda_g t_w} - e^{-\lambda_g(t_w+t_m)}} \ + \tag{3.11}$$

$$+ \ \frac{Y \ \frac{\lambda_m}{\lambda_g-\lambda_m} \ Z_m(t_a) \ (e^{-\lambda_g t_w} - e^{-\lambda_g(t_w+t_m)})}{e^{-\lambda_g t_w} \ - \ e^{-\lambda_g(t_w+t_m)}}. \tag{3.12}$$

Thus, σ_g can finally be deduced from Eq. 3.6 by inserting $Z_g(t_a)$:

$$\sigma_g = \frac{Z_g(t_a)}{N \; \Phi_{tot} \; f_g^b} \; - \; \frac{Y \; \sigma_m \; \lambda_m \; g_m}{f_g^b}. \tag{3.13}$$

The second term in Eq. 3.13 describes the isomeric transition, for which the ground-state cross section has to be corrected. For half-lives shorter than the ground-state, this part introduces major corrections, whereas for longer half-lives this term becomes small.

3.2.2 ^{74}Se(n,γ)^{75}Se

For the determination of the ^{74}Se neutron capture cross section five activations were performed (see Table 3.3).

Table 3.3: Activation schemes and sample characteristics for the Se measurements. Φ_{tot} gives the total neutron exposure of the sample during the activation.

Material	Sample No.	Diameter [mm]	Mass [mg]	Atoms ^{74}Se	t_a [min]	Φ_{tot} [neutrons]
Se	se-1	6	151.8	1.03×10^{19}	931	1.10×10^{14}
	se-2	10	200.2	1.36×10^{19}	419	1.53×10^{13}
	se-3	6	102.2	6.94×10^{18}	1400	1.64×10^{14}
	se-4	10	207.8	1.41×10^{19}	1420	0.99×10^{14}
	se-5	10	147.8	1.00×10^{19}	1425	1.16×10^{14}

The ^{74}Se(n,γ)^{75}Se reaction was analyzed via the two strongest transitions in ^{75}As at 136.0 keV and 264.7 keV. The results from the individual Se activations are listed in Table 3.4. The capture cross section derived with the experimental neutron distribution is 281±16 mbarn and was calculated as the weighted mean value of all five activations.

Table 3.4: Results from the Se activations. *Value not included in mean value.

Activation ^{74}Se(n,γ)^{75}Se	Cross section [mbarn] (136 keV)	(265 keV)
se-1	283 ± 16	276 ± 16
se-2	270 ± 15	$259 \pm 14^*$
se-3	273 ± 16	265 ± 15
se-4	291 ± 16	287 ± 16
se-5	300 ± 17	284 ± 16
weighted average	281 ± 16	

3.2.3 ^{84}Sr(n,γ)^{85}Sr

For the cross sections to the ground and isomeric state of ^{85}Sr in total 12 activations were performed. Five short-time activations of 155 min to 274 min were used for determining the partial cross section of the ^{84}Sr$(n,\gamma)^{85}$Sr^m reaction feeding the isomer in ^{85}Sr with a half-life of 67.63 min. The ^{84}Sr$(n,\gamma)^{85}$Sr^g cross section to the ground state (t$_{1/2}$= 64.64 d) was separately deduced from seven long-time activations (see Table 3.5).

Table 3.5: Activation schemes and sample characteristics. The suffix "m" denotes short time activations for measurements of the partial cross section to the ^{85}Sr^m isomeric state. Φ_{tot} gives the total neutron exposure of the sample during the activation.

Material	Sample No.	Diameter [mm]	Mass [mg]	Atoms ^{84}Sr	t_a [min]	Φ_{tot} [neutrons]
Sr(OH)$_2$	sr-1	6	67.6	1.88×10^{18}	1386	1.45×10^{14}
	sr-2	10	161.2	4.47×10^{18}	1470	8.03×10^{13}
	sr-3	6	119.8	3.32×10^{18}	1234	1.59×10^{14}
	sr-4m	6	147.5	4.09×10^{18}	155	1.13×10^{13}
	sr-5m	10	195.3	5.42×10^{18}	199	2.27×10^{13}
SrF$_2$	sr-6	10	478.3	1.28×10^{19}	1461	1.16×10^{14}
	sr-7	10	195.7	5.25×10^{18}	2621	1.31×10^{14}
	sr-8m	8	204.5	5.49×10^{18}	207	3.29×10^{13}
	sr-9m	10	314.4	8.44×10^{18}	274	2.77×10^{13}
SrCO$_3$	sr-10	8	91.2	2.08×10^{18}	1277	1.64×10^{14}
	sr-11	10	152.1	3.47×10^{18}	1257	9.30×10^{13}
	sr-12m	8	222.6	5.09×10^{18}	194	1.91×10^{13}

In case of ^{84}Sr, neutron captures populate both, ground and isomeric state of ^{85}Sr. While ^{85}Sr^g decays can be identified via the 514 keV transition in ^{85}Rb, the decay of the isomer proceeds mainly via transitions of 232 keV and 151 keV. The isomeric state is 239 keV above the ground state and decays either via a 7 keV- 232 keV cascade (internal transition, 86.6%) or directly by electron capture (13.4%) into the 151 keV level of the daughter nucleus ^{85}Rb.

The partial cross section to the isomeric state can be easily deduced from the above mentioned transitions at 151 keV and 232 keV and yields 189±10 mbarn (see Table 3.6). The cross section to the ground state has to be corrected for the internal decay of the isomer during the activation and measuring time and results in 112±8 mbarn. This leads to a total capture cross section of 301±18 mbarn.

Table 3.6: Results from the Sr activations.

Activation ^{84}Sr(n,γ)	cross section [mbarn]		
	$\rightarrow^{85}$Sr^g	$\rightarrow^{85}$Sr^m	
	(514 keV)	(151 keV)	(232 keV)
sr-1	114 ± 9		
sr-2	124 ± 8		
sr-3	102 ± 8		
sr-4m		189 ± 13	194 ± 10
sr-5m		194 ± 13	194 ± 8
sr-6	106 ± 7	178 ± 12	189 ± 8
sr-7	107 ± 7		
sr-8m		186 ± 12	190 ± 9
sr-9m		187 ± 12	191 ± 8
sr-10	122 ± 8	192 ± 13	192 ± 9
sr-11	106 ± 7		
sr-12m		178 ± 12	189 ± 9
weighted average	112 ± 8	189 ± 10	

3.2.4 ^{102}Pd(n,γ)^{103}Pd

For the determination of the ^{102}Pd neutron cross section three long-time activations were performed (see Table 3.7). The samples were cut from 25μm thick Pd foil of 99.5 % purity.

Due to the weak γ transitions the activated samples were counted with the Clover detector setup [46]. For this reason the γ-ray absorption coefficients were calculated with GEANT [47, 48], see Table 3.8. The Pd samples were analyzed via the "strongest" transition in ^{103}Rh at 357 keV. The second strongest transition at 497 keV was already too weak for analysis. The result for the experimental neutron capture cross section is 378 ± 14 mbarn.

Table 3.7: Activation schemes and sample characteristics for the Pd measurements. Φ_{tot} gives the total neutron exposure of the sample during the activation.

Material	Sample No.	Diameter [mm]	Mass [mg]	Atoms ^{102}Pd	t_a [min]	Φ_{tot} [neutrons]
Pd	pd-1	10	452.5	2.61×10^{19}	9770	8.18×10^{14}
	pd-2	8	301.5	1.74×10^{19}	5751	4.83×10^{14}
	pd-3	12	339.5	1.96×10^{19}	7585	3.48×10^{14}

Table 3.8: GEANT simulations of the correction factors for ^{103}Pd

Sample	Thickness [mm]	K_E	K_γ	K_S	K_{Total}
pd-1	0.5	0.9976	0.9563	0.9991	0.9531
pd-2	0.5	0.9986	0.9569	0.9951	0.9509
pd-3	0.25	0.9972	0.9762	0.9663	0.9407

Table 3.9: Results from the Pd activations.

Activation ^{102}Pd(n,γ)	Cross section [mbarn] (357 keV)
pd-1	374 ± 14
pd-2	357 ± 13
pd-3	403 ± 15
weighted average	378 ± 14

3.2.5 ^{120}Te(n,γ)^{121}Te

For the determination of the ^{120}Te neutron capture cross section five activations were performed (see Table 3.10). From these, also the partial cross section to the 154 d isomeric state was deduced.

Table 3.10: Activation schemes and sample characteristics for the Te measurements. Φ_{tot} gives the total neutron exposure of the sample during the activation.

Material	Sample No.	Diameter [mm]	Mass [mg]	Atoms ^{120}Te	t_a [min]	Φ_{tot} [neutrons]
Te	te-1	10	352.9	1.60×10^{18}	2617	1.96×10^{14}
	te-2	10	441.2	2.00×10^{18}	1600	1.52×10^{14}
	te-3	8	349.3	1.58×10^{18}	1406	1.56×10^{14}
	te-4	8	417.2	1.89×10^{18}	4142	3.03×10^{14}
	te-5	8	409.6	1.86×10^{18}	2593	3.09×10^{14}

The Te samples were analyzed via the 576 keV γ-line from the β^+ decay of ^{121}Te^g into ^{121}Sb. The partial cross section to the isomeric state cannot be measured directly after the irradiation due to a huge Compton background around 210 keV, but after a waiting time of 80 d the expected 212 keV from the IT to the ground state (88.6 %) could be determined.

The result for the neutron capture cross section to the ground-state is 433.8 ± 21.0 mbarn, and 63.2 ± 2.7 mbarn for the partial cross section to the isomeric state. This

leads to a total (n,γ) cross section of $\sigma=497 \pm 23.7$ mbarn.

Table 3.11: Results from the Te activations.

Activation ^{120}Te(n,γ)	cross section [mbarn]	
	$\rightarrow ^{121}$Te^g (576 keV)	$\rightarrow ^{121}$Te^m (212 keV)
te-1	436.8 ± 21.1	62.3 ± 2.6
te-2	429.0 ± 20.8	65.5 ± 2.8
te-3	446.3 ± 21.5	62.2 ± 2.6
te-4	426.2 ± 20.7	61.5 ± 2.7
te-5	431.7 ± 21.0	64.9 ± 2.9
weighted average	433.8 ± 21.0	63.2 ± 2.7

3.2.6 ^{130}Ba(n,γ)^{131}Ba and ^{132}Ba(n,γ)^{133}Ba

The neutron cross sections of ^{130}Ba and ^{132}Ba were deduced from three long-time activations (see Table 3.12). In the case of ^{130}Ba, only the total cross section could be determined, since the isomeric state was too short-lived (14.6 min). For ^{132}Ba the partial cross section to the isomeric state (38.9 h) and the total cross section via the long-lived ground-state (10.52 yr) in ^{133}Ba could be measured. The latter measurement was performed with the Clover setup and thus required a GEANT simulation for the γ-ray absorption coefficients [47], see Table 3.13.

Table 3.12: Activation schemes and sample characteristics for the Ba measurements. Φ_{tot} gives the total neutron exposure of the sample during the activation.

Material	Sample No.	Diameter [mm]	Mass [mg]	Atoms		t_a [min]	Φ_{tot} [neutrons]
				^{130}Ba	^{132}Ba		
BaCO$_3$	ba-1	8	106.9	3.46×10^{17}	3.30×10^{17}	7721	6.93×10^{14}
	ba-2	8	145.5	4.71×10^{17}	4.48×10^{17}	4014	2.70×10^{14}
	ba-3	10	149.7	4.84×10^{17}	4.61×10^{17}	4280	4.48×10^{14}

The ^{130}Ba total neutron capture cross section can be measured via the transitions at 124 keV, 216 keV, 373 keV, and 496 keV from the β^+ decay into ^{131}Cs. Due to its short half-life of 14.6 min no isomeric cross section was determined in this case. The resulting total experimental cross section is 746 ± 29 mbarn.

The partial cross section to the 38.9 h isomer in ^{133}Ba was measured via the 276 keV line (IT) to be 34.2 ± 2.0 mbarn. The total capture cross section was determined with the Clover detector via the strongest EC decay transition into ^{133}Cs at 356.0 keV, and results 393.9 ± 15.4 mbarn.

Table 3.13: GEANT simulations for ^{133}Ba

Sample	Thickness [mm]	K_E	K_γ	K_S	K_{Total}
ba-1	0.48	1.0002	0.9820	0.9575	0.9405
ba-2	0.65	1.0022	0.9752	0.9608	0.9390
ba-3	0.43	0.9994	0.9841	0.9570	0.9412

Table 3.14: Results from the ^{130}Ba activations.

Activation	cross section [mbarn]			
^{130}Ba(n,γ)	(124 keV)	(216 keV)	(373 keV)	(496 keV)
ba-1	757 ± 29	727 ± 29	724 ± 29	750 ± 28
ba-2	793 ± 30	751 ± 30	739 ± 30	769 ± 28
ba-3	742 ± 26	721 ± 23	730 ± 32	745 ± 31
weighted average	746 ± 29			

Table 3.15: Results from the ^{132}Ba activations.

Activation	cross section [mbarn]	
^{132}Ba(n,γ)	$\rightarrow^{133}$Ba^{g+m}	$\rightarrow^{133}$Ba^m
	(356 keV)	(276 keV)
ba-1	396.0 ± 15.2	31.5 ± 1.8
ba-2	403.9 ± 15.6	38.1 ± 2.2
ba-3	381.8 ± 15.5	34.1 ± 2.0
weighted average	393.9 ± 15.4	34.2 ± 2.0

3.2.7 ^{174}Hf(n,γ)^{175}Hf

The line at 343.4 keV was chosen because it has the highest intensity in the decay of ^{175}Hf. However, this line overlapped with a significantly stronger line at 345.9 keV, which originates from the decay of ^{181}Hf. In order to separate these lines, a fit of two Gaussian functions and a constant has been performed with ORIGIN (see Fig. 3.5). The experimental cross section yielded $\sigma_{exp}= 990 \pm 51$ mbarn.

Table 3.16: Activation schemes and sample characteristics for the Hf measurements. Φ_{tot} gives the total neutron exposure of the sample during the activation.

Material	Sample No.	Diameter [mm]	Mass [mg]	Atoms ^{174}Hf	t_a [min]	Φ_{tot} [neutrons]
Hf	hf-1	6	92.0	4.97×10^{17}	5440	8.69×10^{14}
	hf-2	6	92.1	4.97×10^{17}	3865	6.04×10^{14}
	hf-3	8	163.5	8.83×10^{17}	5451	5.09×10^{14}
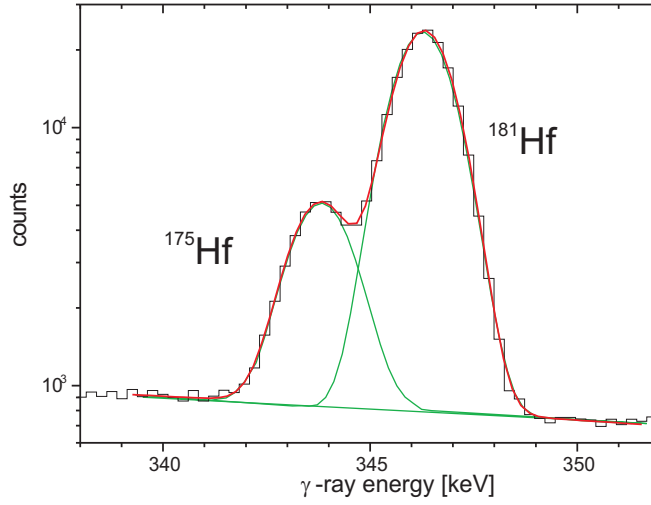
Figure 3.5: Peak-separation of the 343 keV line with two Gaussian fits using ORIGIN.

Table 3.17: Results from the ^{174}Hf activation.

Activation ^{174}Hf(n,γ)	cross section [mbarn] (343 keV)
hf-1	985 ± 51
hf-2	980 ± 51
hf-3	1005 ± 52
Weighted average	990 ± 51

3.3 Isomeric ratios

From the partial cross sections to the isomeric states in ^{85}Sr, ^{121}Te, and ^{133}Ba the isomeric ratio at stellar temperatures ($kT = 25$ keV) was calculated. Table 3.18 gives a comparison of our deduced stellar isomeric ratio at $kT = 25$ keV to the isomeric

ratio at thermal energies of $kT= 25$ meV [59, 60]. For ^{84}Sr there was a significant change in the partial thermal cross section to the ground state between [59] from 1981 and the latest version from 2006 [60]. This caused an increase of the isomeric ratio at thermal energies from 0.632 to 0.756. Thus the latest value is in disagreement with our stellar isomeric ratio. For the other isotopes ^{120}Te and ^{132}Ba we achieve a quite good agreement within the error bars.

Table 3.18: Comparison of isomeric ratios at thermal and at stellar neutron energies. Listed are also the partial thermal cross sections from Ref. [59, 60]. *Cross section measured in a Maxwellian neutron flux. ^{r}Cross section measured with reactor neutrons.

Isotope	thermal cross section →g.s. [mb]	→i.s. [mb]	Isomeric ratio @ 25 meV	Isomeric ratio @ 25 keV	Reference
^{84}Sr	350±70*	600±60*	0.632±0.063	0.633± 0.033	[59]
	199±10*	623±60*	0.756±0.073	0.633± 0.033	[60]
^{120}Te	2000±300^r	340±60^r	0.145±0.026	0.127± 0.005	[59, 60]
^{132}Ba	6500±800^r	500^r	0.071	0.086± 0.005	[59, 60]

3.4 Uncertainties of the (n, γ) cross sections

The experimental uncertainties of the neutron capture measurements are summarized in the following Tables 3.19, 3.20, and 3.21. Since nearly every stellar neutron cross section measurement was carried out relative to gold, the error of 1.4% [42] in the gold cross section cancels out. An uncertainty of 2% was assumed in all measurements due to an estimated sample position uncertainty of 0.25 mm relative to the Au foils during the activation which affects the neutron flux seen by the sample. The same error was used for the uncertainty of the efficiency calibration of both detectors.

For the Se samples, a fairly large contribution results from the 4.5% error of the isotopic abundance [43]. In most cases the largest error is introduced from the uncertainties of the γ-ray intensities.

The errors in the time factors f_b, $f_w = e^{-\lambda\ t_w}$, and $f_m = e^{-\lambda\ t_m}$ are negligible in all measurements except those with a short half-life (^{85}Sr^m) or a large error in the half life (^{175}Hf: 2.9%). The error in the masses (± 0.1 mg) could be neglected for all samples except for the gold foils.

The conservatively assumed overall uncertainty for all measurements ranges between 4 and 8%, which includes the 2.5% uncertainty from the measurement of the gold foils. These uncertainties were also adopted for the Maxwellian averaged cross sections, assuming that the uncertainties of the theoretical energy dependence were negligible for the extrapolation to $kT= 30$ keV.

Table 3.19: Compilation of uncertainties for ^{197}Au, ^{74}Se, ^{84}Sr, and ^{102}Pd. [1]Not included in the final uncertainty, see text. [2]Negligible. [3]Including uncertainty from gold.

	Uncertainty (%)				
	^{197}Au	^{74}Se	^{84}Sr→g	^{84}Sr→m	^{102}Pd
Source of uncertainty	412 keV	136/ 265 keV	514 keV	151/ 232 keV	357 keV
Gold cross section	1.4[1]	–	–	–	–
Isotopic abundance	–	4.5	1.8	1.8	1.0
Detector efficiency	2	2		2	2
Divergence of n flux	2	2		2	2
Sample mass	0.2	–[2]		–[2]	–[2]
γ-Ray intensity	0.1	0.5/ 1.2	4.2	5.4/ 2.6	0.031
γ-Ray self-absorption	–	0.2	0.2	0.2	0.2
Counting statistics	0.1 - 1.0	0.4 - 1.6	3.6 - 5.3	0.4 - 2.0	0.3 - 0.6
Time factors f_b, f_m, f_w	–	–	–	0.2 - 1.3	–
Total uncertainty[3]	2.5	5.5 - 5.7	6.5 - 7.9	4.3 - 7.1	3.7

Table 3.20: Compilation of uncertainties for ^{120}Te and ^{130}Ba. [1]Negligible. [2]Including uncertainty from Au, see Table 3.19.

	Uncertainty (%)		
	^{120}Te→g	^{120}Te→m	^{130}Ba
Source of uncertainty	212 keV	576 keV	124/ 216/ 373/ 496 keV
Isotopic abundance	1.0		0.9
Detector efficiency	2.0		2.0
Divergence of n flux	2.0		2.0
Sample mass	–[1]		–[1]
γ-Ray intensity	0.1	3.1	1.0/ 1.5/ 1.4/ 0.4
γ-Ray self-absorption	0.2		0.2
Counting statistics	2.0 - 2.6	0.4 - 0.8	0.2 - 1.4
Time factors f_b, f_m, f_w	–[1]		–[1]
Total uncertainty[2]	4.2 - 4.5	4.8 - 4.9	3.7 - 4.4

Table 3.21: Compilation of uncertainties for ^{132}Ba and ^{174}Hf. [1]Negligible. [2]Including uncertainty from Au, see Table 3.19.

	Uncertainty (%)		
Source of uncertainty	^{132}Ba→m 276 keV	^{132}Ba→g+m 356 keV	^{174}Hf 343 keV
Isotopic abundance		1.0	0.56
Detector efficiency		2.0	2.0
Divergence of n flux		2.0	2.0
Sample mass		$-$ [1]	$-$ [1]
γ-Ray intensity	3.4	0.3	3.6
γ-Ray self-absorption		0.2	0.3
Counting statistics	2.6 - 3.1	1.2 - 1.4	1.1
Time factors f_b, f_m, f_w		$-$ [1]	0.14
Total uncertainty[2]	5.8 - 6.0	3.8 - 4.0	5.2

3.5 Proton-capture measurements

The proton-induced reactions on natural Palladium samples were carried out with the cyclotron and Van de Graaff accelerator at the Physikalisch-Technische Bundesanstalt (PTB) in Braunschweig/ Germany. During these activations we were able to determine the total capture cross sections of ^{102}Pd and compared it with a previous measurement from Özkan et al. [61]. For all other measurements no previous experimental data was available in the energy range of the p process. The respective Gamow window ($E_0 \pm \Delta/2$) for T=2-3 GK is E_p(c.m.)= 1.72-4.31 MeV, thus our measurements were carried out between 2.75 and 5 MeV. We determined the total cross section of ^{104}Pd(p,γ) but with contributions from the ^{105}Pd(p,n) channel, which already opens at 2.1 MeV. The same holds for ^{105}Pd(p,γ) but here the ^{106}Pd(p,n) channel opens at 3.7 MeV and we could only measure the cross section to the long-lived isomeric state in ^{106}Ag. For ^{110}Pd we could see only the (p,n) channel to the 249.9 d isomeric state in ^{110}Ag, since the respective (p,γ) cross section to ^{111}Ag^g ($t_{1/2}$= 7.45 d) was – according to NON-SMOKER predictions – more than two orders of magnitude weaker. The decay properties and decay schemes of the activated silver isotopes are shown in Table 3.22 and Fig. 3.6.

3.5.1 Sample preparation

The Pd samples were prepared by sputtering thin ($\approx$500 nm) layers of natural Pd on 1 mm thick Al disks 35 mm in diameter at the Institut für Materialforschung (IMF) of Forschungszentrum Karlsruhe. A first estimation of the Pd layer thickness of 380 - 396 nm was deduced from a sensor, which compared the layer on a sputtered Si sample with a blank Si sample.

The real thickness of the various Pd samples was determined by X-Ray Fluorescence (XRF) at Institut für Nukleare Entsorgung (INE) of Forschungszentrum Karlsruhe. Therefore, six Pd standards (50 - 500 μg) were prepared from a standard solution with 1000 μg Pd per ml, plus an additional blank sample for the determination of a calibration curve (Fig. 3.7). Since the Pd solution was only available as acid, we could not use Al backings (which would have been dissolved due to the instability of Al against acid solutions) and took Ta backings instead.

The XRF detector at the INE irradiates the samples with a Bremsstrahlung spectrum of a rhodium anode, and detects the induced characteristic X-ray fluorescence after reflection on a LiF crystal. The thickness deduced from the XRF measurement (Table 3.24) was systematically 20% higher than the results estimated after the sputtering process.

3.5.2 Experimental setup at the PTB

The activation beamline in Braunschweig is shown in Fig. 3.8. The wobbled proton beam from the cyclotron or Van de Graaff accelerator is limited by an aperture 9.5 mm in diameter. In front of this aperture is a second aperture, on which a

Table 3.22: Decay properties of the product nuclei from the proton capture experiments. Shown here are only the strongest transitions. * Transitions not used in analysis.

Isotope	Final state	$t_{1/2}$	E_γ [keV]	I_γ [%]	Reference
^{103}Ag	Ground state	65.7 (7) m	118.7	31.2 (7)	[52]
			148.2	28.3 (5)	
			243.9	8.5 (5)	
			266.9	13.4 (4)	
			531.9*	8.8 (2)	
			1273.8	9.4 (3)	
	Isom. state (IT)	5.7 (2) s	134.4*	4.5 (1)	
^{105}Ag	Ground state	41.29 (7) d	64.0	10.5 (10)	[62]
			280.4	30.2 (17)	
			344.5	41.4 (6)	
			443.4	10.5 (5)	
			644.6*	11.1 (6)	
			1087.9*	3.85 (17)	
	Isom. state (IT)	7.23 (16) m	25.5*	0.00416	
	Isom. state (EC)		319.2*	0.16 (4)	
^{106}Ag	Ground state	23.96 (1) m	511.9*	17.0 (15)	[63]
			616.2*	0.142 (13)	
			621.9*	0.32 (3)	
			1050.4*	0.167 (15)	
	Isom. state (EC)	8.28 (2) d	406.2*	13.4 (4)	
			451.0	28.2 (7)	
			511.9*	88 (3)	
			616.2*	21.6 (6)	
			717.2	28.9 (8)	
			748.4	20.6 (6)	
			1045.8	29.6 (10)	
			1527.7	16.3 (13)	
^{110}Ag	Ground state (β^-)	24.6 (2) s	657.5*	4.50 (23)	[64]
	Ground state (EC)		374*	≤0.02	
	Isom. state (IT)	249.76 (4) d	117.6*	0.0080 (5)	
	Isom. state (β^-)		657.8	94.3 (3)	
			677.6*	10.56 (4)	
			706.7*	16.33 (7)	
			763.9	22.62 (21)	
			884.7	72.7 (4)	
			937.5	34.2 (6)	
			1384.6*	24.9 (8)	
			1505.9*	13.60 (18)	
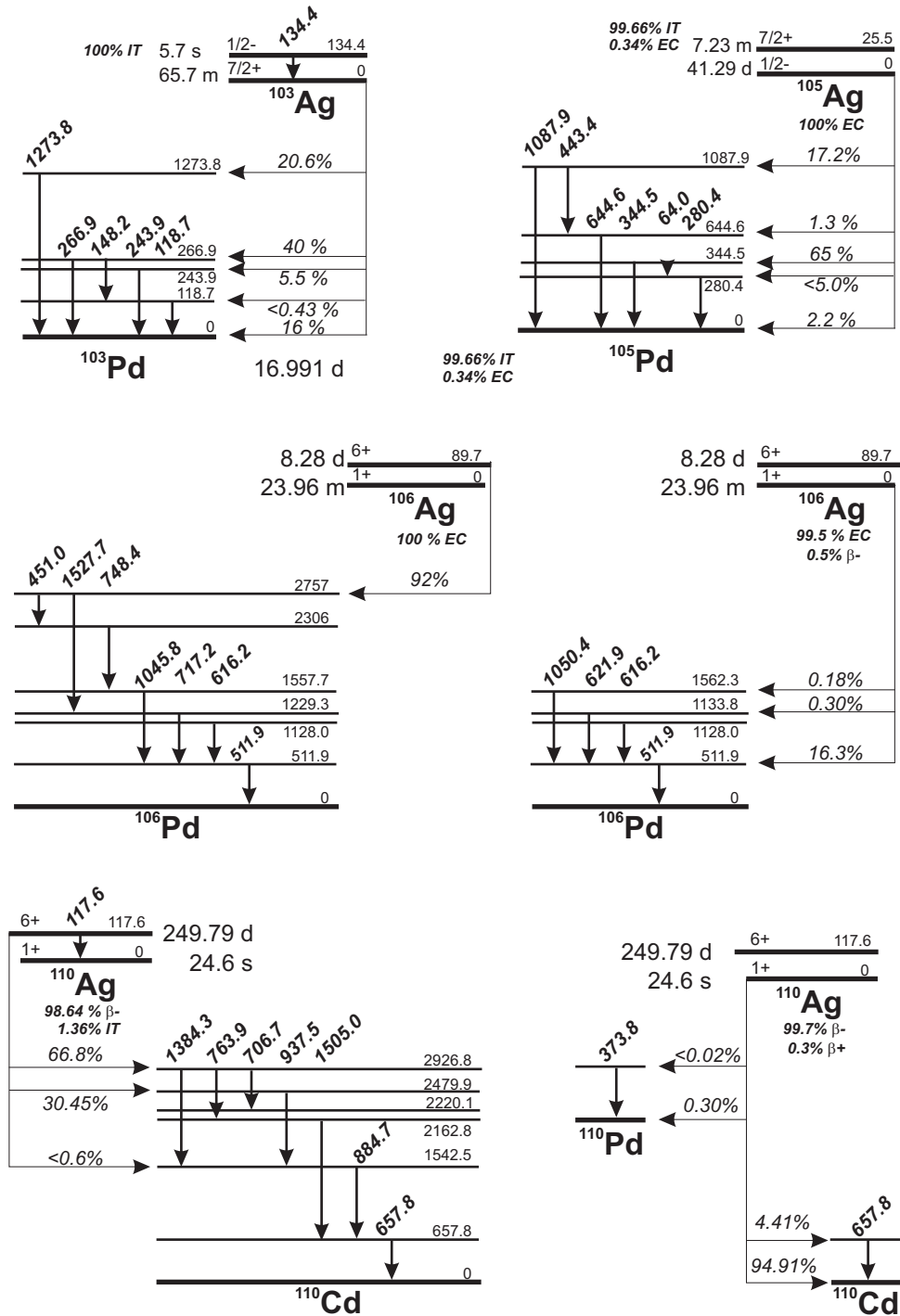
Figure 3.6: Decay schemes of ^{103}Ag, ^{105}Ag, ^{106}Ag, and ^{110}Ag.

Table 3.23: Natural abundances of the Pd isotopes [43].

Isotope	^{102}Pd	^{104}Pd	^{105}Pd	^{106}Pd	^{108}Pd	^{110}Pd
Nat. Abund. [%]	1.02 (1)	11.14 (8)	22.33 (8)	27.33 (3)	26.46 (9)	11.72 (9)

suppression voltage of $U_S=$ -300 V was applied. The opening of the beamline is 13 mm in diameter. The samples with 10 mm Pd in diameter were attached there and cooled from behind (Fig. 3.8). Before each measurement the illumination of the target surface and wobbling of the proton beam was checked with a quartz window. Some of the samples irradiated with the proton beam from the Van de Graaff showed the formation of blisters because the integrated proton flux was higher and the beam much more focussed compared to the irradiation with the cyclotron. The samples were activated at nine different proton energies between 2.75 MeV and 5.00 MeV (see Table 3.25) switching between short-time activations (up to 7200 s for the 65.7 min ground-state in ^{103}Ag) and long-time activations (up to 36000 s at 2.75 MeV).

The produced activity was measured offline with two different HPGe detectors (efficiency curves in Fig. 3.9), which were shielded from room background by 10 cm lead. The PTB detector was used at two distances, P1 (15 mm) and P3 (135 mm), for determining the effect of coincidence summing corrections (see Sec. 3.5.4).

3.5.3   Data analysis

The analysis of the proton-capture measurements is similar to the analysis of neutron-capture measurements. The difference is that we do not measure relative to a standard but directly measure the absolute proton charge which hits the sample (see
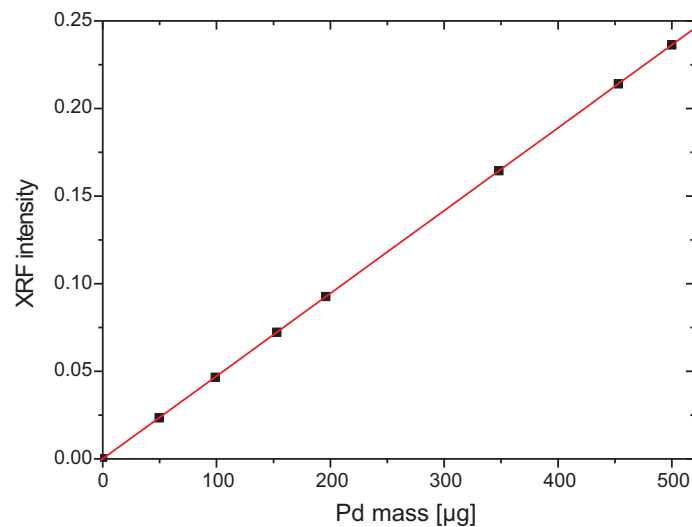
Figure 3.7: XRF-calibration curve.

Table 3.24: Pd masses in [μg] derived from the XRF measurement, area density N in [atoms/cm^2], and the respective thickness in [nm] for the samples used for the proton-capture measurements on Pd.

Sample No.	Mass [μg]	N [atoms/cm^2]	thickness [nm]
1	473.8	3.414×10^{18}	502.7
3	480.3	3.460×10^{18}	509.6
4	458.7	3.305×10^{18}	486.7
5	492.5	3.549×10^{18}	522.6
6	442.7	3.190×10^{18}	469.7
7	466.2	3.359×10^{18}	494.6
8	460.8	3.320×10^{18}	489.0
9	457.7	3.298×10^{18}	485.6
10	435.5	3.138×10^{18}	462.1
11	425.3	3.064×10^{18}	451.2
12	437.5	3.152×10^{18}	464.3
13	413.5	2.979×10^{18}	438.7
38	442.7	3.190×10^{18}	469.7
39	451.6	3.254×10^{18}	479.2
40	429.6	3.096×10^{18}	455.9
41	434.9	3.134×10^{18}	461.5
42	432.5	3.116×10^{18}	458.9
43	422.2	3.042×10^{18}	448.0
44	437.1	3.149×10^{18}	463.8
45	427.0	3.077×10^{18}	453.1
48	420.0	3.026×10^{18}	445.6
50	438.5	3.160×10^{18}	465.3
51	424.4	3.059×10^{18}	450.4
52	432.0	3.113×10^{18}	458.4
53	438.1	3.156×10^{18}	464.8
54	413.5	2.979×10^{18}	438.8
55	435.6	3.138×10^{18}	462.2
56	431.0	3.106×10^{18}	457.4

Table 3.25: Activation parameters of the proton capture measurements.

E_p(lab) [MeV]	E_p(c.m.) [MeV]	Accelerator	Sample	t_{act} [s]	$< I_p >$ [μA]	Φ_{tot} [p]
8.99	8.91	Cyclotron	13	2700	9.2	1.55×10^{17}
8.05	7.98	Cyclotron	12	2700	10.2	1.72×10^{17}
6.99	6.92	Cyclotron	11	3600	10.2	2.28×10^{17}
5.92	5.86	Cyclotron	10	5639	8.9	3.14×10^{17}
5.02	4.97	Cyclotron	9	4200	11.5	3.02×10^{17}
5.02	4.97	Cyclotron	1	5400	10.3	3.47×10^{17}
5.00	4.95	Cyclotron	56	5400	11.6	3.91×10^{17}
4.46	4.42	Cyclotron	3	9000	9.6	5.40×10^{17}
4.53	4.49	Cyclotron	38	7646	10.8	5.17×10^{17}
4.53	4.49	Cyclotron	39	14510	11.0	9.95×10^{17}
4.26	4.22	Cyclotron	40	7101	12.1	5.37×10^{17}
4.26	4.22	Cyclotron	41	14400	12.2	10.90×10^{17}
4.02	3.98	Cyclotron	4	7200	11.2	5.03×10^{17}
4.02	3.98	Cyclotron	5	10800	11.7	7.85×10^{17}
3.98	3.94	Cyclotron	42	7265	14.6	6.61×10^{17}
3.98	3.94	Cyclotron	43	14669	14.7	13.50×10^{17}
3.76	3.72	Cyclotron	44	7200	11.0	4.92×10^{17}
3.76	3.72	Cyclotron	45	14500	11.0	9.98×10^{17}
3.52	3.49	Cyclotron	6	18000	9.6	10.80×10^{17}
3.50	3.47	Van de Graaff	7	7200	11.9	5.32×10^{17}
3.50	3.47	Van de Graaff	8	18000	14.5	16.30×10^{17}
3.50	3.47	Van de Graaff	48	7400	17.7	8.15×10^{17}
3.25	3.22	Van de Graaff	50	7200	11.4	5.13×10^{17}
3.25	3.22	Van de Graaff	51	21600	11.9	16.00×10^{17}
3.00	2.97	Van de Graaff	52	7200	13.1	5.91×10^{17}
3.00	2.97	Van de Graaff	53	36000	12.2	27.30×10^{17}
2.75	2.72	Van de Graaff	54	7385	12.9	5.95×10^{17}
2.75	2.72	Van de Graaff	55	36000	13.1	29.50×10^{17}
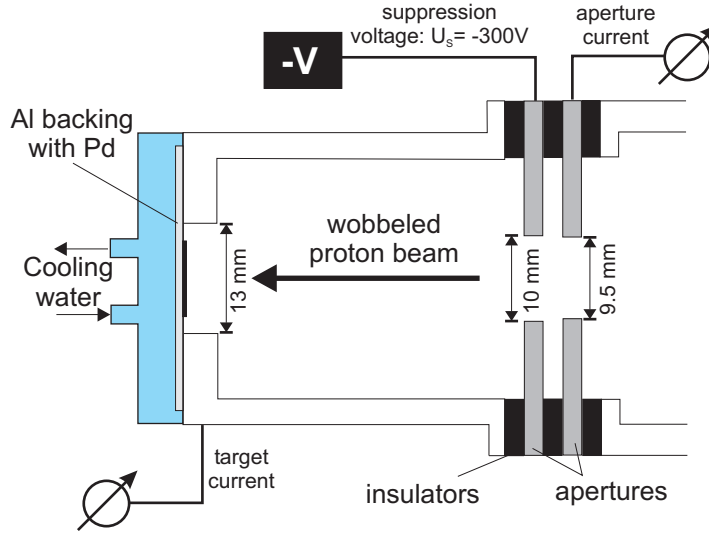
Figure 3.8: Experimental setup at the PTB.

Table 3.25). Since we have a constant proton flux, the number of activated atoms N_{act} directly after the irradiation is described by Eq. 3.1 but here k_γ is negligible due to the thin (460 nm) Pd layers. The cross section at the respective proton energy can then be calculated via

$$\sigma(E_p)[barn] = \frac{N_{act} \; \lambda \; t_{act} \; 10^{24}}{H \; N \; \Phi_{tot} \; (1 - e^{-\lambda \; t_{act}})}.$$ (3.14)

H is the natural abundance of the respective Pd isotope (see Table 3.23), Φ_{tot} the collected proton charge during the activation time t_{act} (Table 3.25), and λ the decay constant. N is the area density of the Pd in units of [atoms cm^{-2}]. Finally the cross section has to be corrected for the coincidence summing effect of the respective γ transition.

3.5.4 Coincidence-summing corrections

For the measurement of the induced activity two HPGe detectors were used (see efficiency curves in Fig. 3.9). The FZK detector is a 100% n-type coaxial detector with a crystal volume of 370 cm^3 and a thin carbon window. Since we used this detector only in 89 mm distance, the summing corrections are low and were estimated with one sample measured at 164 mm distance. The result was in perfect agreement compared to the summing correction calculated with the peak efficiencies in the following equations.

The PTB detector was used at two distances (P1= 15 mm and P3= 135 mm). For this detector the total efficiencies were available (see Fig. 3.9) and were used for the calculation of coincidence summing corrections.
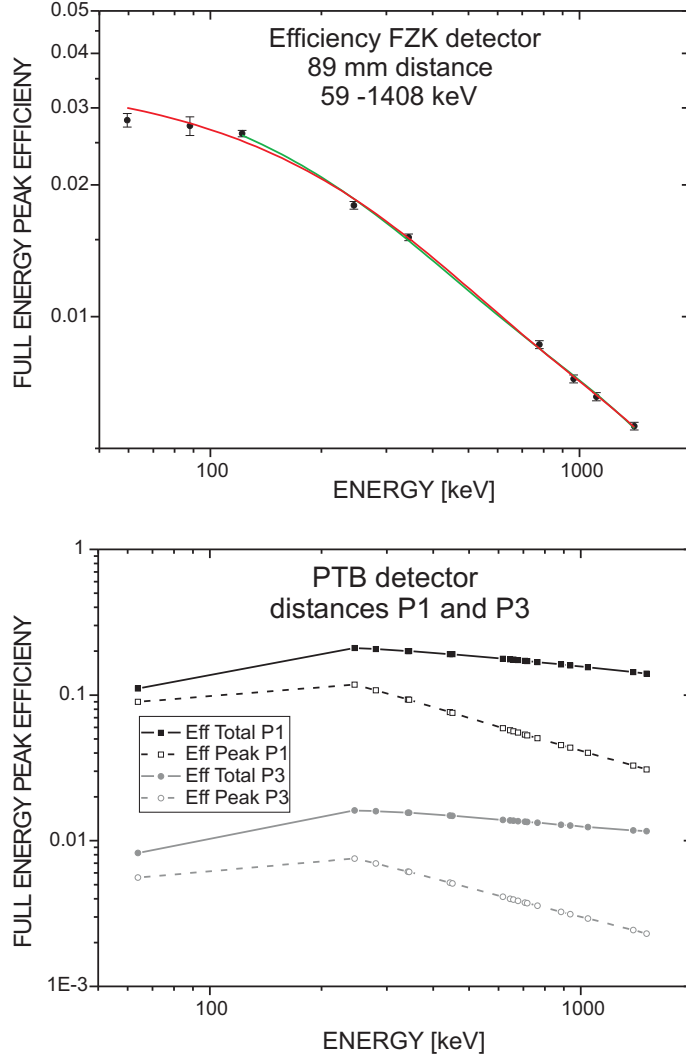
Figure 3.9: Efficiency curves of the HPGe detectors used in the proton-capture measurements.

Coincidence summing occurs when two or more γ rays are emitted within the resolving time of the detector [65]. The probability for coincidence summing increases with increasing total efficiency, thus with decreasing source-detector distance but is independent of the count rate. For the following we take the simple assumptions that no angular correlation exists between the γ rays and all β radiation is absorbed in the detector window. If we take the cascade γ_1, γ_2, γ_3, and $\gamma_1+\gamma_2=\gamma_3$, in absence of coincidence summing, the count rate C_{10} in the full energy peak is

$$C_{10} = A \ I_{\gamma,1} \ \varepsilon_1. \tag{3.15}$$

with the source activity A, the γ-ray intensity I_γ, and the peak efficiency ε_1 of γ-ray γ_1. Taking into account summing , the count rate in the full-energy peak of γ_1 will be smaller, since a fraction of γ_1 and γ_2 can merge to γ_3. The probability of counting

γ_2 is equal to the total efficiency ε_{t2}, and we get

$$C_1 = A\ I_{\gamma,1}\ \varepsilon_1 - A\ I_{\gamma,1}\ \varepsilon_1\ \varepsilon_{t2} = A\ I_{\gamma,1}\ \varepsilon_1(1 - \varepsilon_{t2}). \qquad (3.16)$$

The correction factor S_1

$$S_1 = \frac{C_{10}}{C_1} = \frac{1}{1 - \varepsilon_{t2}} \qquad (3.17)$$

describes the ratio of the count rate derived without and with summing correction. For γ_2 the situation is similar, and we get

$$C_2 = A\ I_{\gamma,2}\ \varepsilon_2 - A\ I_{\gamma,2}\ \varepsilon_2\ \varepsilon_{t1} = A\ I_{\gamma,2}\ \varepsilon_2(1 - \varepsilon_{t1}). \qquad (3.18)$$

and analogous the correction factor S_2

$$S_2 = \frac{C_{20}}{C_2} = \frac{1}{1 - \varepsilon_{t1}}. \qquad (3.19)$$

The correction for the sum peak at γ_3 is different, since γ_1 and γ_2 lead to additional events compared to the count rate without summing:

$$C_3 = A\ I_{\gamma,3}\ \varepsilon_3 + A\ I_{\gamma,1}\ \varepsilon_1\ \varepsilon_2. \qquad (3.20)$$

And the correction factor S_3 becomes

$$S_3 = \frac{C_{30}}{C_3} = \frac{1}{1 + \frac{I_{\gamma,1}\ \varepsilon_1\ \varepsilon_2}{I_{\gamma,3}\ \varepsilon_3}}. \qquad (3.21)$$

with the peak efficiencies ε_1 and ε_2. Note that the total efficiency ε_{tx} does not appear here.

3.5.5 Error analysis

The energy loss of the proton beam in the Pd layer was calculated using the program SRIM 2003 [66] with the respective ion stopping and range tables. The samples have an average palladium thickness of 460 nm, thus the energy loss ranges between 29 keV at 2.75 MeV and 13 keV at 9 MeV. The estimated uncertainty of the proton energy is 0.2 %, leading to total uncertainties ΔE_{total} (see Table 3.26) between 31 and 34 keV. The effective center-of-mass energy $E_{c.m.}^{eff}$ is the center of the energy bin with symmetric error bars, and calculated via $E_{c.m.} - \frac{1}{2} \cdot \frac{\delta E}{\delta x}$.

The total uncertainty of the measured cross sections increases with decreasing proton energy due to increasing statistical errors (see Table 3.27). An exception is the activity measurement of ^{105}Ag, since its favorable half-life of 41.29 d allowed long-time counting over several days.

The systematic error consists of the uncertainties in the efficiency curves of the detectors (2%), the determination of the sample mass via XRF (1.5%), and the respective uncertainties of γ-ray intensities and isotopic abundances [43], and are listed for each product nucleus in Tables 3.28, 3.29, 3.30, and 3.31.

Table 3.26: Total energy uncertainty calculated from the energy losses for a mean sample thickness of 460 nm and 0.2% energy uncertainty from the accelerator.

$E_{c.m}$	$E_{c.m.}^{eff}$	ΔE_{acc}	$-\frac{\delta E}{\delta x}$	ΔE_{total}
[MeV]	[MeV]	[MeV]	[MeV]	[MeV]
8.906	8.900	0.018	0.013	0.031
7.975	7.968	0.016	0.015	0.031
6.925	6.917	0.014	0.016	0.030
5.865	5.856	0.012	0.018	0.030
4.968	4.958	0.010	0.020	0.030
4.947	4.937	0.010	0.020	0.030
4.488	4.477	0.009	0.022	0.031
4.220	4.209	0.008	0.022	0.030
3.943	3.931	0.008	0.023	0.031
3.725	3.713	0.007	0.024	0.031
3.467	3.455	0.007	0.025	0.032
3.220	3.207	0.006	0.026	0.032
2.972	2.958	0.006	0.028	0.034
2.724	2.710	0.005	0.029	0.034

Table 3.27: Statistical uncertainties in [%].

$E^{eff}_{c.m.}$	^{103}Ag	^{105}Ag	^{106}Ag^m	^{110}Ag^m
[MeV]	%	%	%	%
8.91	–	–	–	0.4
7.98	–	–	–	1.1
6.93	14.7	–	–	1.2
5.87	4.8	–	–	1.5
4.96	3.0	1.1	4.7	3.3
4.94	3.0	0.9	3.4	3.3
4.48	2.9	0.3	3.0	4.2
4.41	2.5	0.7	10.0	3.7
4.21	3.8	0.2	8.2	3.5
3.97	3.6	0.8	10.3	5.9
3.93	3.2	0.2	9.0	3.1
3.71	4.4	0.8	12.0	8.1
3.48	–	1.3	6.0	10.0
3.46	4.5	0.9	10.8	6.7
3.46	4.1	0.4	7.5	13.9
3.21	5.9	0.5	8.1	–
2.96	10.0	0.7	–	–
2.71	13.0	0.7	–	–

Table 3.28: Systematic errors for the ^{102}Pd(p,γ) measurement.

	Uncertainty (^{103}Ag) [%]				
Source	119 keV	148 keV	244 keV	267 keV	1274 keV
Isotopic abundance			0.98		
Detector efficiency			2.0		
Sample mass (XRF)			1.5		
γ-ray intensity	2.24	1.77	5.88	2.99	3.19
Total uncertainty	3.50	3.21	6.47	4.02	4.17

Table 3.29: Systematic errors for the ^{104}Pd(p, γ) and ^{105}Pd(p, n) measurements.

	Uncertainty (^{105}Ag) [%]					
Source	64 keV	280 keV	344 keV	443 keV	645 keV	645 keV
Isotopic abundance ^{104}Pd			0.72			
Isotopic abundance ^{105}Pd			0.36			
Detector efficiency			2.0			
Sample mass (XRF)			1.5			
γ-ray intensity	9.52	5.63	1.45	4.76	5.41	4.42
Total uncertainty	9.88	6.21	3.00	5.44	6.01	5.14

Table 3.30: Systematic errors for the ^{105}Pd(p, γ) and ^{106}Pd(p, n) measurements.

	Uncertainty (^{106}Ag^m) [%]			
Source	451 keV	717 keV	748 keV	1046 keV
Isotopic abundance ^{105}Pd			0.36	
Isotopic abundance ^{106}Pd			0.11	
Detector efficiency			2.0	
Sample mass (XRF)			1.5	
γ-ray intensity	2.48	2.77	2.91	3.38
Total uncertainty	3.54	3.75	3.86	4.22

Table 3.31: Systematic errors for the ^{110}Pd(p, n) measurement.

	Uncertainty (^{110}Ag^m) [%]				
Source	658 keV	707 keV	764 keV	885 keV	938 keV
Isotopic abundance ^{110}Pd			0.77		
Detector efficiency			2.0		
Sample mass (XRF)			1.5		
γ-ray intensity	0.32	0.43	0.93	0.55	1.75
Total uncertainty	2.63	2.65	2.78	2.67	3.15

Chapter 4

Neutron-capture results

4.1 General

The experimental neutron spectrum of the $^7\mathrm{Li}(p,n)^7\mathrm{Be}$ reaction approximates a Maxwellian distribution with $kT = 25.0 \pm 0.5$ keV almost perfectly [42] (see Fig. 3.1). The cutoff at $\mathrm{E}_n = 106$ keV and the slightly different shape of this spectrum requires a correction for obtaining the exact Maxwellian averaged cross section $<\sigma>_{kT} = \frac{<\sigma v>}{v_T}$ at the temperature T:

$$\frac{<\sigma>_{kT}}{NF} = \frac{2}{\sqrt{\pi}} \frac{\int^{res} \sigma(E_n) \ E_n \ e^{-E_n/kT} \ dE_n \ + \ \int^{unres} \frac{\sigma(E_n)}{NF} \ E_n \ e^{-E_n/kT} \ dE_n}{\int^{res+unres} E_n \ e^{-E_n/kT} \ dE_n}.$$

(4.1)

In this equation, $\frac{\sigma(E_n)}{NF}$ is the normalized energy-dependent cross section and E_n the neutron energy. $\int^{res}$ and $\int^{unres}$ denote the integration over the resolved and unresolved resonance region. The factor $v_T = \sqrt{2kT/\mu}$ denotes the most probable velocity with the reduced mass μ. The normalization factor NF is deduced from a comparison between the experimental cross section σ_{exp} and the cross sections derived by folding the experimental distribution with the respective energy-dependent neutron cross section, σ_{eval} (see Table 4.2).

The proper Maxwellian averaged cross sections as a function of thermal energy kT between 5 and 260 keV can then be calculated from the normalized cross section. "Normalized" in this context means that the resolved resonance region was kept constant (Table 4.1), whereas the unresolved region was shifted by the normalization factor. This method was chosen because most of the resonances are experimental [59] but subject to the often underestimated experimental uncertainty. A more accurate but time- and (wo)manpower-consuming way is described in Section 7.2.

4.2 Energy-dependent cross section data

For each isotope the databases Joint Evaluated Fission and Fusion General Purpose File (JEFF), Japanese Evaluated Nuclear Data Library (JENDL), and Evaluated

Nuclear Data File (ENDF) were searched for energy-dependent cross sections. In all cases the most recent version of the databases (JEFF 3.1 [67], JENDL 3.3 [68], and ENDF-B/VI.8 [69]) were used, as provided in the online database JANIS [70], which are partially based on experimental resonance parameters [59, 71].

The trends of the energy-dependent neutron cross section curves are similar for each isotope. Nevertheless deviations become visible from the cross sections deduced with our experimental neutron distribution in Table 4.2. These originate from differences in the resonance strengths and the number of resonances, which were taken into account, and also the range of the resolved resonance region (Table 4.1). The unresolved resonance region is in most cases deduced from Hauser-Feshbach calculations using a Moldauer potential. In the cases of ^{130,132}Ba and ^{174}Hf the JEFF 3.1 dependencies were adopted from JENDL-3.3. The unresolved region is in these cases calculated with the spherical optical and statistical model code CASTHY [72]. The observed level spacing is determined here to reproduce the calculated capture cross section. More specifically, for ^{132}Ba the γ-ray strength function was adjusted to reproduce the available experimental capture cross section of [73]. For ^{174}Hf the available resonance parameters from JENDL-3.3 were updated up to 200 eV with recent TOF results [74]. Above that energy the resonance parameters were taken from ENDF/B-VI and JENDL-3.3. The energy range beyond 50 keV was calculated with CASTHY [72]. The low energy region was in all cases deduced by a $1/v$ extrapolation from the thermal cross section at 25.3 meV. It should be emphasized here that the Maxwellian averaged cross sections, which we calculated for p-process energies of kT=170-260 keV, thus are only semi-experimental, since the energy-dependencies we used are deduced from either Hauser-Feshbach calculations using the Moldauer potential (for ^{74}Se, ^{84}Sr, ^{102}Pd, and ^{120}Te) or the code CASTHY. The following subsections present the respective energy-dependencies.

Table 4.1: Extension of the resolved resonance region (in eV) in different databases. *JEF 2.2: 9-300 eV. "–" denotes that only unresolved resonances are available.

Isotope	JEFF 3.1 [eV]	JENDL 3.3 [eV]	ENDF-B/VI.8 [eV]
^{74}Se	8-2400	8-2600	8-2400
^{84}Sr	100-3500	–	100-3500
^{102}Pd	60-397	60-250	–
^{120}Te	–	–	–
^{130}Ba	20-2530	20-2530	–
^{132}Ba	–	–	–
^{174}Hf	4-220*	4-220	4-230

Table 4.2: Overview of cross sections and normalization factors derived by folding the respective database with the experimental neutron spectrum. All values are total (n, γ) cross sections. * JEF 2.2 value. JEFF 3.1 yields 944 mb. ** Value not used due to abnormal spectrum (see Fig. 4.3).

Isotope	Exp.		JEFF 3.1		JENDL 3.3		ENDF-B/VI.8		NON-SMOKER	
	σ_{exp}	NF	σ_{eval}	NF	σ_{eval}	NF	σ_{eval}	NF	σ_{eval}	NF
	[mb]		[mb]		[mb]		[mb]		[mb]	
^{74}Se	281	1.000	160	0.568	207	0.736	160	0.568	206	0.731
^{84}Sr	301	1.000	234	0.779	–	–	233	0.774	324	1.078
^{102}Pd	376	1.000	203	0.540	389	1.035	(459)**	(1.221)	366	0.973
^{120}Te	497	1.000	426	0.857	292	0.588	433	0.871	504	1.015
^{130}Ba	746	1.000	722	0.968	718	0.962	–	–	782	1.048
^{132}Ba	393	1.000	452	1.150	450	1.145	–	–	453	1.152
^{174}Hf	990	1.000	1007*	1.017	941	0.951	686	0.693	769	0.777

4.2.1 ^{74}Se(n,γ)

For ^{74}Se energy-dependent cross section data was available from all three big libraries. JEFF 3.1 and ENDF-B/VI.8 are identical, whereas JENDL 3.3 has more resolved resonances up to 2600 eV. For the calculation of Maxwellian averaged cross sections the normalized energy-dependence of JEFF 3.1 was used.
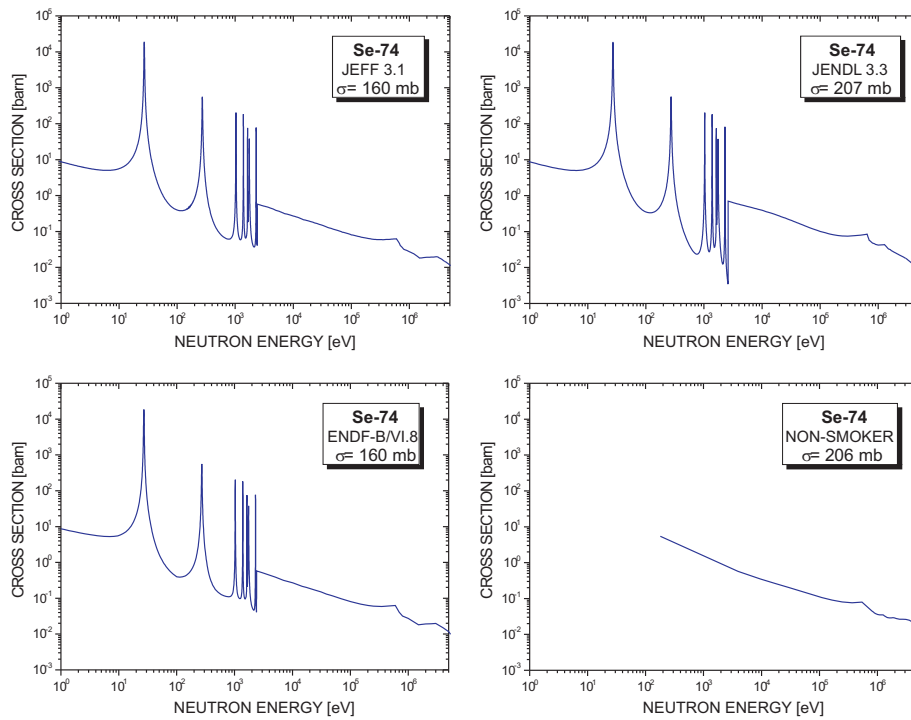
Figure 4.1: Evaluated energy-dependent cross sections for ^{74}Se.

4.2.2 ^{84}Sr(n,γ)

For ^{84}Sr identical energy-dependent cross section data was only available from JEFF 3.1 and ENDF-B/VI.8. For the calculation of Maxwellian averaged cross sections this normalized energy-dependence was used.
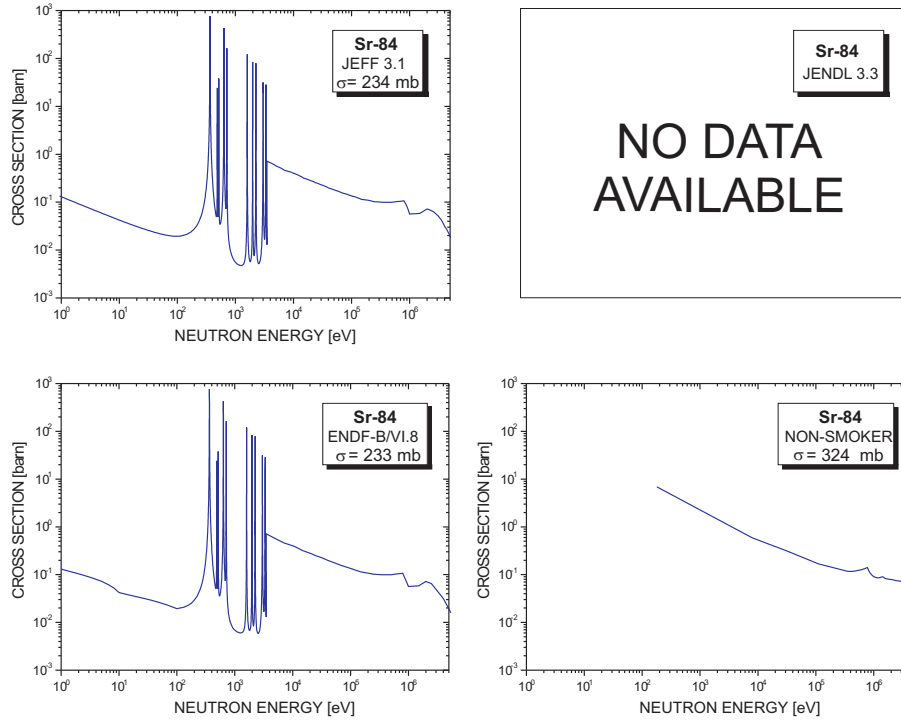
Figure 4.2: Evaluated energy-dependent cross sections for ^{84}Sr.

4.2.3 ^{102}Pd(n,γ)

For ^{102}Pd energy-dependent cross section data with one large resonance was provided by JEFF 3.1 and JENDL 3.3. These two differ only in the beginning of the unresolved resonance region (397 eV vs. 250 eV). The unresolved resonance region in the JENDL curve is a factor of 3 higher which causes the large difference in the calculation of the cross section with the experimental neutron distribution.

ENDF-B/VI.8 neglects the resonance structure and yields a rather high average cross section (given in brackets in Table 4.2). For the calculation of Maxwellian averaged cross sections the normalized energy-dependencies of JEFF 3.1 and JENDL 3.3 were used. The results in Table 4.3 correspond to the mean value of the MACS derived with JEFF and JENDL.
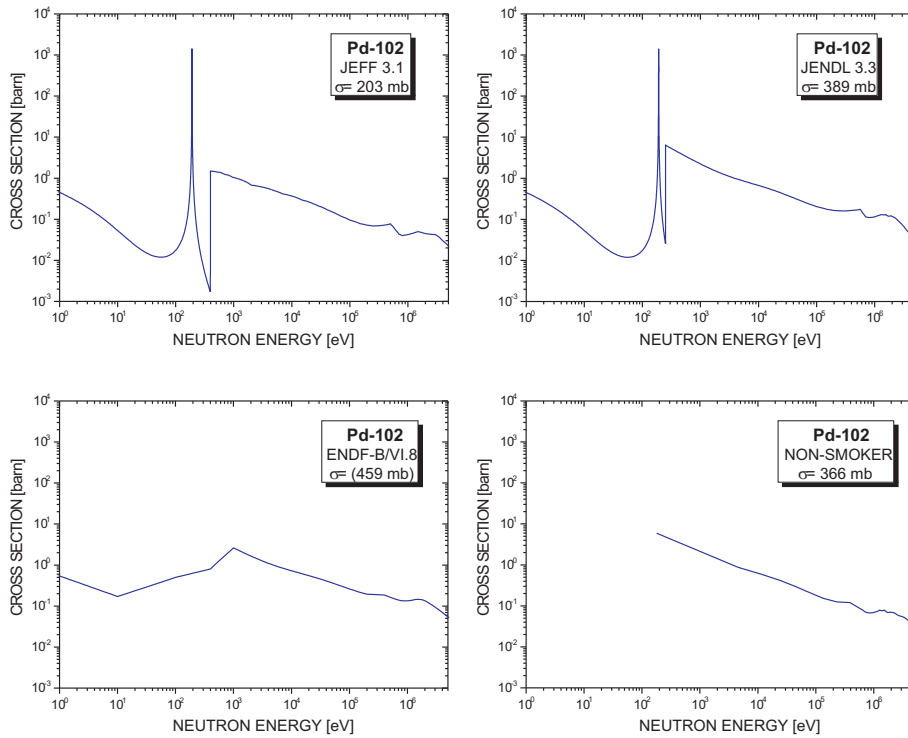
Figure 4.3: Evaluated energy-dependent cross sections for ^{102}Pd.

4.2.4 ^{120}Te(n,γ)

For ^{120}Te the energy-dependent cross section data from the three big libraries consists only of unresolved resonances. They differ in the beginning of this region (JEFF and ENDF-B: 100 eV; JENDL: 68 eV) and in the resonance strength.

For the calculation of Maxwellian averaged cross sections the normalized energy-dependencies of JEFF 3.1 and JENDL 3.3 were used.
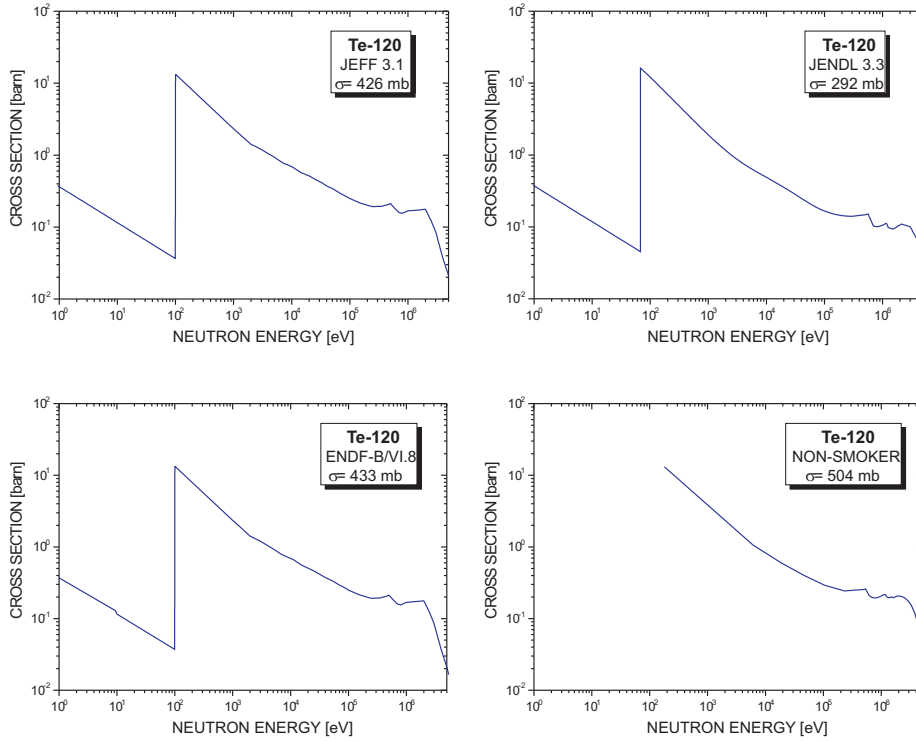
Figure 4.4: Evaluated energy-dependent cross sections for ^{120}Te.

4.2.5 ^{130}Ba(n,γ)

For ^{130}Ba identical energy-dependent cross section data was only available from JEFF 3.1 and JENDL 3.3.

For the calculation of Maxwellian averaged cross sections this normalized energy-dependence was used.
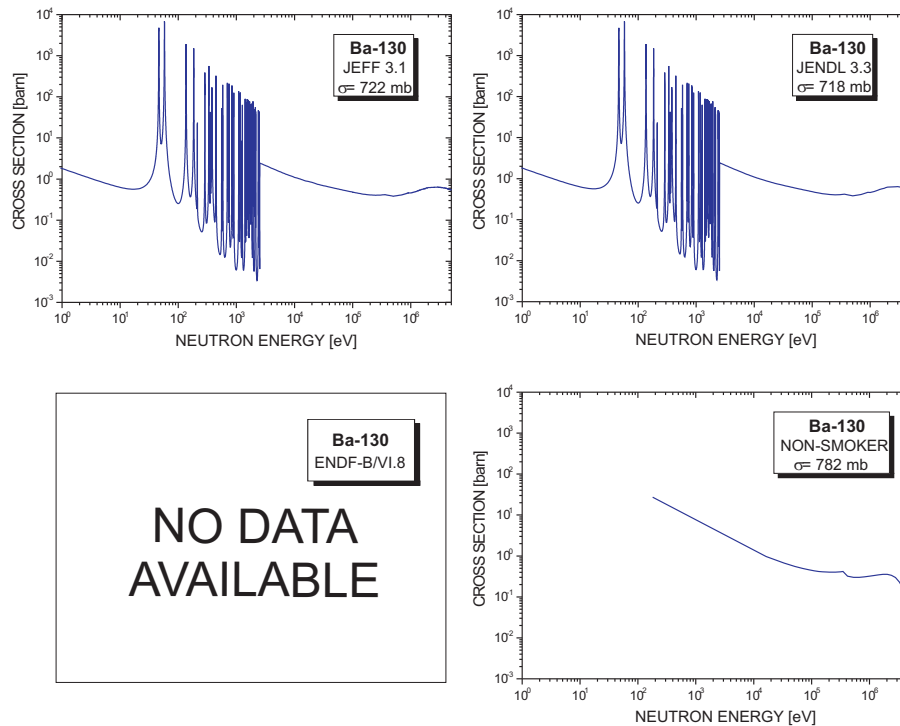
Figure 4.5: Evaluated energy-dependent cross sections for ^{130}Ba.

4.2.6 ^{132}Ba(n,γ)

For ^{132}Ba identical energy-dependent cross section data was only available from JEFF 3.1 and JENDL 3.3. Both libraries provide only unresolved resonances starting from 68 eV.

For the calculation of Maxwellian averaged cross sections this normalized energy-dependencies was used.
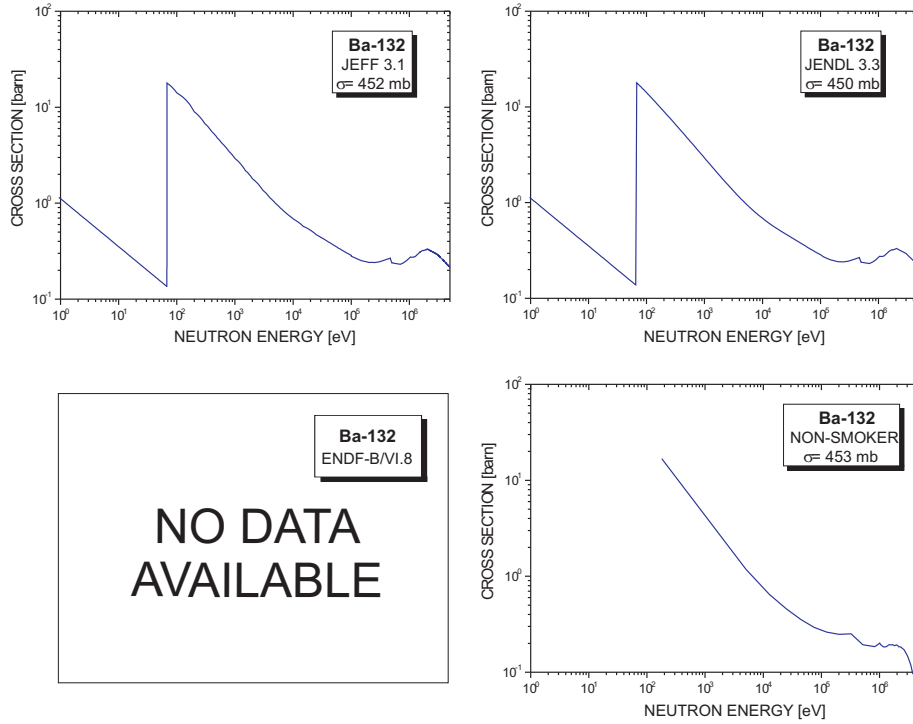
Figure 4.6: Evaluated energy-dependent cross sections for ^{132}Ba.

4.2.7 ^{174}Hf(n,γ)

Energy-dependent cross sections were available from all three libraries. The different cross sections in Table 4.2 are caused by the different height of the unresolved resonance region.

However, as can be seen for JEFF in Fig. 4.7, the data from the older JEF 2.2 reproduces our experimental value best. In [75] was shown that this also holds for ^{180}Hf, where the experimental energy-dependence of [76] is reproduced. Thus, the Maxwellian averaged cross sections were calculated with this older JEF 2.2 energy-dependence.
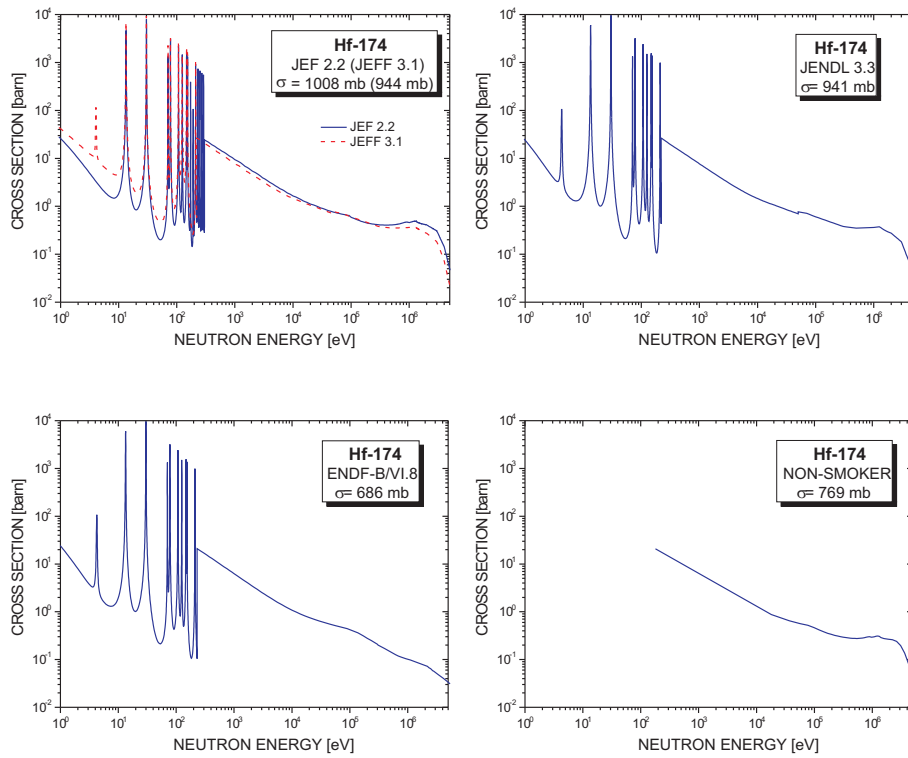
Figure 4.7: Evaluated energy-dependent cross sections for ^{174}Hf.

4.3 Maxwellian averaged cross sections

4.3.1 Maxwellian averaged cross sections for kT= 5-260 keV

Tables 4.3 and 4.4 show the calculated Maxwellian averaged cross sections and stellar enhancement factors (SEF) for kT=5-100 keV and kT=170-260 keV. For comparison also the (previous) recommended data from Bao et al. [26] are given. With exception of ^{130}Ba, where experimental data from [73] was available, all cross sections of [26] are based on semi-empirical estimates. These semi-empirical values are normalized NON-SMOKER cross sections which account for known systematic deficiencies in the nuclear inputs of the calculation. The Maxwellian averaged cross sections were calculated with the energy-dependencies from the evaluated library JEFF and also with the NON-SMOKER energy-dependencies from the Bao et al. compilation (entry "this work + [26]").

4.3.2 Comparison of MACS30 values with theoretical predictions

Fig. 4.8 shows a comparison of the experimental Maxwellian averaged cross section $<\sigma>_{30}$ from this thesis with various theoretical models. For ^{130}Ba, the experimental value from [73] agrees perfectly with our new result. In all other cases, the semi-empirical value from [26] is in good agreement. The Hauser-Feshbach predictions from NON-SMOKER [22] and MOST (version 2002: [24]; version 2005: [25]), and the predictions from Allen et al. [78], Holmes et al. [30], Woosley et al. [79], Harris [80], and Zhao et al. [81] are shown in Fig. 4.8. There is no model which agrees for all seven investigated isotopes. For example, the predictions from Zhao et al. [81] are systematically too low, whereas for ^{84}Sr the older models from Allen [78], Holmes [30], and Harris [80] seem to have the best agreement. It has to be noted that the predictions from the Hauser-Feshbach code MOST differ between the versions from 2002 [24] and 2005 [25]. With exception of ^{84}Sr and ^{174}Hf, the recent MOST 2005 is systematically lower. On the other hand NON-SMOKER gives good agreement within the error bars only for ^{102}Pd, ^{120}Te, and ^{130}Ba.

In Table 4.5 an updated list of Maxwellian averaged cross sections at kT=30 keV is given for all 32 p nuclei. Theoretical predictions from MOST (version from 2005 [25]) and NON-SMOKER [23] are compared with the previous [26] and most recent recommended cross sections. After inclusion of the new values from this work experimental values are missing only for ^{96}Ru, ^{138}La, ^{158}Dy, ^{168}Yb, ^{184}Os, and ^{196}Hg. The semi-empirical value for ^{138}La was not given in [26], since ^{138}La is not produced – even in minor amounts like most p-process nuclei – in the s process. The value given here is a preliminary estimate based on the new cross sections given in Chapter 6.

Fig. 4.9 shows the deviations of MOST and NON-SMOKER predictions relative to the experimental recommended Maxwellian averaged cross section at kT= 30 keV. It is clearly visible from that picture that NON-SMOKER over-predicts 21 of these cross sections, whereas MOST 2005 under-predicts 18 out of 26 cross sections. (The 6 cross sections with semi-empirical estimates mentioned above are not included since they were normalized to NON-SMOKER predictions.)
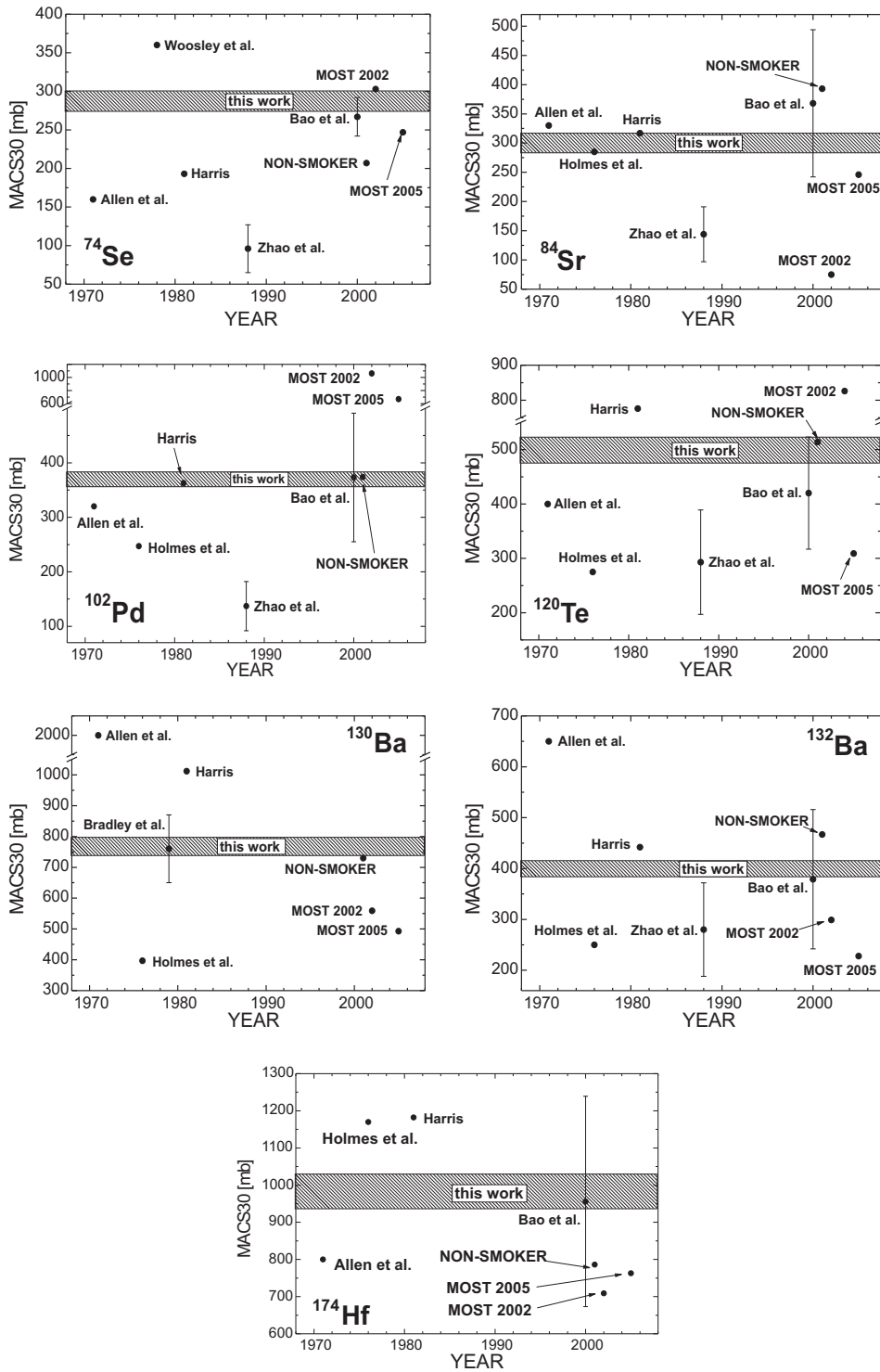
Figure 4.8: Comparison of MACS30 values with predictions.
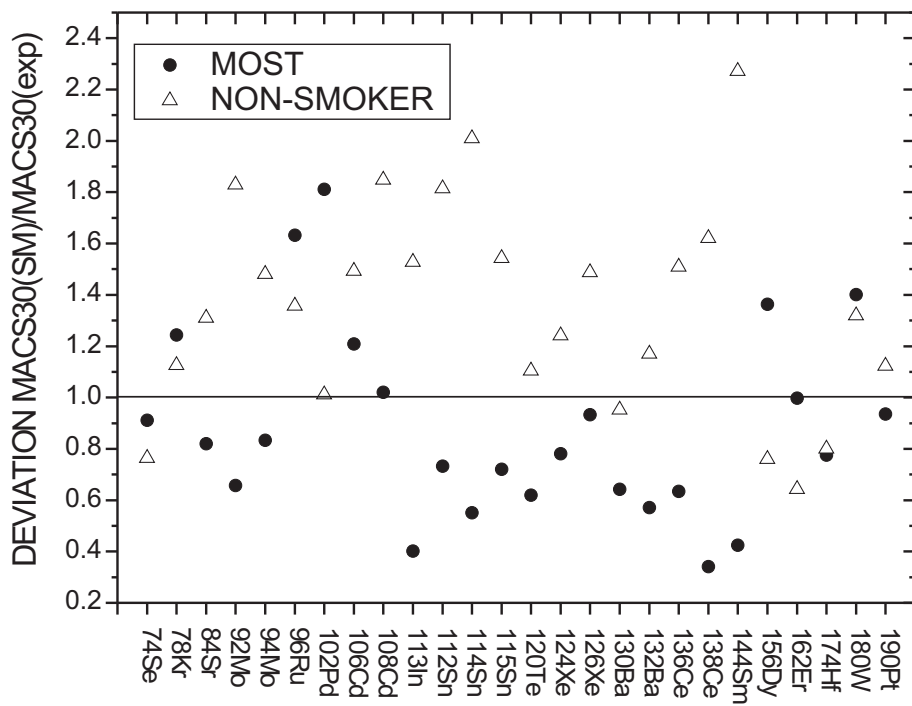
Figure 4.9: Deviation of MACS30 from MOST and NON-SMOKER relative to the experimental value. Not included are p isotopes with semi-empirical cross sections, since they were normalized to NON-SMOKER.

Table 4.3: Maxwellian averaged cross sections $<\sigma>_{kT}$ (in mbarn) and stellar enhancement factors [22] for thermal energies between $5\leq kT\leq100$ keV.

	Thermal energy kT [keV]										
	5	10	15	20	25	30	40	50	60	80	100
^{74}Se											
Bao [26]	677	466	378	327	292	267 (25)	232	209	192	170	156
This work, [77]	775	500	395	337	298	271 (15)	233	209	192	170	157
This work + [26]	687	473	384	332	296	271 (15)	236	212	195	173	158
SEF [22]	1.000	1.000	1.000	1.000	1.000	1.000	1.000	1.000	1.000	1.000	0.999
^{84}Sr											
Bao [26]	885	622	517	446	400	368 (125)	322	286	257	213	185
This work, [77]	683	499	413	361	326	300 (17)	264	240	224	201	187
This work + [26]	721	507	421	364	326	300 (17)	263	233	210	174	151
SEF [22]	1.000	1.000	1.000	1.000	1.000	1.000	1.000	1.000	1.000	1.000	1.001
^{102}Pd											
Bao [26]	894	657	540	466	414	375 (118)	320	283	257	222	199
This work	913	654	533	459	408	370(14)	318	283	260	229	211
This work + [26]	882	648	533	460	408	370 (14)	316	279	254	219	196
SEF [22]	1.000	1.000	1.000	1.000	1.000	1.000	1.000	1.000	1.000	1.002	1.010
^{120}Te											
Bao [26]	1037	708	578	504	455	420 (103)	372	341	318	286	263
This work	1175	834	687	600	542	499 (24)	440	402	375	341	321
This work + [26]	1232	841	687	599	541	499 (24)	442	405	378	340	312
SEF [22]	1.000	1.000	1.000	1.000	1.000	1.000	1.000	1.000	1.000	1.003	1.010
^{130}Ba											
Bao [26, 73]	2379	1284	1031	901	818	760 (110)	683	634	601	556	526
This work	1655	1190	1000	891	819	767 (30)	696	649	616	574	548
This work + [26]	2401	1296	1040	909	826	767 (30)	689	640	607	561	531
SEF [22, 73]	1.000	1.000	1.000	1.000	1.000	1.000	1.000	1.002	1.006	1.023	1.054
^{132}Ba											
Bao [26]	1029	659	526	455	410	379 (137)	339	315	298	276	261
This work	921	641	532	470	429	399 (16)	358	332	313	291	277
This work + [26]	1083	694	554	479	432	399 (16)	357	332	314	291	275
SEF [22]	1.000	1.000	1.000	1.000	1.000	1.000	1.000	1.001	1.004	1.018	1.040
^{174}Hf											
Bao [26]	2453	1436	1219	1100	1019	956 (283)	863	797	746	674	625
This work, [75]	2797	1766	1394	1196	1071	983 (46)	863	784	727	651	604
This work + [26]	2522	1477	1253	1131	1048	983 (46)	887	820	767	693	643
SEF [22]	1.000	1.001	1.012	1.044	1.088	1.133	1.207	1.261	1.304	1.377	1.442

Table 4.4: Maxwellian averaged cross sections $<\sigma>_{kT}$ (in mbarn) and stellar enhancement factors [22] extrapolated to p-process temperatures ($170 \leq kT \leq 260$ keV).

Isotope	$kT=$	170 keV	215 keV	260 keV
^{74}Se	this work, [77]	132	121	111
	this work + [26]	130	119	110
	SEF [22]	1.01	1.02	1.03
^{84}Sr	this work, [77]	164	155	148
	this work + [26]	120	113	109
	SEF [22]	1.02	1.06	1.09
^{102}Pd	this work	178	166	157
	this work + [26]	153	138	127
	SEF [22]	1.11	1.19	1.27
^{120}Te	this work	284	271	261
	this work + [26]	265	251	242
	SEF [22]	1.10	1.18	1.25
^{130}Ba	this work	510	505	507
	this work + [26]	467	445	431
	SEF [22]	1.23	1.33	1.42
^{132}Ba	this work	258	254	253
	this work + [26]	240	226	218
	SEF [22]	1.16	1.22	1.28
^{174}Hf	this work, [75]	531	514	505
	this work + [26]	535	510	495
	SEF [22]	1.64	1.68	1.71

Table 4.5: Status of MACS30 of all 32 p nuclei. Recommended cross sections are taken from Ref. [26], unless another reference is given. *Semi-empirical estimate. The value for ^{138}La is still a preliminary estimate. [1]No value for ^{138}La was given in [26] since it is a pure p-process isotope.

Isotope	Hauser-Feshbach predictions		Recommended MACS30		Comments
	MOST [25]	NON-SMOKER [23]	previous [26]	new	Refs.
	[mbarn]	[mbarn]	[mbarn]	[mbarn]	
^{74}Se	247	207	$267 \pm 25^*$	271 ± 15	this work, [77]
^{78}Kr	388	351	312 ± 26		
^{84}Sr	246	393	$368 \pm 125^*$	300 ± 17	this work, [77]
^{92}Mo	46	128	70 ± 10		
^{94}Mo	85	151	102 ± 20		
^{96}Ru	338	281	238 ± 60	207 ± 8	[82]
^{98}Ru	358	262	$173 \pm 36^*$		
^{102}Pd	670	374	$373 \pm 118^*$	370 ± 14	this work
^{106}Cd	365	451	302 ± 24		
^{108}Cd	206	373	202 ± 9		
^{113}In	316	1202	787 ± 70		
^{112}Sn	154	381	210 ± 12		
^{114}Sn	74	270	134.4 ± 1.8		
^{115}Sn	247	528	342.4 ± 8.7		
^{120}Te	309	551	$420 \pm 103^*$	499 ± 24	this work
^{124}Xe	503	799	644 ± 83		
^{126}Xe	335	534	359 ± 51		
^{130}Ba	493	730	760 ± 110	767 ± 30	this work
^{132}Ba	228	467	$379 \pm 137^*$	399 ± 16	this work
^{136}Ce	208	495	328 ± 21		
^{138}Ce	61	290	179 ± 5		
^{138}La	337	767	$-$ [1]	419 ± 59 *	
^{144}Sm	39	209	92 ± 6		
^{156}Dy	2138	1190	1567 ± 145		
^{158}Dy	1334	949	$1060 \pm 400^*$		
^{162}Er	1620	1042	1624 ± 124		
^{168}Yb	875	886	$1160 \pm 400^*$		
^{174}Hf	763	786	$956 \pm 283^*$	983 ± 46	this work, [75]
^{180}W	751	707	536 ± 60		
^{184}Os	709	789	$657 \pm 202^*$		
^{190}Pt	634	760	677 ± 82		
^{196}Hg	469	372	$650 \pm 82^*$		

4.4   Stellar reaction rates

The reaction rate in $[\text{cm}^3 \cdot \text{s}^{-1}]$ can be calculated from a Maxwellian averaged cross section in [mbarn] via

$$< \sigma v >=< \sigma >_{kT} \cdot v \cdot 10^{-27}. \tag{4.2}$$

The velocity v is here in $[\text{cm} \cdot \text{s}^{-1}]$, and the Maxwellian averaged cross section $< \sigma >_{kT}$ in $[10^{-27} \text{ cm}^2]$. If we now transform the velocity v $[\text{cm} \cdot \text{s}^{-1}]$ in terms of T_9 [GK], we get

$$v = 4.07651 \times 10^8 \cdot \sqrt{T_9/\mu}. \tag{4.3}$$

The energy kT [keV] is calculated from T_9 [GK] with

$$T_9 = kT \cdot \frac{11.6045}{1000}. \tag{4.4}$$

With the aforementioned equations, and inclusion of the SEF (stellar enhancement factor), the stellar reaction rate can be determined via

$$N_A < \sigma v >= SEF \cdot 26445.5 \cdot < \sigma >_{kT} \cdot \sqrt{kT/\mu} \tag{4.5}$$

with μ being the reduced mass and N_A the Avogadro constant. The units for $<\sigma>_{kT}$, the thermal energy kT and the reaction rate $N_A < \sigma v >$ are [mbarn], [keV] and [mole^{-1} cm^3 s^{-1}], respectively. The following Tables 4.6 and 4.7 lists the stellar reaction rates for all seven measured isotopes. Table 4.6 shows the reaction rates calculated from the (normalized) Maxwellian averaged cross section using evaluated energy dependencies like JEFF 3.1 [67]. This rate is plotted in Fig. 4.10 with the solid line (label "this work + JEFF"). Table 4.7 lists the reaction rates calculated with the Bao et al. [26] energy dependence which is equal to a "normalized" NON-SMOKER dependence, as can be seen in Fig. 4.10 (dashed line, labelled "this work + Bao"). Both curves are shown in comparison to the original NON-SMOKER rates [22] (dotted line). The normalization at kT=30 keV reveals the different behavior due to the use of different energy dependencies, especially the reason for deviations at higher energies. It has to be emphasized that the plotted temperature dependencies are actually all from Hauser-Feshbach calculations, even the "experimental" rates from the evaluated libraries JEFF, JENDL, and ENDF-B. Thus, different statistical models (as described in Sec. 4.2) with different input parameters are compared here.

In the cases of ^{74}Se and ^{174}Hf both normalized curves are in perfect agreement with exception of the low-energy part below kT=30 keV. ^{84}Sr is conflicting: at higher energies ($kT\geq$120 keV) the normalized curves agree rather well, but they deviate strongly at lower energies. Therefore below 40 keV the "evaluated" energy dependence follows the original NON-SMOKER trend. For ^{102}Pd and ^{132}Ba agreement is found only at lower energies, with increasing discrepancies at higher energy. The data of ^{120}Te and ^{132}Ba exhibit a similar behavior as ^{84}Sr. Around the normalization point the agreement between both normalized curves is good, but beyond the deviation increases with increasing energy. Therefore the "evaluated" curve approaches the original NON-SMOKER predictions.

Table 4.6: Stellar reaction rates (including SEF from Tables 4.3 and 4.4) for thermal energies between $kT=$ 5 keV and 260 keV derived with evaluated databases.

	^{74}Se	^{84}Sr	^{102}Pd	^{120}Te	^{130}Ba	^{132}Ba	^{174}Hf
kT				$N_A < \sigma v >$			
[keV]				[mole^{-1}cm^{3}s^{-1}]			
5	4.61×10^7	4.07×10^7	5.42×10^7	6.98×10^7	9.82×10^7	5.47×10^7	1.67×10^8
10	4.21×10^7	4.20×10^7	5.49×10^7	7.00×10^7	9.99×10^7	5.38×10^7	1.49×10^8
15	4.08×10^7	4.25×10^7	5.49×10^7	7.07×10^7	1.03×10^8	5.47×10^7	1.44×10^8
20	4.01×10^7	4.30×10^7	5.45×10^7	7.13×10^7	1.06×10^8	5.58×10^7	1.42×10^8
25	3.97×10^7	4.33×10^7	5.41×10^7	7.19×10^7	1.09×10^8	5.69×10^7	1.42×10^8
30	3.95×10^7	4.37×10^7	5.38×10^7	7.25×10^7	1.12×10^8	5.80×10^7	1.43×10^8
40	3.93×10^7	4.44×10^7	5.34×10^7	7.39×10^7	1.17×10^8	6.01×10^7	1.45×10^8
50	3.94×10^7	4.52×10^7	5.33×10^7	7.55×10^7	1.22×10^8	6.23×10^7	1.47×10^8
60	3.97×10^7	4.61×10^7	5.34×10^7	7.72×10^7	1.27×10^8	6.47×10^7	1.50×10^8
80	4.06×10^7	4.79×10^7	5.45×10^7	8.13×10^7	1.39×10^8	7.03×10^7	1.55×10^8
100	4.17×10^7	4.99×10^7	5.66×10^7	8.60×10^7	1.53×10^8	7.67×10^7	1.62×10^8
170	4.60×10^7	5.79×10^7	6.85×10^7	1.08×10^8	2.17×10^8	1.03×10^8	3.01×10^8
215	4.79×10^7	6.41×10^7	7.70×10^7	1.24×10^8	2.60×10^8	1.21×10^8	3.35×10^8
260	4.92×10^7	6.91×10^7	8.56×10^7	1.40×10^8	3.08×10^8	1.39×10^8	3.70×10^8

The deviation between both normalized curves at $kT=$ 5 and 260 keV is shown in Table 4.8. The differences at 260 keV originate purely from the comparison of two different statistical models, and range between 1-2% (for ^{74}Se and ^{174}Hf) up to 36% for ^{84}Sr. The differences at $kT=$5 keV have to be taken with caution. The lowest neutron energy provided by NON-SMOKER is 180 eV, higher than some low-lying resonances.

The reason for the S-shaped reaction rate curve of NON-SMOKER for ^{84}Sr is the (n, p) channel opening at E_n(c.m.)=360 keV (see the little hump in Fig. 4.2), as discussed in Sec. 2.3.1. The difference between proton and neutron separation energy, $S_p - S_n =$ 8641 keV - 8529 keV = 112 keV, is also visible in Fig. 4.10 resulting in the minimum in the reaction rate curve. Here, the width fluctuation coefficient W is different from unity and enhances the weaker channel, which is reflected in the decreasing neutron capture cross section.

For ^{84}Sr the normalized temperature dependence of NON-SMOKER is similar to the one of the other statistical model above $kT>$120 keV. This indicates that the other model used different width fluctuation corrections or none at all. There is no channel opening for ^{120}Te and ^{132}Ba but the temperature-dependence of the rates is different. This effect comes from the use of different nuclear properties, such as the proton+nucleus optical potential, the GDR (Giant Dipole Resonance) strength, and/or nuclear level densities.

Table 4.7: Stellar reaction rates (including SEF from Tables 4.3 and 4.4) for thermal energies between $kT=$ 5 keV and 260 keV derived with the energy dependencies of Bao et al. [26].

	^{74}Se	^{84}Sr	^{102}Pd	^{120}Te	^{130}Ba	^{132}Ba	^{174}Hf
kT				$N_A < \sigma v >$			
[keV]				[mole^{-1}cm^{3}s^{-1}]			
5	4.61×10^7	4.06×10^7	5.43×10^7	6.98×10^7	9.82×10^7	5.47×10^7	1.66×10^8
10	4.21×10^7	4.20×10^7	5.50×10^7	7.00×10^7	9.99×10^7	5.38×10^7	1.48×10^8
15	4.07×10^7	4.26×10^7	5.49×10^7	7.07×10^7	1.03×10^8	5.47×10^7	1.45×10^8
20	4.01×10^7	4.29×10^7	5.45×10^7	7.13×10^7	1.06×10^8	5.58×10^7	1.48×10^8
25	3.97×10^7	4.34×10^7	5.42×10^7	7.20×10^7	1.09×10^8	5.69×10^7	1.55×10^8
30	3.95×10^7	4.37×10^7	5.39×10^7	7.26×10^7	1.12×10^8	5.80×10^7	1.62×10^8
40	3.92×10^7	4.44×10^7	5.34×10^7	7.39×10^7	1.17×10^8	6.01×10^7	1.75×10^8
50	3.93×10^7	4.51×10^7	5.32×10^7	7.55×10^7	1.22×10^8	6.24×10^7	1.85×10^8
60	3.96×10^7	4.62×10^7	5.35×10^7	7.71×10^7	1.27×10^8	6.46×10^7	1.95×10^8
80	4.05×10^7	4.78×10^7	5.45×10^7	8.12×10^7	1.39×10^8	7.03×10^7	2.13×10^8
100	4.18×10^7	4.98×10^7	5.66×10^7	8.61×10^7	1.53×10^8	7.65×10^7	2.31×10^8
170	4.63×10^7	5.80×10^7	6.85×10^7	1.08×10^8	2.17×10^8	1.04×10^8	3.01×10^8
215	4.82×10^7	6.41×10^7	7.70×10^7	1.25×10^8	2.61×10^8	1.21×10^8	3.36×10^8
260	4.91×10^7	6.92×10^7	8.54×10^7	1.40×10^8	3.08×10^8	1.39×10^8	3.69×10^8

Table 4.8: Ratio $\frac{Eval}{Bao}$ at $kT=5$ and 260 keV between both normalized reaction rate curves.

kT	^{74}Se	^{84}Sr	^{102}Pd	^{120}Te	^{130}Ba	^{132}Ba	^{174}Hf
$\frac{Eval}{Bao}$(5 keV)	1.13	0.95	1.04	0.95	0.69	0.85	1.11
$\frac{Eval}{Bao}$(260 keV)	1.01	1.36	1.24	1.09	1.18	1.16	1.02
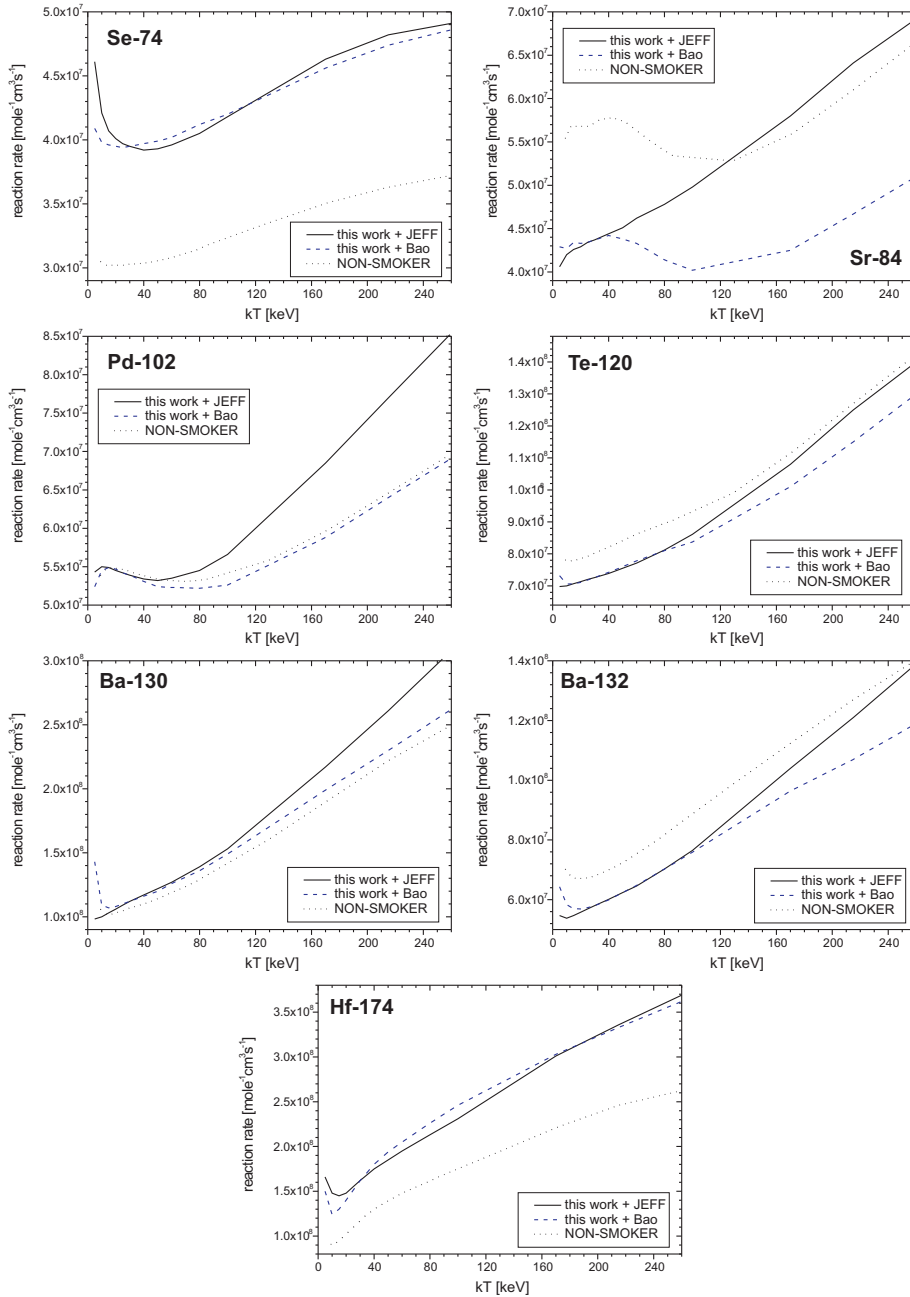
Figure 4.10: Comparison of reaction rates derived with different energy dependencies. Solid line: energy dependence from evaluated data libraries, e.g. JEFF 3.1; dotted line: original NON-SMOKER prediction; dashed line: normalized NON-SMOKER energy dependence from Bao et al. For an explanation of the NON-SMOKER curve of ^{84}Sr, see text.

Chapter 5

Proton-capture results

5.1 $^{102}\mathbf{Pd}(p, \gamma)^{103}\mathbf{Ag}$

The total capture cross section of ^{102}Pd(p, γ) was measured via the five γ transitions at 118.7, 148.2, 243.9, 266.9, and 1273.8 keV. The half life was additionally checked and yielded 68.2 ± 2.4 min, slightly higher than the 65.7 min given in [52]. The following Table 5.1 summarizes the cross section results of the single transitions, including the calculated summing correction factors S_C. Table 5.2 gives the respective weighted average cross section and the S factor. The experimental error bars are the sum of the statistical and systematical error. An error band of $\pm 100\%$ is drawn around the NON-SMOKER curve to show the uncertainty of this prediction for proton-capture reactions. As can be seen at the S-factor plot in Fig. 5.1 we achieve rather good agreement with the NON-SMOKER prediction. The experimental curve cuts the NON-SMOKER curve around 4 MeV, with increasing deviation towards higher energies.

Over the whole energy range we are about a factor of 3 lower than the experimental result from Özkan et al. [61]. They used enriched ^{102}Pd samples which had an area density of 2 mg/cm^2, a factor of 3 higher than our samples. Thus their results exhibit a rather large energy uncertainty, which is 3 times higher (60-90 keV) compared to our results. However, this does not explain the discrepancy between both measurements.
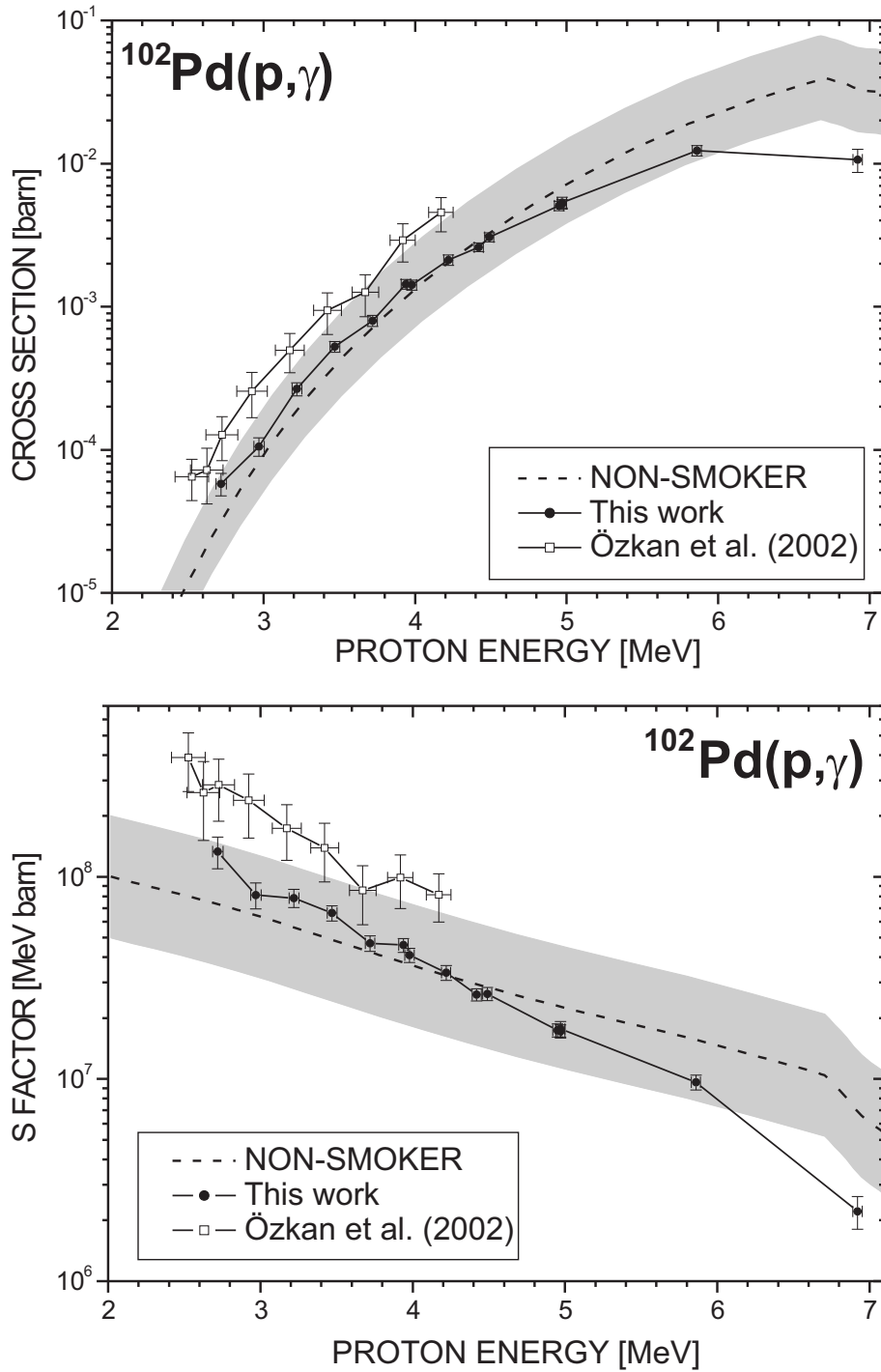
Figure 5.1: Cross section and S factor for ^{102}Pd(p, γ).

Table 5.1: Cross section results of ^{102}Pd(p, γ) from the single γ transitions. The summing correction factor S_C for the FZK detector is shown below the column heads.

E_p(c.m.) [MeV]	σ(119 keV) [barn]	σ(148 keV) [barn]	σ(244 keV) [barn]	σ(267 keV) [barn]	σ(1274 keV) [barn]
S_C	1.030	1.026	1.007	0.932	0.989
2.72	5.453×10^{-5}	5.570×10^{-5}	7.932×10^{-5}	6.043×10^{-5}	7.315×10^{-5}
2.97	1.043×10^{-4}	1.022×10^{-4}	1.329×10^{-4}	1.120×10^{-4}	1.152×10^{-4}
3.22	2.578×10^{-4}	2.654×10^{-4}	2.792×10^{-4}	2.967×10^{-4}	3.139×10^{-4}
3.47	4.839×10^{-4}	4.839×10^{-4}	5.396×10^{-4}	5.594×10^{-4}	5.140×10^{-4}
3.72	7.849×10^{-4}	7.820×10^{-4}	8.024×10^{-4}	9.065×10^{-4}	8.886×10^{-4}
3.94	1.421×10^{-3}	1.383×10^{-3}	1.573×10^{-3}	1.653×10^{-3}	1.604×10^{-3}
3.98	1.395×10^{-3}	1.403×10^{-3}	1.547×10^{-3}	1.609×10^{-3}	1.532×10^{-3}
4.22	2.075×10^{-3}	2.079×10^{-3}	2.260×10^{-3}	2.413×10^{-3}	2.374×10^{-3}
4.42	2.569×10^{-3}	2.562×10^{-3}	2.754×10^{-3}	2.957×10^{-3}	2.756×10^{-3}
4.49	3.007×10^{-3}	3.026×10^{-3}	3.263×10^{-3}	3.395×10^{-3}	3.365×10^{-3}
4.95	5.034×10^{-3}	4.955×10^{-3}	5.338×10^{-3}	5.714×10^{-3}	5.660×10^{-3}
4.97	5.142×10^{-3}	5.079×10^{-3}	5.656×10^{-3}	5.949×10^{-3}	5.673×10^{-3}
4.97	5.227×10^{-3}	5.296×10^{-3}	5.746×10^{-3}	6.247×10^{-3}	5.727×10^{-3}
5.86	1.201×10^{-2}	1.268×10^{-2}	1.317×10^{-2}	1.278×10^{-2}	$-$
6.92	9.954×10^{-3}	1.232×10^{-2}	1.222×10^{-2}	1.027×10^{-2}	$-$

Table 5.2: Weighted cross sections and S factors from the ^{102}Pd(p, γ) measurements. $\Delta\sigma$ and Δ S factor are the respective uncertainties.

E_p^{eff}(c.m.) [MeV]	weighted σ [barn]	Δ σ [barn]	S factor [MeV barn]	Δ S factor [MeV barn]
2.71±0.03	5.79×10^{-5}	1.04×10^{-5}	1.32×10^8	2.35×10^7
2.96±0.03	1.05×10^{-4}	1.55×10^{-5}	8.02×10^7	1.18×10^7
3.21±0.03	2.66×10^{-4}	2.77×10^{-5}	7.76×10^7	8.07×10^6
3.45±0.03	5.25×10^{-4}	4.60×10^{-5}	6.54×10^7	5.73×10^6
3.71±0.03	7.97×10^{-4}	7.03×10^{-5}	4.64×10^7	4.09×10^6
3.93±0.03	1.43×10^{-3}	1.12×10^{-4}	4.54×10^7	3.56×10^6
3.97±0.03	1.42×10^{-3}	1.15×10^{-4}	4.05×10^7	3.28×10^6
4.21±0.03	2.12×10^{-3}	1.77×10^{-4}	3.33×10^7	2.79×10^6
4.41±0.03	2.60×10^{-3}	1.81×10^{-4}	2.59×10^7	1.80×10^6
4.48±0.03	3.06×10^{-3}	2.26×10^{-4}	2.61×10^7	1.93×10^6
4.94±0.03	5.08×10^{-3}	3.81×10^{-4}	1.73×10^7	1.30×10^6
4.96±0.03	5.26×10^{-3}	4.29×10^{-4}	1.74×10^7	1.42×10^6
5.86±0.03	1.23×10^{-2}	1.02×10^{-3}	9.64×10^6	7.99×10^5
6.92±0.03	1.06×10^{-2}	1.96×10^{-3}	2.21×10^6	4.08×10^6

5.2 $^{104}\mathbf{Pd}(p, \gamma)$ and $^{105}\mathbf{Pd}(p, n)$

The total capture cross section of ^{104}Pd(p, γ) into ^{105}Ag could only be measured together with the ^{105}Pd(p, n) reaction ((p, n) threshold $\approx$2.1 MeV), since we used Pd samples of natural composition. The derived cross section σ^+ is thus a mixture of both reaction channels. It was deduced from the γ transitions at 64.0, 280.4, 344.5, and 443.4 keV. The 7.23 min isomeric state in ^{105}Ag could not be determined due to its short half-life. The results are summarized in Table 5.4 with the respective summing correction factors S_C.

As a very first approximation for the separation of the (p, γ) and (p, n) channels the cross section ratios of NON-SMOKER were used. We can determine the "mixed" cross section σ^+ by

$$Z^+ = (11.14\% + 22.33\%) \ N_{Pd} \ \sigma^+ \ \Phi_{tot} \ f_b, \tag{5.1}$$

where 11.14% and 22.33% are the natural isotopic abundances of ^{104}Pd and ^{105}Pd [43], respectively. This is equivalent to

$$Z^+ = (N_{104} \ \sigma_{pg} + N_{105} \ \sigma_{pn}) \ \Phi_{tot} \ f_b, \tag{5.2}$$

where N_{104} and σ_{pg} are the number of ^{104}Pd atoms and the respective ^{104}Pd(p, γ) cross section, and N_{105} and σ_{pn} the number of ^{105}Pd atoms and the ^{105}Pd(p, n) cross section. By comparison of these coefficients, one derives that

$$\sigma^+ \ (N_{104} + N_{105}) = N_{104} \ \sigma_{pg} + N_{105} \ \sigma_{pn}. \tag{5.3}$$

The ratio of these two reaction channels can be deduced from the ratios of the respective NON-SMOKER cross sections in Table 5.3.

The ratio R is defined as $\frac{\sigma_{pn}}{\sigma_{pg}}$, so it follows that $\sigma_{pn} = R \ \sigma_{pg}$. Replacing σ_{pn} in Eq. 5.3 leads to

$$\sigma^+ \ (N_{104} + N_{105}) = N_{104} \ \sigma_{pg} + N_{105} \ R \ \sigma_{pg}, \tag{5.4}$$

which can be transformed to

$$\sigma_{pg} = \frac{\sigma^+ \ (N_{104} + N_{105})}{N_{104} \ + N_{105} \ R}. \tag{5.5}$$

This expression is independent of the amount of Pd atoms, N_{Pd}, and can be shortened to

$$\sigma_{pg} = \frac{\sigma^+ \ (11.14\% \ + \ 22.33\%)}{11.14\% \ + \ 22.33\% \ R}. \tag{5.6}$$

In this way the ^{104}Pd(p, γ) cross section can be separated. The respective ^{105}Pd(p, n) is then calculated from $\sigma_{pn} = R \ \sigma_{pg}$.

Vice versa a "theoretical" σ_{NS}^+ can be calculated from both NON-SMOKER cross sections (Table 5.3) and compared to our experimental data:

$$\sigma_{NS}^+ = \frac{11.14\% * \sigma_{pg} + 22.33\% * \sigma_{pn}}{33.47\%}. \tag{5.7}$$

Table 5.3: Cross section and ratios from NON-SMOKER for ^{104}Pd(p,γ) and ^{105}Pd(p,n). The last column gives the theoretical "mixed" cross section σ_{NS}^+ calculated via Eq. 5.7.

E_p(c.m.) [MeV]	$\sigma(^{104}$Pd$(p,\gamma))$ [barn]	$\sigma(^{105}$Pd$(p,n))$ [barn]	Ratio R $\frac{\sigma_{pn}}{\sigma_{pg}}$	σ_{NS}^+ [barn]
2.50	1.391×10^{-5}	9.970×10^{-6}	0.703	1.115×10^{-5}
2.75	4.351×10^{-5}	3.967×10^{-5}	0.912	4.095×10^{-5}
3.00	1.188×10^{-4}	1.213×10^{-4}	1.021	1.205×10^{-4}
3.25	2.907×10^{-4}	3.127×10^{-4}	1.076	3.054×10^{-4}
3.50	6.438×10^{-4}	7.150×10^{-4}	1.111	6.913×10^{-4}
3.75	1.294×10^{-3}	1.374×10^{-3}	1.062	1.348×10^{-3}
4.00	2.353×10^{-3}	2.903×10^{-3}	1.234	2.720×10^{-3}
4.25	3.903×10^{-3}	5.355×10^{-3}	1.372	4.872×10^{-3}
4.50	6.670×10^{-3}	9.085×10^{-3}	1.362	8.281×10^{-3}
5.00	1.510×10^{-2}	2.422×10^{-2}	1.604	2.119×10^{-2}

The experimental results for the respective mixed cross section σ^+ and the S factor are given in Tables 5.4 and 5.5. These results are shown in comparison to the NON-SMOKER prediction (Table 5.3) in Fig. 5.2. An error band of $\pm100\%$ is drawn around the NON-SMOKER curve to show the uncertainty of this prediction. Our experimental result is within a factor of two in agreement with the NON-SMOKER trend, with increasing deviations towards smaller energies. This trend can be explained by the ^{105}Pd(p,n) channel opening at $E_p \approx 2.1$ MeV, which shifts the ratio R towards smaller numbers and increases the uncertainty. Threshold effects like width fluctuations may be important close to the reaction threshold. Therefore an extrapolation of the isomeric ratio to the threshold may carry large inherent uncertainties as indicated by our results. Further substantiation of our results has to await theoretical modelling of the threshold effects and a following measurement with enriched Pd material.

Tables 5.6 and 5.7 show the weighted cross sections for ^{104}Pd(p,γ) and ^{105}Pd(p,n) disentangled with the NON-SMOKER ratios. For ^{105}Pd(p,n) some data between $E_p=$ 5-9 MeV from a previous measurement of Batij et al. [83] existed which is at $E_p=5$ MeV ($\sigma=0.0133 \pm 0.0014$ barn) a factor of 1.9 lower than our data. The single, disentangled cross sections and S factors show the same trend as the "mixed" cross section σ^+ (Figs. 5.3 and 5.4).
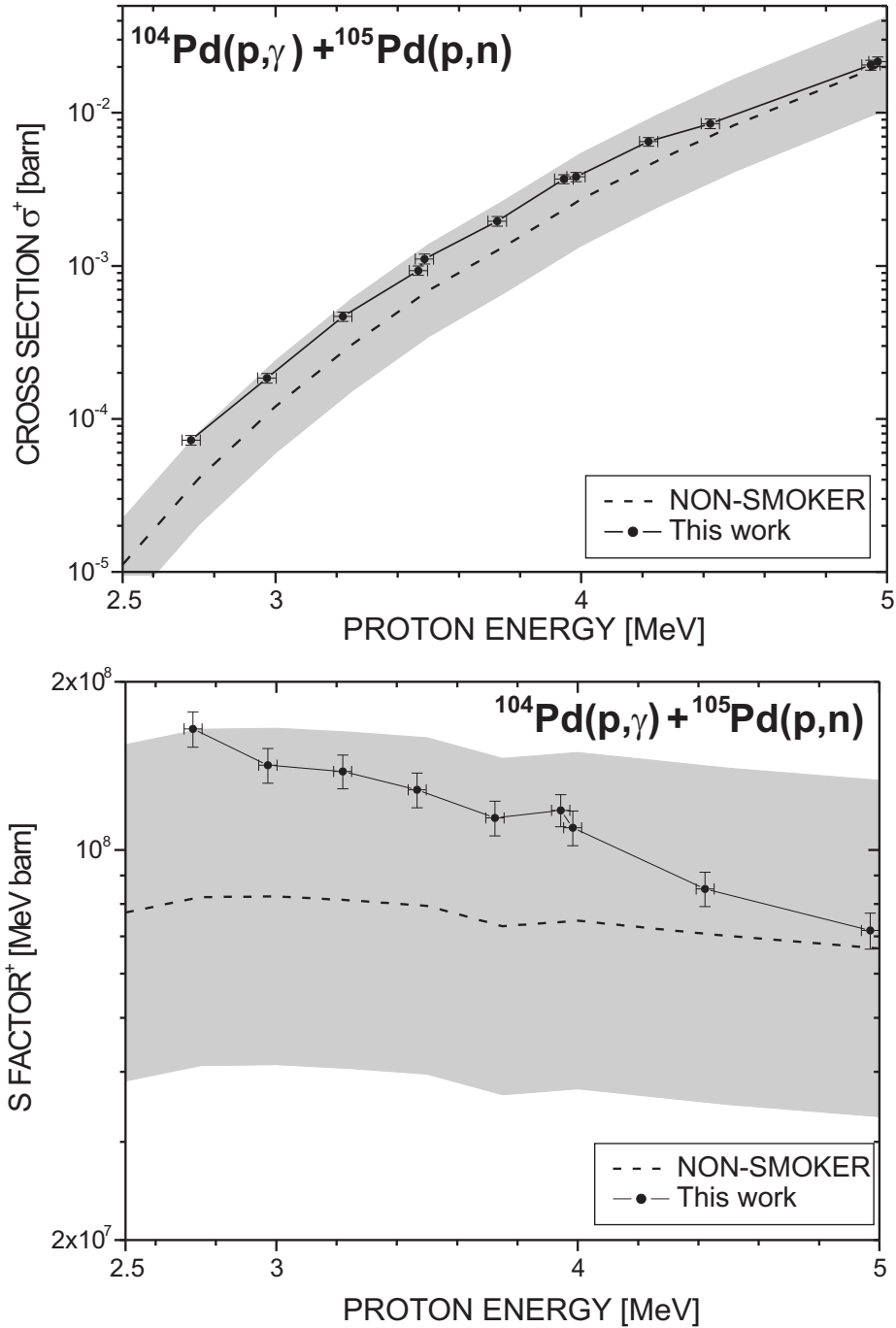
Figure 5.2: "Mixed" cross section σ^+ and S factor for ^{104}Pd(p,γ) and ^{105}Pd(p,n).
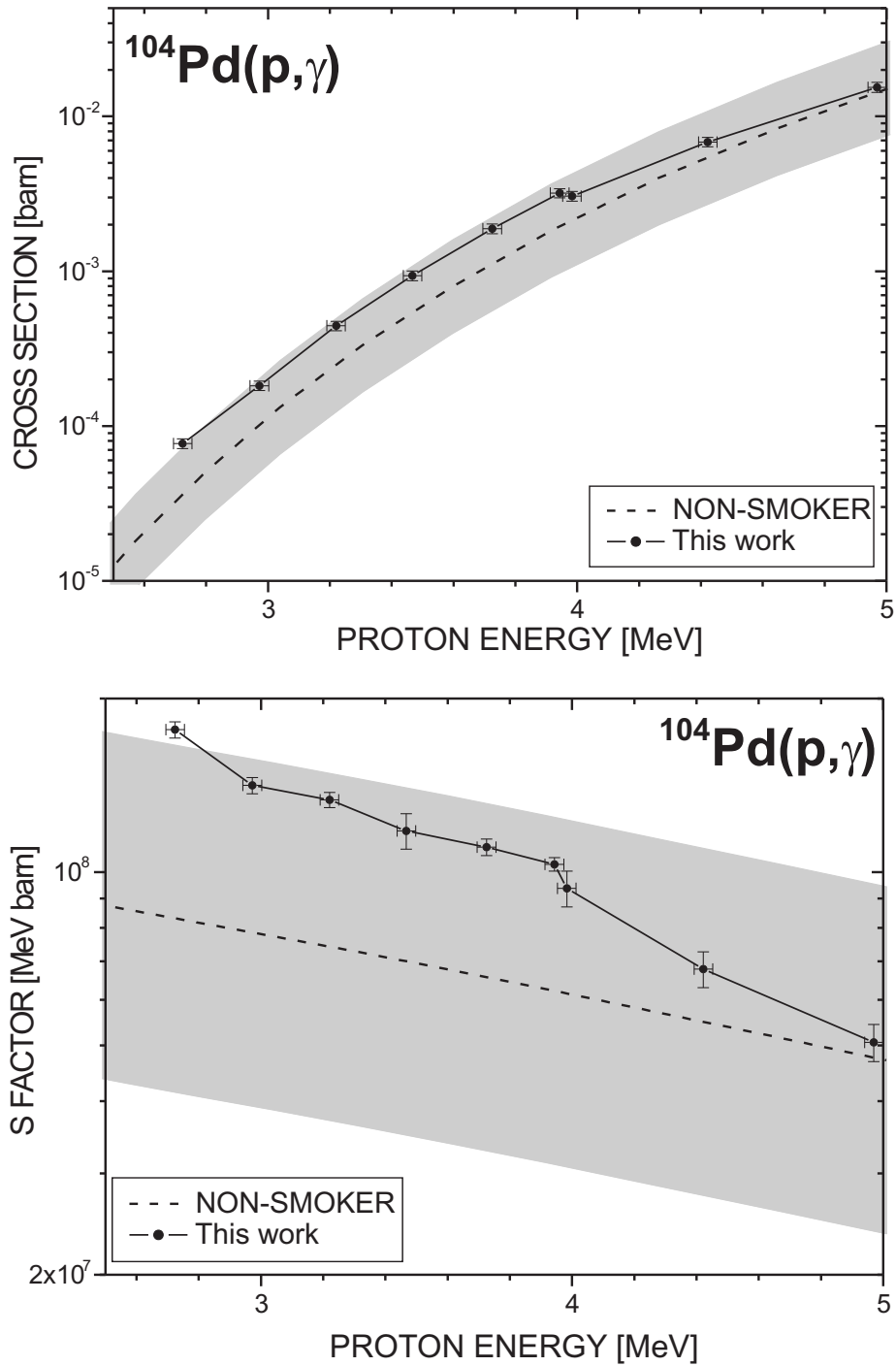
Figure 5.3: Cross sections and S factors (disentangled with NON-SMOKER ratios) for ^{104}Pd(p, γ).
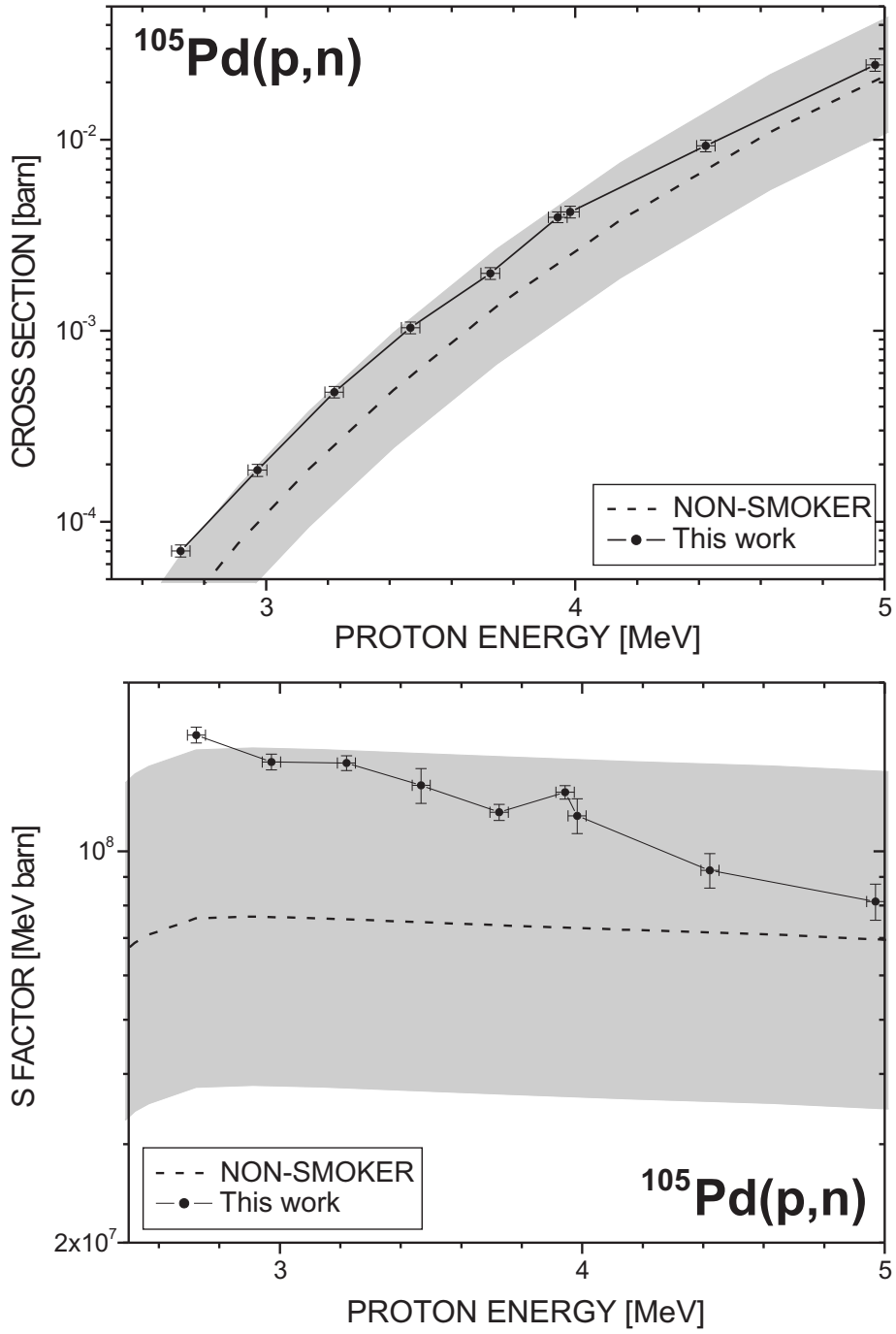
Figure 5.4: Cross sections and S factors (disentangled with NON-SMOKER ratios) for $^{105}\mathrm{Pd}(p, n)$.

Table 5.4: Mixed cross sections σ^+ for the ^{104}Pd(p, γ) and ^{105}Pd(p, n) measurement. The summing correction factor S_C for the FZK detector is shown below the column heads.

E_p^{eff}(c.m.)	σ^+(64 keV)	σ^+(280 keV)	σ^+(344 keV)	σ^+(443 keV)
[MeV]	[barn]	[barn]	[barn]	[barn]
S_C	1.017	1.029	0.992	1.010
2.71±0.03	8.351×10^{-5}	7.595×10^{-5}	7.108×10^{-5}	7.289×10^{-5}
2.96±0.03	2.052×10^{-4}	1.942×10^{-4}	1.812×10^{-4}	1.852×10^{-4}
3.21±0.03	5.236×10^{-4}	4.829×10^{-4}	4.586×10^{-4}	4.664×10^{-4}
3.46±0.03	9.501×10^{-4}	8.882×10^{-4}	8.460×10^{-4}	8.534×10^{-4}
3.46±0.03	1.056×10^{-3}	1.027×10^{-3}	9.948×10^{-4}	9.992×10^{-4}
3.48±0.03	1.170×10^{-3}	1.134×10^{-3}	1.100×10^{-3}	1.100×10^{-3}
3.71±0.03	2.151×10^{-3}	2.023×10^{-3}	1.934×10^{-3}	1.944×10^{-3}
3.93±0.03	4.056×10^{-3}	3.822×10^{-3}	3.640×10^{-3}	3.675×10^{-3}
3.97±0.03	4.120×10^{-3}	3.959×10^{-3}	3.749×10^{-3}	3.852×10^{-3}
4.21±0.03	7.100×10^{-3}	6.704×10^{-3}	6.382×10^{-3}	6.453×10^{-3}
4.41±0.03	9.175×10^{-3}	8.792×10^{-3}	8.352×10^{-3}	8.533×10^{-3}
4.48±0.03	2.308×10^{-2}	2.189×10^{-2}	2.080×10^{-2}	2.105×10^{-2}
4.94±0.03	2.385×10^{-2}	2.109×10^{-2}	2.026×10^{-2}	1.998×10^{-2}
4.96±0.03	2.306×10^{-2}	2.228×10^{-2}	2.132×10^{-2}	2.163×10^{-2}

Table 5.5: Weighted "mixed" cross sections and S factors for the ^{104}Pd(p, γ) and ^{105}Pd(p, n) measurements. $\Delta\sigma$ is the sum of the statistical and systematic error. Δ S factor is the respective error from the S factor.

E_p^{eff}(c.m.)	weighted σ^+	Δ σ^+	S factor	Δ S factor
[MeV]	[barn]	[barn]	[MeV barn]	[MeV barn]
2.71±0.03	7.262×10^{-5}	5.264×10^{-6}	1.646×10^{8}	1.193×10^{7}
2.96±0.03	1.848×10^{-4}	1.319×10^{-5}	1.418×10^{8}	1.012×10^{7}
3.21±0.03	4.665×10^{-4}	3.249×10^{-5}	1.382×10^{8}	9.620×10^{6}
3.46±0.03	1.004×10^{-3}	7.165×10^{-5}	1.281×10^{8}	9.142×10^{6}
3.72±0.03	1.960×10^{-3}	1.402×10^{-4}	1.140×10^{8}	8.154×10^{6}
3.93±0.03	3.692×10^{-3}	2.438×10^{-4}	1.177×10^{8}	7.772×10^{6}
3.97±0.03	3.815×10^{-3}	2.727×10^{-4}	1.095×10^{8}	7.828×10^{6}
4.41±0.03	8.489×10^{-3}	6.040×10^{-4}	8.514×10^{7}	6.058×10^{6}
4.96±0.03	2.161×10^{-2}	1.602×10^{-3}	7.175×10^{7}	5.317×10^{6}

Table 5.6: Disentangled cross section σ^+ and S factor for the ^{104}Pd(p,γ) measurements. $\Delta\sigma$ is the sum of the statistical and systematic error. $\Delta\ S$ factor is the respective error from the S factor.

E$_p^{eff}$(c.m.)	weighted σ	$\Delta\ \sigma$	S factor	$\Delta\ S$ factor
[MeV]	[barn]	[barn]	[MeV barn]	[MeV barn]
2.71±0.03	7.716×10^{-5}	5.593×10^{-6}	1.766×10^{8}	5.730×10^{6}
2.96±0.03	1.823×10^{-4}	1.301×10^{-5}	1.413×10^{8}	4.530×10^{6}
3.21±0.03	4.441×10^{-4}	3.093×10^{-5}	1.334×10^{8}	4.030×10^{6}
3.46±0.03	9.352×10^{-4}	6.672×10^{-5}	1.179×10^{8}	8.410×10^{6}
3.72±0.03	1.882×10^{-3}	1.346×10^{-4}	1.104×10^{8}	3.620×10^{6}
3.93±0.03	3.194×10^{-3}	2.109×10^{-4}	1.031×10^{8}	2.810×10^{6}
3.97±0.03	3.301×10^{-3}	2.359×10^{-4}	9.366×10^{7}	6.690×10^{6}
4.41±0.03	6.837×10^{-3}	4.865×10^{-4}	6.782×10^{7}	4.830×10^{6}
4.96±0.03	1.541×10^{-2}	1.142×10^{-3}	5.063×10^{7}	3.750×10^{6}

Table 5.7: Weighted cross sections and S factors for the ^{105}Pd(p,n) measurements. $\Delta\sigma$ is the sum of the statistical and systematic error. $\Delta\ S$ factor is the respective error from the S factor.

E$_p^{eff}$(c.m.)	weighted σ	$\Delta\ \sigma$	S factor	$\Delta\ S$ factor
[MeV]	[barn]	[barn]	[MeV barn]	[MeV barn]
2.71±0.03	7.036×10^{-5}	5.100×10^{-6}	1.612×10^{8}	5.231×10^{6}
2.96±0.03	1.861×10^{-4}	1.328×10^{-5}	1.443×10^{8}	4.627×10^{6}
3.21±0.03	4.777×10^{-4}	3.336×10^{-5}	1.437×10^{8}	4.337×10^{6}
3.46±0.03	1.039×10^{-3}	7.410×10^{-5}	1.311×10^{8}	9.348×10^{6}
3.72±0.03	1.999×10^{-3}	1.430×10^{-4}	1.173×10^{8}	3.848×10^{6}
3.93±0.03	3.940×10^{-3}	2.602×10^{-4}	1.274×10^{8}	3.466×10^{6}
3.97±0.03	4.194×10^{-3}	2.997×10^{-4}	1.157×10^{8}	8.265×10^{6}
4.41±0.03	9.313×10^{-3}	6.627×10^{-4}	9.247×10^{7}	6.580×10^{6}
4.96±0.03	2.471×10^{-2}	1.831×10^{-3}	8.127×10^{7}	6.022×10^{6}

5.3 ^{105}Pd$(p,\gamma)^{106}$Ag^m and ^{106}Pd$(p,n)^{106}$Ag^m

The situation is more complicated for ^{105}Pd(p,γ) and ^{106}Pd(p,n) since the ground state in ^{106}Ag has a short half-life of 23.96 min. Here we could determine only the partial cross sections to the 8.28 d isomeric state. This 6^+ state decays 100% by EC to ^{106}Pd, which can be followed via the transitions at 451, 717, 748, and 1046 keV. Since we used natural samples, again we cannot distinguish between ^{105}Pd(p,γ) re-action and ^{106}Pd(p,n) channel which opens at E$_p \approx 3.7$ MeV. Analogously to Sec. 5.2 we thus can only measure an partial "mixed" cross section

$$\sigma^+ = \frac{22.33\% * \sigma_{pg} + 27.33\% * \sigma_{pn}}{49.66\%} \tag{5.8}$$

(Table 5.9) but in this case we cannot separate both reaction channels because no NON-SMOKER prediction for ^{106}Pd$(p,n)^{106}$Ag^m is available. This separation has to be postponed until the measurement with enriched ^{104,105}Pd samples is performed. Nevertheless the cross sections σ^+ at E$_p$=3.21 and 3.46 MeV can be considered as "pure" partial $\sigma(^{105}$Pd$(p,\gamma))$ cross section because they are far below the ^{106}Pd(p,n) threshold. Also the data point at 3.72 MeV has still a rather large contribution from the (p,γ) channel, as can be seen from the curve of the partial S factor in Fig. 5.6.

For the partial ^{106}Pd(p,n) cross section experimental data is available from Batij et al. [83] between E$_p$=5.5 and 9 MeV. Bitao et al. [84] calculated for this energy range the ratio between isomer and ground state (see Fig. 5.5) which agrees very well with the experiment of Batij et al. [83]. Table 5.8 lists this ratio $X = \frac{m}{g}$ from Bitao et al. together with the isomeric ratio $IR = \frac{m}{m+g}$ prediction for ^{105}Pd(p,γ) from NON-SMOKER.

Table 5.8: Top: Isomeric ratio for ^{105}Pd$(p,\gamma)^{106}$Ag^m derived from NON-SMOKER. Bottom: Ratios for ^{106}Pd$(p,n)^{106}$Ag^{mg} from Bitao et al. [84].

^{105}**Pd**(p,γ)			NON-SMOKER				
E$_p$ [MeV]	1.00	2.00	2.50	3.00	3.50	8.00	10.00
Isomeric ratio $\frac{m}{m+g}$	0.45	0.45	0.43	0.46	0.46	0.46	0.47
^{106}**Pd**(p,n)			Bitao et al. [84]				
E$_p$ [MeV]	5.49	5.98	6.49	7.01	7.5	7.99	9.008
Ratio X=$\frac{m}{g}$	0.034	0.045	0.061	0.08	0.107	0.141	0.252
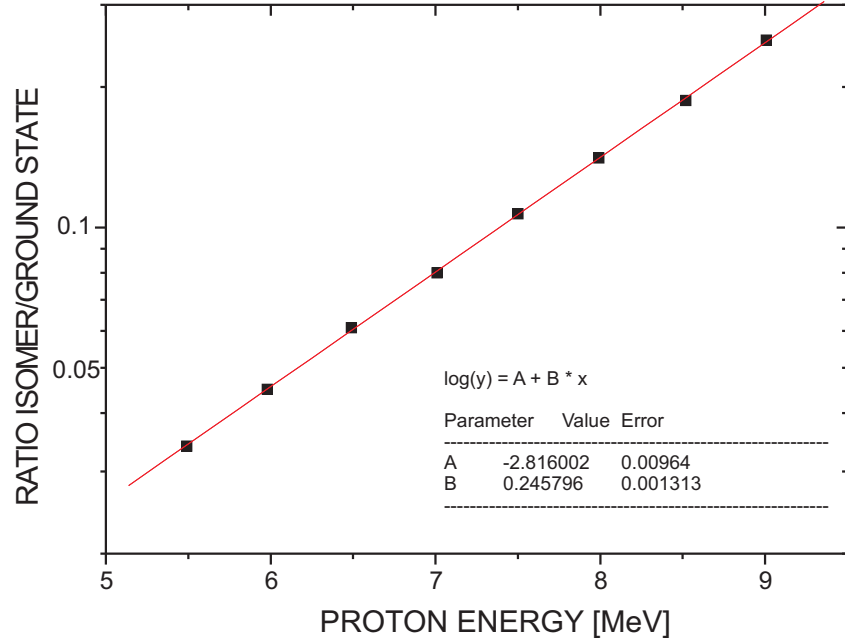
Figure 5.5: Fit of the ratio X for ^{106}Pd$(p,n)^{106}$Ag^{mg} from Bitao et al. [84].

Table 5.9: "Mixed" partial cross sections σ^+ from the ^{105}Pd(p,γ) and ^{106}Pd(p,n) measurement. The summing correction factor S_C for the FZK detector is shown below the column heads.

E_p(c.m.) [MeV]	σ^+(451 keV) [barn]	σ^+(717 keV) [barn]	σ^+(748 keV) [barn]	σ^+(1046 keV) [barn]
S_C	1.009	1.000	1.013	1.009
3.22	3.743×10^{-6}	3.489×10^{-6}	3.844×10^{-6}	3.507×10^{-6}
3.47	4.303×10^{-6}	4.398×10^{-6}	5.026×10^{-6}	4.765×10^{-6}
3.47	5.551×10^{-6}	5.623×10^{-6}	5.525×10^{-6}	5.073×10^{-6}
3.49	5.678×10^{-6}	6.414×10^{-6}	7.404×10^{-6}	5.846×10^{-6}
3.72	9.939×10^{-6}	9.905×10^{-6}	1.108×10^{-5}	1.032×10^{-5}
3.94	1.436×10^{-5}	1.638×10^{-5}	1.524×10^{-5}	1.392×10^{-5}
3.98	1.456×10^{-5}	1.637×10^{-5}	1.415×10^{-5}	1.486×10^{-5}
4.22	4.439×10^{-5}	4.570×10^{-5}	4.512×10^{-5}	4.235×10^{-5}
4.42	6.366×10^{-5}	6.517×10^{-5}	7.469×10^{-5}	5.77×10^{-5}
4.49	7.856×10^{-5}	7.944×10^{-5}	7.920×10^{-5}	7.757×10^{-5}
4.95	2.964×10^{-4}	3.143×10^{-4}	2.839×10^{-4}	2.985×10^{-4}
4.97	3.053×10^{-4}	3.193×10^{-4}	3.092×10^{-4}	2.959×10^{-4}
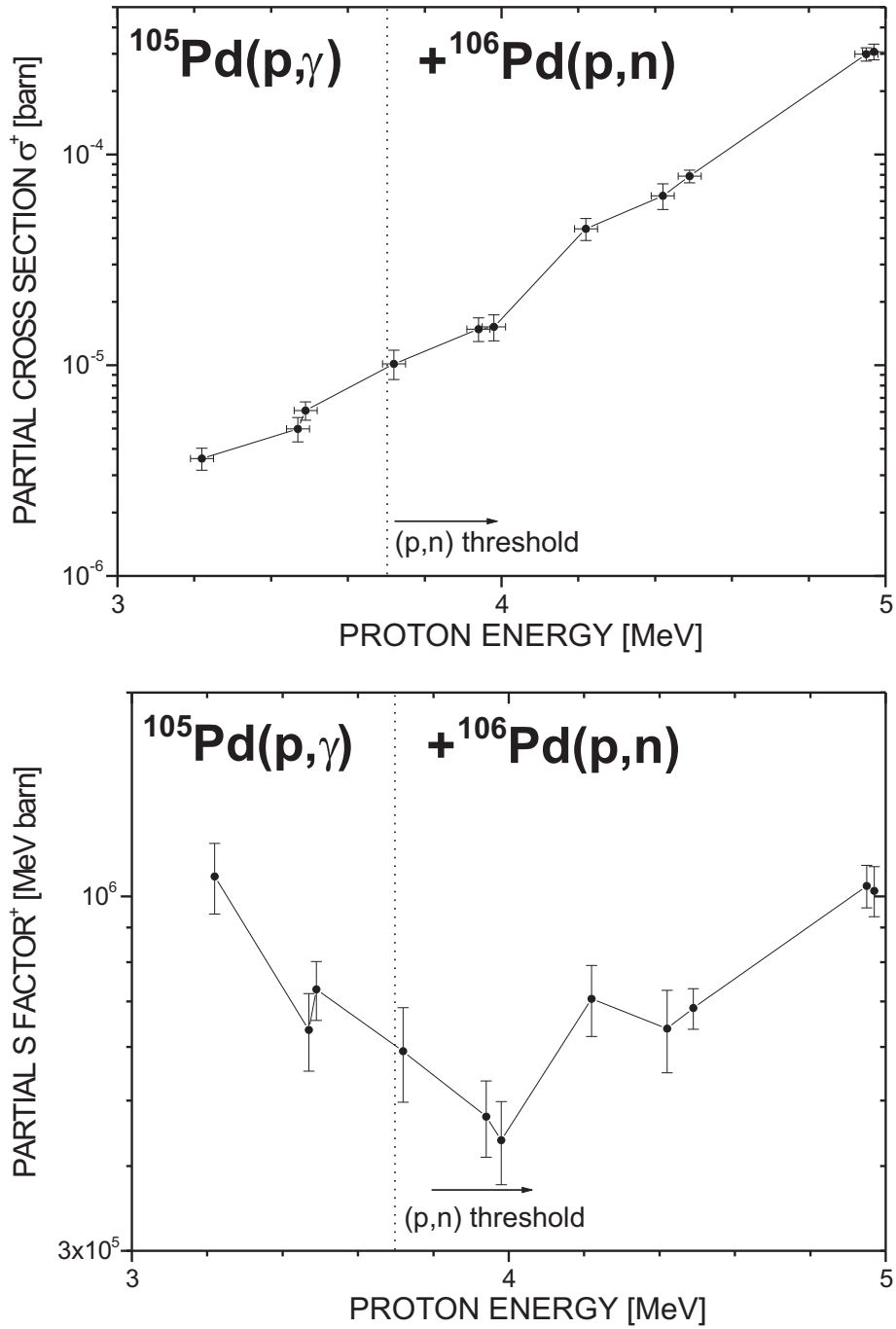
Figure 5.6: Partial "mixed" cross sections and S factors for ^{105}Pd$(p, \gamma)^{106}$Ag^m and ^{106}Pd$(p, n)^{106}$Ag^m.

Table 5.10: Weighted partial "mixed" cross sections and S factors for the ^{105}Pd(p, γ) and ^{106}Pd(p, n) measurements. $\Delta\sigma$ is the sum of the statistical and systematic error. ΔS factor is the respective error from the S factor.

E_p^{eff}(c.m.) [MeV]	weighted σ^+ [barn]	$\Delta \sigma^+$ [barn]	S factor [MeV barn]	ΔS factor [MeV barn]
3.21±0.03	3.605×10^{-6}	4.317×10^{-7}	1.070×10^6	1.281×10^5
3.46±0.03	4.983×10^{-6}	6.543×10^{-7}	6.356×10^5	8.345×10^4
3.48±0.03	6.091×10^{-6}	6.074×10^{-7}	7.291×10^5	7.270×10^4
3.71±0.03	1.015×10^{-5}	1.616×10^{-6}	5.910×10^5	9.405×10^4
3.93±0.03	1.484×10^{-5}	1.913×10^{-6}	4.734×10^5	6.104×10^4
3.97±0.03	1.519×10^{-5}	2.128×10^{-6}	4.368×10^5	6.121×10^4
4.21±0.03	4.434×10^{-5}	5.333×10^{-6}	7.064×10^5	8.497×10^4
4.41±0.03	6.364×10^{-5}	8.844×10^{-6}	6.382×10^5	8.868×10^4
4.48±0.03	7.872×10^{-5}	5.413×10^{-6}	6.843×10^5	4.706×10^4
4.94±0.03	2.988×10^{-4}	2.166×10^{-5}	1.037×10^6	7.515×10^4
4.96±0.03	3.071×10^{-4}	2.600×10^{-5}	1.020×10^6	8.634×10^4

5.4 ^{110}Pd$(p, n)^{110}$Ag^m

Only the partial (p, n) cross section of ^{110}Pd into the isomeric state in ^{110}Ag^m could be measured instead of the respective total ^{110}Pd(p, γ) cross section which was 1000 times lower. The γ-lines at 657.8, 763.9, 884.7 and 937.5 keV were used for analysis. The results are summarized in Table 5.11 with the respective summing correction factors S.

Fig. 5.7 shows a rather good agreement (within a factor of 1.2-1.3) with the measurement of Batij et al. [83] between 6 and 9 MeV. Since no partial cross section for the ^{110}Pd(p, n) reaction is available from NON-SMOKER, only the total cross section is shown there for a comparison of the energy trends. However, the total cross section measurement of Batij et al. [83] also shows a good agreement with the respective NON-SMOKER prediction, like the 46 years old measurement from Johnson et al. [85].

Table 5.11: Partial cross sections of the ^{110}Pd$(p, n)^{110}$Ag^m measurements derived from the single γ transitions. The summing correction factor S_C for the FZK detector is shown below the column heads.

| E_p(c.m.) [MeV]	σ(658 keV) [barn]	σ(764 keV) [barn]	σ(885 keV) [barn]	σ(938 keV) [barn]
S_C	1.008	1.010	1.010	1.000
3.47	5.446×10^{-5}		6.477×10^{-5}	
3.47	4.990×10^{-5}		5.280×10^{-5}	5.552×10^{-5}
3.49	6.217×10^{-5}		7.463×10^{-5}	
3.73	1.265×10^{-4}		1.350×10^{-4}	1.366×10^{-4}
3.94	2.844×10^{-4}		2.795×10^{-4}	2.847×10^{-4}
3.98	2.883×10^{-4}	2.916×10^{-4}	2.986×10^{-4}	
4.22	5.625×10^{-4}		5.654×10^{-4}	5.591×10^{-4}
4.42	7.988×10^{-4}	8.422×10^{-4}	8.405×10^{-4}	
4.49	1.013×10^{-3}		1.021×10^{-3}	1.012×10^{-3}
4.95	2.295×10^{-3}	2.386×10^{-3}	2.417×10^{-3}	
4.97	2.245×10^{-3}	2.377×10^{-3}	2.249×10^{-3}	
4.97	2.427×10^{-3}		2.473×10^{-3}	2.531×10^{-3}
5.87	8.327×10^{-3}	8.604×10^{-3}	8.002×10^{-3}	
6.93	2.634×10^{-2}	2.650×10^{-2}	2.631×10^{-2}	
7.98	4.825×10^{-2}	4.930×10^{-2}	4.861×10^{-2}	
8.91	7.414×10^{-2}	7.698×10^{-2}	7.581×10^{-2}	
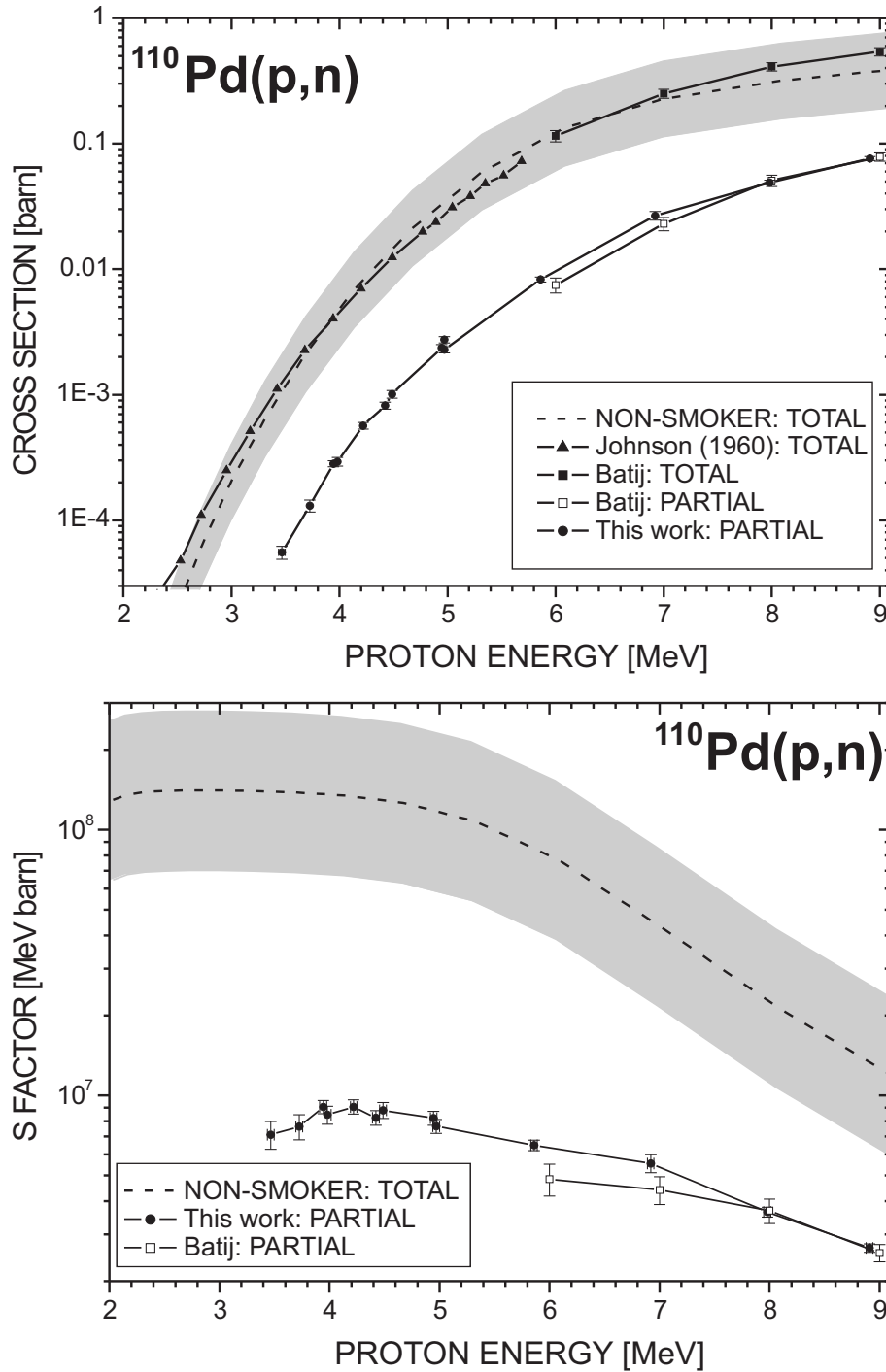
Figure 5.7: Partial cross section and S factor for $^{110}\text{Pd}(p,n)^{110}\text{Ag}^m$.

Table 5.12: Weighted partial cross sections and partial S factors from the ^{110}Pd(p,n) measurements. $\Delta\sigma$ is the sum of the statistical and systematic error. Δ S factor is the respective error from the S factor.

E_p^{eff}(c.m.) [MeV]	weighted σ [barn]	$\Delta\ \sigma$ [barn]	S factor [MeV barn]	$\Delta\ S$ factor [MeV barn]
3.45±0.03	$5.550{\times}10^{-5}$	$6.640{\times}10^{-6}$	$7.033{\times}10^{6}$	$8.420{\times}10^{5}$
3.71±0.03	$1.310{\times}10^{-4}$	$1.400{\times}10^{-5}$	$7.544{\times}10^{6}$	$8.110{\times}10^{5}$
3.93±0.03	$2.820{\times}10^{-4}$	$1.610{\times}10^{-5}$	$8.950{\times}10^{6}$	$5.120{\times}10^{5}$
3.97±0.03	$2.930{\times}10^{-4}$	$2.310{\times}10^{-5}$	$8.357{\times}10^{6}$	$6.590{\times}10^{5}$
4.21±0.03	$5.660{\times}10^{-4}$	$3.490{\times}10^{-5}$	$8.964{\times}10^{6}$	$5.520{\times}10^{5}$
4.41±0.03	$8.190{\times}10^{-4}$	$5.190{\times}10^{-5}$	$8.164{\times}10^{6}$	$5.180{\times}10^{5}$
4.48±0.03	$1.010{\times}10^{-3}$	$6.890{\times}10^{-5}$	$8.705{\times}10^{6}$	$5.950{\times}10^{5}$
4.94±0.03	$2.360{\times}10^{-3}$	$1.420{\times}10^{-4}$	$8.131{\times}10^{6}$	$4.900{\times}10^{5}$
4.96±0.03	$2.288{\times}10^{-3}$	$1.357{\times}10^{-4}$	$7.655{\times}10^{6}$	$4.541{\times}10^{5}$
5.86±0.03	$8.291{\times}10^{-3}$	$3.819{\times}10^{-4}$	$6.493{\times}10^{6}$	$2.991{\times}10^{5}$
6.92±0.03	$2.666{\times}10^{-2}$	$2.086{\times}10^{-3}$	$5.548{\times}10^{6}$	$4.341{\times}10^{5}$
7.97±0.03	$4.913{\times}10^{-2}$	$2.086{\times}10^{-3}$	$3.641{\times}10^{6}$	$1.546{\times}10^{5}$
8.90±0.03	$7.624{\times}10^{-2}$	$2.704{\times}10^{-3}$	$2.665{\times}10^{6}$	$9.452{\times}10^{5}$

5.5 Conclusion

Our experimental results agree in all cases within a factor of 2 with the respective NON-SMOKER cross sections. However, since we used natural samples we could not disentangle the reaction channels for ^{104}Pd$(p,\gamma)/^{105}$Pd(p,n) and ^{105}Pd$(p,\gamma)/$ ^{106}Pd(p,n). Thus, a measurement with enriched samples of ^{104}Pd and ^{105}Pd is necessary for a verification of these cross sections. Comparison with recent measurements performed at DEMOKRITOS in Greece will be interesting. Other results from these measurements will be more or less complementary, since they measure the prompt γ-rays online, whereas with our activation method we only can determine the γ-ray activity offline.

Chapter 6

The Karlsruhe Astrophysical Database of Nucleosynthesis in Stars

6.1 History of stellar neutron capture compilations

The first collection of stellar neutron capture cross sections was published in 1971 by Allen and co-workers [78]. This paper reviewed the role of neutron capture reactions in the nucleosynthesis of heavy elements and presented also a list of recommended (experimental or semi-empirical) Maxwellian averaged cross sections at $kT = 30$ keV (MACS30) for nuclei between carbon and plutonium.

The idea of an experimental and theoretical stellar neutron cross section database was picked up again by Bao and Käppeler [86] for s-process studies. This compilation published in 1987 included cross sections for (n,γ) reactions (between ^{12}C and ^{209}Bi), some (n,p) and (n,α) reactions (for ^{33}Se to ^{59}Ni), and also (n,γ) and (n,f) reactions for long-lived actinides. A follow-up compilation was published by Beer, Voss and Winters in 1992 [87].

In the year 2000 the update of this compilation [26] was extended to big bang nucleosynthesis. It included a collection of recommended MACS30 for isotopes between ^{1}H and ^{209}Bi, and – like the original Allen paper – also semi-empirical recommended values for nuclides without experimental cross section information. These estimated values are normalized cross sections derived with the Hauser-Feshbach code NON-SMOKER [21], which account for known systematic deficiencies in the nuclear input of the calculation. Additionally, the database provided stellar enhancement factors and energy-dependent MACS for energies between $kT = 5$ keV and 100 keV. The stellar enhancement factors and partially also the energy-dependence of the Maxwellian averaged cross sections were derived from theory (NON-SMOKER).

6.2 The Karlsruhe Astrophysical Database of Nucleosynthesis in Stars

As for any compilation, also Bao et al. needs regular updates. The increasing amount of neutron capture data, originating mainly from time-of-flight measurements with the 4π BaF_2 detectors at Karlsruhe and CERN/n_TOF, as well as from activation measurements, called for a database which can be easily updated. Additionally, a similar database project was started for the p process, since most of these measurements were performed within the last 10 years. With the increasing importance of the World Wide Web it became obvious that such a database could be implemented on the internet.

The "Karlsruhe Astrophysical Database of Nucleosynthesis in Stars" (KADoNiS) [88] was first launched under http://nuclear-astrophysics.fzk.de/kadonis in April 2005 with an online version of the previous Bao et al. compilation. On January 31st 2006, the first updated version of KADoNiS ("KADoNiS 0.1") was brought online. In the "Logbook" the updates can be followed. A second update was done in December 2006 ("KADoNiS 0.2"). The published paper version ("KADoNiS 1.0") is planned for 2008.

A still open project which has to be finished before the planned publication is the recalculation of cross sections for isotopes where a recent change in physical properties (e.g. $t_{1/2}$, I_γ...) will lead to changes in already measured cross sections.

6.2.1 Part 1: Updated big bang and s-process database

Included in the first update (KADoNiS v0.1) were only cross sections which were already published. Semi-empirical estimates were directly replaced by new experimental data and previous recommended cross sections were updated by inclusion of the new measurements. The most recent theoretical results derived with the Hauser-Feshbach code MOST [25] were added in November 2005. A version history is given in the Logbook.

Table 6.1 lists the respective semi-empirical cross sections which were replaced in KADoNiS v0.1 and v0.2 by experimental values. The updated cross sections by inclusion of new measurements are shown in Table 6.2.

The KADoNiS homepage provides a datasheet with all necessary information for each isotope similar to the layout in Ref. [26]. On the top of this page the recommended MACS30 for the total and partial cross sections are shown. In the "Comment" line one can find the previous recommended values, special comments, and the date of the last review. The field "List of all available values" includes the original values as given in the respective publications, renormalized values, year of publication, type of value (theoretical, semi-empirical, or experimental), a short comment about the method (accelerator, neutron, and reference source), and the references with hyperlinks.

This section is followed by tabulated MACS, reaction rates, and stellar enhancement factors for energies between $kT=$ 5 and 100 keV. A "click" on the field "Show/hide

Table 6.1: List of recommended semi-empirical cross sections, which were replaced by experimental values in KADoNiS v0.1 and v0.2.

Isotope	KADoNiS version	Old recomm. value [mbarn]	New recomm. value [mbarn]	Reference
^{74}Se	v0.1	267 ± 25	271 ± 15	[77], this work
^{78}Se	v0.2	109 ± 41	60.1 ± 9.6	[89]
^{84}Sr	v0.1	368 ± 125	300 ± 17	[77], this work
^{102}Pd	v0.2	375 ± 118	370 ± 14	this work
^{120}Te	v0.2	420 ± 103	499 ± 24	this work
^{128}Xe	v0.1	248 ± 66	262.5 ± 3.7	[90]
^{129}Xe	v0.1	472 ± 71	617 ± 12	[90]
^{130}Xe	v0.1	141 ± 51	132.0 ± 2.1	[90]
^{132}Ba	v0.2	379 ± 137	399 ± 16	this work
^{147}Pm	v0.1	1290 ± 470	709 ± 100	[91]
^{151}Sm	v0.1	2710 ± 420	3031 ± 68	[92]
^{174}Hf	v0.2	956 ± 283	983 ± 46	[75], this work
^{182}Hf	v0.2	117 ± 41	141 ± 8	[75]
^{180}Ta^{m}	v0.1	1640 ± 260	1465 ± 100	[93]

mass chain" gives a graphical plot of all available recommended total MACS30 for the isotopic mass chain of the respective element. The bottom part of each datasheet shows a chart of nuclides which can be zoomed by selecting different sizes (S, M, L, or XL). By clicking on an isotope in this chart, one can easily jump to the respective datasheet (if available).

Table 6.2: List of previous and new recommended cross sections, which were updated by inclusion of new experimental values in KADoNiS v0.1 and v0.2. "Reference" lists the latest publication which was included.

Isotope	KADoNiS version	Old recomm. value [mbarn]	New recomm. value [mbarn]	Reference
^{19}F	v0.2	5.4 ± 1.1	3.20 ± 0.06	[94]
^{22}Ne	v0.1	0.059 ± 0.006	0.058 ± 0.004	[95]
^{28}Si	v0.1	2.9 ± 0.3	1.42 ± 0.13	[96]
^{29}Si	v0.1	7.9 ± 0.9	6.58 ± 0.66	[96]
^{30}Si	v0.1	6.5 ± 0.6	1.82 ± 0.33	[96]
^{35}Cl	v0.1	10.0 ± 0.3	9.68 ± 0.21	[97]
^{37}Cl	v0.1	2.15 ± 0.8	2.12 ± 0.07	[97]
^{40}Ar	v0.1	2.6 ± 0.2	2.6 ± 0.2	[95]
^{54}Fe	v0.1	27.6 ± 1.8	29.6 ± 1.3	[98]
^{88}Sr	v0.1	6.2 ± 0.3	6.13 ± 0.11	[99]
^{90}Zr	v0.2	21 ± 2	19.4 ± 1.3	[100]
^{91}Zr	v0.2	60 ± 8	58.2 ± 2.5	[100]
^{92}Zr	v0.2	33 ± 4	30.1 ± 1.7	[100]
^{96}Ru	v0.1	238 ± 60	207 ± 8	[82]
^{99}Tc	v0.1	781 ± 50	933 ± 47	[101]
^{102}Ru	v0.1	186 ± 11	151 ± 7	[82]
^{104}Ru	v0.1	161 ± 10	156 ± 5	[82]
^{110}Cd	v0.1	246 ± 10	237 ± 2	[102]
^{111}Cd	v0.1	1063 ± 125	754 ± 12	[102]
^{112}Cd	v0.1	235 ± 30	187.9 ± 1.7	[102]
^{113}Cd	v0.1	728 ± 80	667 ± 11	[102]
^{114}Cd	v0.1	127 ± 5	129.2 ± 1.3	[102]
^{116}Cd	v0.1	59 ± 2	74.8 ± 0.9	[102]
^{116}Sn	v0.1	91.4 ± 0.9	91.6 ± 0.6	[103]
^{120}Sn	v0.1	36.0 ± 0.5	36.2 ± 0.3	[103]
^{130}Ba	v0.1	760 ± 110	767 ± 30	this work
^{135}Cs	v0.1	198 ± 17	160 ± 10	[104]
^{139}La	v0.1	38.4 ± 2.7	31.6 ± 0.8	[105]
^{151}Sm	v0.2	3031 ± 68	3039 ± 62	[106]
^{175}Lu	v0.1	1146 ± 44	1219 ± 10	[107]
^{176}Lu	v0.1	1532 ± 69	1639 ± 14	[107]
^{176}Hf	v0.1	455 ± 20	626 ± 11	[76]
^{177}Hf	v0.1	1500 ± 100	1544 ± 12	[76]
^{178}Hf	v0.1	314 ± 10	319 ± 3	[76]
^{179}Hf	v0.1	956 ± 50	922 ± 8	[76]
^{180}Hf	v0.1	179 ± 5	157 ± 2	[76]
^{204}Pb	v0.2	89.5 ± 5.5	81.6 ± 2.3	[108]
^{207}Pb	v0.2	9.7 ± 1.3	9.9 ± 0.5	[109]

6.2.2 Part 2: Experimental *p*-process database

The second part of KADoNiS is an experimental *p*-process database. In its present state (October 2006) it lists all available (p, γ) and (α, γ) measurements within the Gamow window, which was estimated as in Ref. [1]. In future a more accurate determination of the exact position of each single Gamow window will follow by inclusion of experimental data. The lists for (p, n), (α, n), (α, p), and (n, α) reactions will be completed in 2007. The last step will be the inclusion of photodisintegration rates.

The list includes the publication year, the reference, and a hyperlink to the respective EXFOR file under http://www.jcprg.org/master /exfor/. For each isotope, a datasheet similar to that in the neutron capture database will be created. In this datasheet, the real Gamow window for $T_9 =$ 2-3 will be given together with different datasets. By choosing one dataset, the data of the respective file is shown. A plot of all datasets (cross section vs. energy) with the indication of the real Gamow window will also be included (see Fig. 6.1).

The *p*-process database and the (final) layout is still under construction. Among the many open projects for the future of this database are the (automated) calculation of inverse reactions, the comparison of these values with the respective capture measurements, the inclusion of theoretical Hauser-Feshbach predictions (MOST, NON-SMOKER), and of course the completion of the list for (p, n), (α, n), (α, p), and (n, α) reactions.

Table 6.3: List of (α, γ) measurements included in the present *p*-process database

Isotope	Reaction	E [MeV]	Reference
^{56}Fe	(α, γ)	3.90 - 6.50	[110]
^{58}Ni	(α, γ)	4.90 - 6.10	[111]
^{62}Ni	(α, γ)	5.10 - 8.60	[112]
^{64}Ni	(α, γ)	4.40 - 7.10	[112]
^{63}Cu	(α, γ)	5.90 - 8.70	[113]
^{70}Ge	(α, γ)	5.05 - 7.80	[114]
^{96}Ru	(α, γ)	7.03 - 10.56	[82]
^{106}Cd	(α, γ)	7.57- 12.06	[115]
^{112}Sn	(α, γ)	8.30 - 9.97	[61]
^{144}Sm	(α, γ)	10.50 - 13.40	[116]

6.2.3 New semi-empirical estimates

For the publication in a referred journal in 2007 we also plan to update the semi-empirical estimates. The new values will be adopted to the then available set of experimental cross sections. For this reason, the ^{138}La estimated in Table 4.5 is still preliminary, since it might change by inclusion of new measurements. These

Table 6.4: List of (p, γ) measurements included in the present p-process database

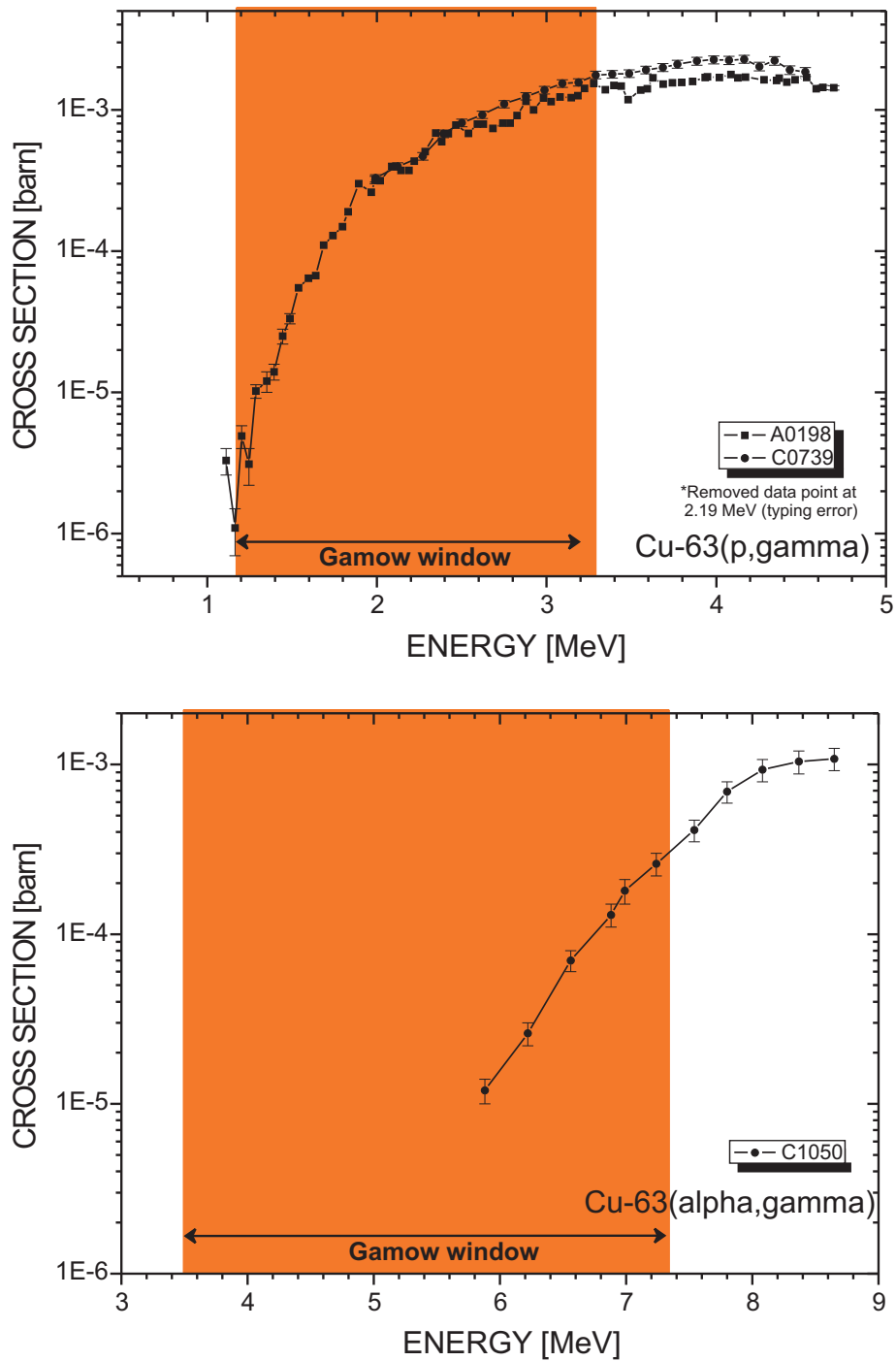| Isotope	Reaction	E [MeV]	Reference
^{58}Ni	(p, γ)	1.32 - 2.74	[117]
^{58}Ni	(p, γ)	1.00 - 4.91	[118]
^{58}Ni	(p, γ)	0.51 - 3.09	[119]
^{58}Ni	(p, γ)	1.14 - 4.09	[120]
^{60}Ni	(p, γ)	0.61 - 2.94	[119]
^{61}Ni	(p, γ)	1.11 - 2.94	[119]
^{64}Ni	(p, γ)	1.11 - 2.94	[121]
^{63}Cu	(p, γ)	1.11 - 4.69	[121]
^{63}Cu	(p, γ)	1.99 - 4.69	[122]
^{65}Cu	(p, γ)	1.03 - 3.22	[121]
^{65}Cu	(p, γ)	1.99 - 4.34	[122]
^{64}Zn	(p, γ)	1.47 - 2.73	[119]
^{67}Zn	(p, γ)	1.47 - 2.92	[119]
^{68}Zn	(p, γ)	1.67 - 4.97	[123]
^{74}Se	(p, γ)	1.60 - 3.00	[119]
^{74}Se	(p, γ)	1.46 - 3.55	[124]
^{76}Se	(p, γ)	1.46 - 3.55	[124]
^{77}Se	(p, γ)	1.55 - 2.97	[119]
^{84}Sr	(p, γ)	1.67 - 2.96	[125]
^{86}Sr	(p, γ)	1.48 - 2.96	[125]
^{87}Sr	(p, γ)	1.58 - 2.96	[125]
^{88}Sr	(p, γ)	1.38 - 4.94	[126]
^{89}Y	(p, γ)	1.76 - 4.83	[127]
^{90}Zr	(p, γ)	1.97 - 5.70	[128]
^{96}Zr	(p, γ)	3.50 - 6.00	[129]
^{93}Nb	(p, γ)	1.42 - 4.80	[130]
^{92}Mo	(p, γ)	1.48 - 3.00	[131]
^{94}Mo	(p, γ)	1.48 - 2.49	[131]
^{95}Mo	(p, γ)	1.70 - 3.00	[131]
^{98}Mo	(p, γ)	1.48 - 3.00	[131]
^{96}Ru	(p, γ)	1.65 - 3.37	[132]
^{98}Ru	(p, γ)	1.60 - 3.37	[132]
^{99}Ru	(p, γ)	1.46 - 3.37	[132]
^{100}Ru	$(p, \gamma)+(p, n)$	1.46 - 3.37	[132]
^{104}Ru	(p, γ)	1.46 - 3.37	[132]
^{102}Pd	(p, γ)	2.53 - 4.17	[61]
^{112}Sn	(p, γ)	3.00 - 8.50	[129]
^{116}Sn	(p, γ)	2.63 - 4.18	[61]
^{119}Sn	(p, γ)	2.80 - 6.00	[129]

Figure 6.1: Example of data plot for ^{63}Cu with approximate location of the Gamow window for $T=$ 2-3 GK as estimated in [1]. The label gives the respective EXFOR file number. Top: ^{63}Cu(p, γ) [121, 122]. Bottom: ^{63}Cu(α, γ) [113].

values will be, as in [26], normalized NON-SMOKER cross sections which account for known systematic deficiencies in the nuclear input of the calculation.

Chapter 7

Update of reaction libraries

7.1 General

The file "REACLIB.NOSMO" is a local version of a library of nuclear reactions between ^{1}H and Z=83 (bismuth). Most of these reaction rates are deduced from statistical Hauser-Feshbach calculations and only a few of them are experimental. The file is a limited update of a previous version from 1991 which was performed in 1995. Theoretical NON-SMOKER rates (here called RATH, [22]) up to Z=83 were inserted and replaced previous SMOKER values (from FKTH [133]). The masses (Q values) for isotopes without experimental information were taken from the Finite Range Droplet Model (FRDM) [134].

The reaction library consists of 8 different sections for different reactions. A detailed description of the REACLIB format can be found in the provided "readme" file under
http://download.nucastro.org/astro/reaclib. The present update affects only sections "2" (photodisintegrations) and "4" (capture reactions).

Each reaction rate is described by three lines. The first marks the type of reaction, the reference, the label "n" or "r" for non-resonant or resonant reactions, an (optional) letter "v", which indicates that the respective rate is calculated from the inverse reaction, and the Q value in MeV. The second and third line give seven parameters a$_0$, a$_1$, a$_2$, a$_3$, a$_4$, a$_5$, and a$_6$, from which the rate for each T_9 between 0.1 and 10 GK can be calculated via:

$$Rate = exp\,[a_0 + \frac{a_1}{T_9} + \frac{a_2}{T_9^{1/3}} + a_3 \cdot T_9^{1/3} + a_4 \cdot T_9 + a_5 \cdot T_9^{5/3} + a_6 \cdot ln(T_9)]. \quad (7.1)$$

"Rate" corresponds to $ln(2)/t_{1/2}$ for decays, N_A<ab> for two-body reactions and $N_A{}^2$<abc> for three-body reactions.

The stellar reaction rate $N_A < \sigma^*\upsilon >_{n,\gamma}$ is related to the respective inverse rate $N_A < \sigma^*\upsilon >_{\gamma,n}$ via detailed balance, see Eq. 2.8. For photodissociation reactions the respective relation is [22]:

$$\lambda_\gamma = \frac{(2J_i + 1)(2J_n + 1)}{2J_f + 1} \left(\frac{A_i}{A_f}\right)^{3/2} \frac{G_i(T)}{G_f(T)}\; exp\left(- \frac{Q_{n,\gamma}}{kT}\right)\, T_9^{3/2}\; F\; N_A < \sigma^*\upsilon >_{n,\gamma} (7.2)$$

The units are [s^{-1}] for λ_γ, [GK] for T$_9$, and [cm^3 s^{-1} mole^{-1}] for the reaction rate $N_A < \sigma^* \upsilon >$. The numerical factor F is

$$F = \frac{1}{N_A}\Big(\frac{u\ k}{2\pi\ \hbar^2}\Big)^{3/2} = 9.8685 \times 10^9\ [mole\ cm^{-3}]. \tag{7.3}$$

The respective parameters for the inverse rate are thus determined by keeping a$_2$, a$_3$, a$_4$, and a$_5$. a$_0$ has to be replaced with a$_0^{rev}$ which accounts for the numerical factor F (Eq. 7.2) and the spin and mass factors. a_1^{rev} is determined by a_1–11.6045·Q (the Q value). The factor 11.6045 is derived from 1 MeV = k·11.6045 GK. In case of calculating a photodissociation rate from a capture rate a$_6^{rev}$ is determined by a$_6$ + 1.5. This term is derived from $T_9^{3/2}$ in Eq. 7.2. For all other rates is a$_6^{rev}$= a$_6$. Thus, for the here discussed cases of calculating photodisintegration rates from capture rates, the seven-parameter fit becomes:

$$N_A < ab >_{\gamma,x}= exp\ [a_0^{rev} + \frac{a_1\ -\ 11.6045\cdot Q}{T_9} + \frac{a_2}{T_9^{1/3}} + a_3\cdot T_9^{1/3} + a_4\cdot T_9 +$$
$$+a_5\cdot T_9^{5/3} + (a_6\ +\ 1.5)\cdot ln(T_9)] \tag{7.4}$$

The value derived by this equation has finally to be multiplied by the ratio of the partition functions for target and product nucleus $\frac{G_t}{G_p}$. A detailed description and tabulated data can be found in [22].

7.2 Update process

For this thesis, only the neutron capture cross sections (and vice versa the inverse (γ, n) reactions) have been updated by inclusion of the experimental KADoNiS v0.2 cross sections and the semi-empirical estimates given there. The available version of REACLIB.NOSMO included (experimental) neutron capture rates from the Bao et al. compilation from 1987 [86], but only up to ^{81}Br. These rates were fitted with one parameter, a$_0$, whereas a$_1$ to a$_6$ were set to zero. In these cases, the neutron capture rates are described only as s wave captures which are temperature independent. Therefore, also all Bao 1987 entries (beyond ^{20}Ne, labelled with BAKA) were replaced again by temperature-dependent NON-SMOKER entries which are then renormalized. An exception was made for ^{22}Ne, where the old temperature dependence from [135] seems to fit a recent measurement from [95] better than the NON-SMOKER rate. Here the RATH entry was deleted and the previous (resonant and non-resonant) entries renormalized. For a graphical comparison of these three temperature dependences, see the discussion in Chapter 9.

In [7] a table with renormalization factors f^{old}=r$_{exp}$/r$_{theo}$ was published for the transformation of theoretical NON-SMOKER cross sections into experimental Maxwellian averaged cross sections at kT= 30 keV, $<\sigma >_{30}$, given in the Bao et al. compilation from 2000 [26]. This renormalization factor has to be multiplied with the rate derived via Eq. 7.1.

The same renormalization factor has to be included in the reverse rate and yields the updated parameter $a_0^{rev,new}$. First, the factor f^x is used to update the 12 low mass neutron capture reactions listed in Table 7.1, which do not originate from SMOKER or NON-SMOKER calculations. Since the statistical model is not applicable for isotopes with low level densities ($Z <10$), NON-SMOKER includes only reactions starting with the Ne isotopes.

The table with renormalization factors provided in [7] compared only the theoretical stellar cross sections with the respective experimental laboratory cross sections given in Bao et al. 2000, hence the stellar enhancement factor SEF is missing. For this reason, a new table with renormalization factors $f^*=r_{exp}/r_{theo}$ was produced (Table 7.2). These factors update the NON-SMOKER rates directly to the most recent KADoNiS rates of version v0.2.

Table 7.1: Renormalization factors f^x for the update of reactions on light isotopes (below ^{22}Ne) to the most recent KADoNiS version v0.2.

Isotope	f^x	$<\sigma>_{30}$(old) [mb]	$<\sigma>_{30}$(new) [mb]	References
p	1.191	0.213	0.254	[135], [26]
he3	319.780	2.38×10^{-5}	0.0076	[135], [26]
li7	1.034	0.0406	0.042	[135], [26]
c12	0.077	0.2001	0.0154	[86], [26]
c13	1.413	0.0149	0.021	[135], [26]
c14	0.828	0.0018	0.0015	[135], [26]
n14	0.603	0.0680	0.041	[135], [26]
n15	0.537	0.0108	0.0058	[135], [26]
o16	189.920	2.00×10^{-4}	0.038	[86], [26]
o18	0.400	0.0222	0.00886	[135], [26]
f19	0.592	5.4024	3.20	[86], [94]
ne22	0.700	0.0829	0.058	[135], [95]

^{180}Ta^m is not included in this list, since it is the only (stable) isotope, which exists only in the isomeric state. The reaction library entries for ^{180}Ta are only for the capture from the ground-state, and the respective entry for the isomeric state can be deduced from the footnote of Table 5 in [7]. These parameters are normalized to the previous recommended (semi-empirical) value of 1640 mb. Hence, for the actual recommended (experimental) value of 1465 mb, one has to include a factor of 0.855: a_0^{new}= -10.055368; a_1= 0.2659302; a_2= -27.6891; a_3= 59.43646; a_4= -3.639849; a_5= 0.03887359; a_6= -25.80838.

This procedure is a quick and easy way of updating reaction libraries for neutron captures by normalizing to experimental Maxwellian averaged cross sections at kT=30 keV. A more sophisticated and accurate method would be a re-fitting of the seven parameters with the experimental energy-dependences. One example

Table 7.2: Renormalization factors $f^* = r_{exp}/r_{theo}$. These factors normalize the theoretical rates from RATH [22] to the stellar Maxwellian averaged cross sections, MACS×SEF, of the most recent KADoNiS version v0.2. * The RATH entry from ^{22}Ne was removed and the old entry normalized with the factor f^x, see Table 7.1.

Isotope	f*	Isotope	f*	Isotope	f*	Isotope	f*	Isotope	f*
ne20	0.072	zn68	0.672	pd106	1.137	ce133	0.855	yb170	1.224
ne21	0.332	zn70	1.285	pd107	1.599	ce134	0.787	yb171	1.291
ne22*	0.129*	ga69	0.768	pd108	1.293	ce135	0.647	yb172	0.963
na23	0.697	ga71	1.318	pd110	1.395	ce136	0.500	yb173	0.881
mg24	0.965	ge70	0.820	ag107	0.908	ce137	0.684	yb174	0.928
mg25	0.777	ge72	1.272	ag109	1.003	ce138	0.614	yb175	1.108
mg26	0.075	ge73	1.230	ag110	0.866	ce139	0.611	yb176	1.053
al26	0.504	ge74	1.269	cd106	0.665	ce140	0.486	lu175	1.146
al27	0.630	ge76	1.442	cd108	0.536	ce141	0.597	lu176	1.107
si28	0.259	as75	1.891	cd110	0.784	ce142	0.744	hf174	1.375
si29	0.746	se74	1.309	cd111	0.936	pr141	0.424	hf176	1.317
si30	0.901	se76	1.380	cd112	0.842	pr142	0.595	hf177	1.326
p31	0.156	se77	1.354	cd113	1.129	pr143	0.781	hf178	0.977
s32	0.367	se78	0.815	cd114	0.910	nd142	0.424	hf179	0.947
s33	0.489	se79	1.182	cd115	0.674	nd143	0.525	hf180	0.901
s34	0.064	se80	1.097	cd116	0.832	nd144	0.715	hf181	1.107
s36	0.599	se82	0.482	in113	0.659	nd145	0.767	hf182	1.389
cl35	0.607	br79	1.422	in115	0.709	nd146	0.896	ta179	0.938
cl36	0.659	br81	1.170	sn112	0.543	nd147	1.426	ta181	0.870
cl37	0.978	kr78	0.916	sn114	0.490	nd148	1.630	ta182	0.939
ar36	0.615	kr79	1.189	sn115	0.648	nd150	1.536	w180	0.833
ar38	0.789	kr80	1.313	sn116	0.532	pm147	0.565	w182	0.752
ar39	0.900	kr81	1.099	sn117	0.749	pm148	1.529	w183	0.832
ar40	0.693	kr82	0.764	sn118	0.597	pm149	2.164	w184	0.954
k39	0.855	kr83	0.768	sn119	0.717	sm144	0.426	w185	1.255
k40	1.021	kr84	0.609	sn120	0.575	sm147	0.652	w186	1.238
k41	0.968	kr85	0.448	sn121	0.784	sm148	0.928	re185	1.435
ca40	0.544	kr86	0.418	sn122	0.556	sm149	1.495	re186	1.126
ca41	0.973	rb85	0.528	sn124	0.559	sm150	1.754	re187	1.448
ca42	0.932	rb86	0.428	sn125	1.046	sm151	1.954	os184	0.916
ca43	1.533	rb87	0.302	sn126	1.050	sm152	1.695	os186	0.705
ca44	1.186	sr84	0.753	sb121	0.737	sm153	1.419	os187	1.123
ca45	1.044	sr86	0.305	sb122	0.429	sm154	1.049	os188	1.155
ca46	1.694	sr87	0.277	sb123	0.552	eu151	1.511	os189	1.228
ca48	1.315	sr88	0.397	sb125	0.949	eu152	1.238	os190	1.374
sc45	1.164	sr89	0.406	te120	0.894	eu153	1.062	os191	1.636
ti46	0.770	y89	0.214	te122	0.870	eu154	1.092	os192	2.536
ti47	0.800	zr90	0.388	te123	1.117	eu155	0.998	ir191	1.360
ti48	2.083	zr91	0.375	te124	0.772	gd152	1.802	ir192	1.576
ti49	0.966	zr92	0.435	te125	1.041	gd153	1.610	ir193	1.406
ti50	1.122	zr93	0.501	te126	0.717	gd154	1.643	pt190	0.762
v50	0.974	zr94	0.392	te128	0.829	gd155	1.254	pt192	0.954
v51	1.959	zr95	0.624	te130	0.609	gd156	1.356	pt193	1.348
cr50	1.091	zr96	0.742	i127	0.854	gd157	1.092	pt194	1.120
cr51	1.015	nb93	0.611	i129	1.033	gd158	1.220	pt195	1.486
cr52	0.524	nb94	0.567	xe124	0.803	gd160	0.880	pt196	1.179
cr53	2.237	nb95	0.532	xe126	0.666	tb159	1.026	pt198	1.211
cr54	0.715	mo92	0.546	xe128	0.846	tb160	1.169	au197	1.114
mn55	1.120	mo94	0.674	xe129	1.056	dy156	1.404	au198	1.047
fe54	0.637	mo95	0.604	xe130	0.824	dy158	1.145	hg196	1.556
fe55	0.895	mo96	0.712	xe131	0.736	dy160	1.536	hg198	0.729
fe56	0.447	mo97	0.831	xe132	0.884	dy161	1.194	hg199	1.210
fe57	1.315	mo98	1.050	xe133	0.808	dy162	1.143	hg200	1.040
fe58	0.944	mo99	1.135	xe134	0.576	dy163	1.033	hg201	2.158
co59	0.740	mo100	1.762	xe136	0.612	dy164	1.211	hg202	1.533
ni58	0.811	tc99	1.360	cs133	0.737	ho163	1.018	hg203	1.267
ni59	0.940	ru96	0.732	cs134	0.695	ho165	1.026	hg204	2.796
ni60	0.902	ru98	0.660	cs135	0.557	er162	1.564	tl203	0.975
ni61	1.059	ru99	0.822	ba130	1.047	er164	1.342	tl204	1.268
ni62	0.650	ru100	0.965	ba132	0.845	er166	1.230	tl205	1.033
ni63	0.857	ru101	1.495	ba134	0.767	er167	1.011	pb204	1.226
ni64	0.858	ru102	1.025	ba135	0.918	er168	1.395	pb205	1.356
cu63	0.925	ru103	1.116	ba136	0.596	er169	1.458	pb206	0.588
cu65	0.731	ru104	1.546	ba137	0.647	er170	1.136	pb207	0.650
zn64	0.773	rh103	1.189	ba138	0.695	tm169	1.606	pb208	0.918
zn65	0.775	pd102	0.985	la138	0.541	tm170	1.389	bi209	0.334
zn66	0.735	pd104	0.955	la139	0.422	tm171	1.195	bi210	0.443
zn67	1.035	pd105	1.236	ce132	0.913	yb168	1.375		

where a refitting makes much more sense than a renormalization is e.g. ^{22}Ne, see Chapter 9.

7.3   Update of save_reaclib.wolf

The reaction library save_reaclib.wolf from the p-process simulation packet "pProSim" was updated in the same way and with the same factors as described before. Additionally, the entry for the neutron capture of ^{26}Al ("al26") was added to this library, since it contained only the neutron capture entry for ^{26}Al^g ("al-6" from SMOKER), whereas for the inverse channel both entries, one from NON-SMOKER for al26 and one from SMOKER for al-6, existed. This reaction library was used for the p-process simulation which is described in the following chapter. Table 7.3 gives an overview of the number of reactions in both reaction libraries.

Table 7.3:   Comparison of the reaction library files reaclib.nosmo and save_reaclib.wolf used in the p-process simulation.

		Number of reactions	
	Library section	reaclib.nosmo	save_reaclib.wolf
1	a → b	1075	1442
2	a → b+ c	15453	15532
3	a → b+ c+ d	254	263
4	a+ b → c	15055	15135
5	a+ b → c+ d	28163	30032
6	a+ b → c+ d+ e	21	60
7	a+ b → c+ d+ e+ f	6	6
8	a+ b+ c→ d (+e)	26	35
	Sum	60053	62505

Chapter 8

p-process network calculations

The p-process network calculations were carried out with the program "pProSim" [37, 38]. The underlying nuclear reaction library in the file save_reaclib.wolf was originally based on a reaction network from the Michigan State University for X-ray bursts. Since this network included only proton-rich isotopes between hydrogen and xenon, it was extended for p-process studies by inclusion of the file reaclib.nosmo. For this reason, the (n,γ) and (γ,n) reactions of both reaction libraries were updated with available experimental data in the same way (see Chapter 7).

The present network comprises more than 60000 reactions (Table 7.3), which connect 1814 nuclei between hydrogen and bismuth. pProSim simulates the abundance evolution (e.g. for the 32 p isotopes) with a parameterized model of a supernova type II explosion [6]. Since the p-process layers are located far outside the collapsing core, they only experience the bounced shock front passing through the O/Ne burning zone and the subsequent temperature and density increase.

8.1   Input parameters

For this thesis, the input parameters from [37, 38] were adopted. Unlike described there, the simulations in this thesis were <u>not</u> carried out by changing reaction rates artificially and collectively by a factor of 3 and 1/3. Since the update process replaced the 32 theoretical predictions for neutron capture cross sections of the stable p-process isotopes in previous reaction libraries with 26 experimental cross sections and 6 semi-empirical predictions (^{98}Ru, ^{138}La, ^{158}Dy, ^{168}Yb, ^{184}Os, and ^{196}Hg), only the influence of this change (and all other included experimental neutron capture cross sections) on the overproduction factors was investigated. In the following the input parameters are shortly described. For more details, refer to [37, 38] and the references therein.

8.1.1   Seed abundances

The final p-process abundances depend very sensitively on the choice of the initial seed abundance. This initial abundance depends on the in-situ modification of

the stellar material in various nucleosynthesis processes during the stellar evolution. This also means that the respective O/Ne layers can receive an abundance contribution from the weak s process in the mass region up to A=90. This s-process component depends on the mass of the star and also on the neutrons provided by the $^{22}Ne(\alpha, n)^{25}Mg$ neutron source.

In this simulations, the initial seed abundances for nuclei with A≥40 correspond to the s abundance distribution of a supernova progenitor star with 25 solar masses (25 $M_\odot$, see Fig. 8.1), as described in [6, 11]. Since the p-process layers during the explosion are within the convective zones, which originate from the previous helium burning phases of the progenitor star, the s-process abundance distribution in all layers can be assumed to be constant. The results of the simulation were compared with the solar abundances of the p nuclei from Anders and Grevesse [8], see Fig. 2.1.

8.1.2 Temperature and density profiles

The O/Ne burning zone in this simulation was subdivided in 14 single layers. Due to the strong dependence of the reaction rates on temperature the temperature and density profiles play a crucial role in this astrophysical network. These profiles as function of time were adopted from [136] (see Fig. 8.2). Refs. [37, 38] provide also tables with the mass shells and their respective peak temperatures and densities.

8.1.3 Mass fractions and overproduction factors

The production of the p isotope i is described by its mass $m_i(M)$ [6]:

$$m_i(M) = \sum_{n \geq 1} \frac{1}{2}(X_{i,n} + X_{i,n-1}) \cdot (M_n - M_{n-1}) \qquad (8.1)$$

The sum runs over all p-process layers n, where M_n is the mass coordinate containing a mass fraction $X_{i,n}$ of the p nuclei i. The mean overproduction factor $< F_i >$ for each p-process layer is defined with respect to the solar mass fraction $X_{i,\odot}$ by

$$< F_i > (M) = \frac{m_i(M)}{M_{p,tot} \cdot X_{i,\odot}}. \qquad (8.2)$$

The averaged overproduction factor F_0 is a measure of the overall enrichment of the 35 p nuclei (including ^{152}Gd, ^{164}Er, and $^{180}Ta^m$ with a large s-process contribution) in the total p-process mass $M_{p,tot}$:

$$F_0(M) = \sum_i \frac{< F_i > (M)}{35}. \qquad (8.3)$$

Thus $< F_i >$ would be equal to F_0 if the calculated p-process distribution corresponds to a perfect solar distribution. Accordingly, the normalized overabundances are defined as $\frac{<F_i>}{F_0}$. Ranges of variations of the normalized overabundances for SNII with 13≤ $M_\odot$ ≤25 are given in Fig. 4 in Ref. [6].
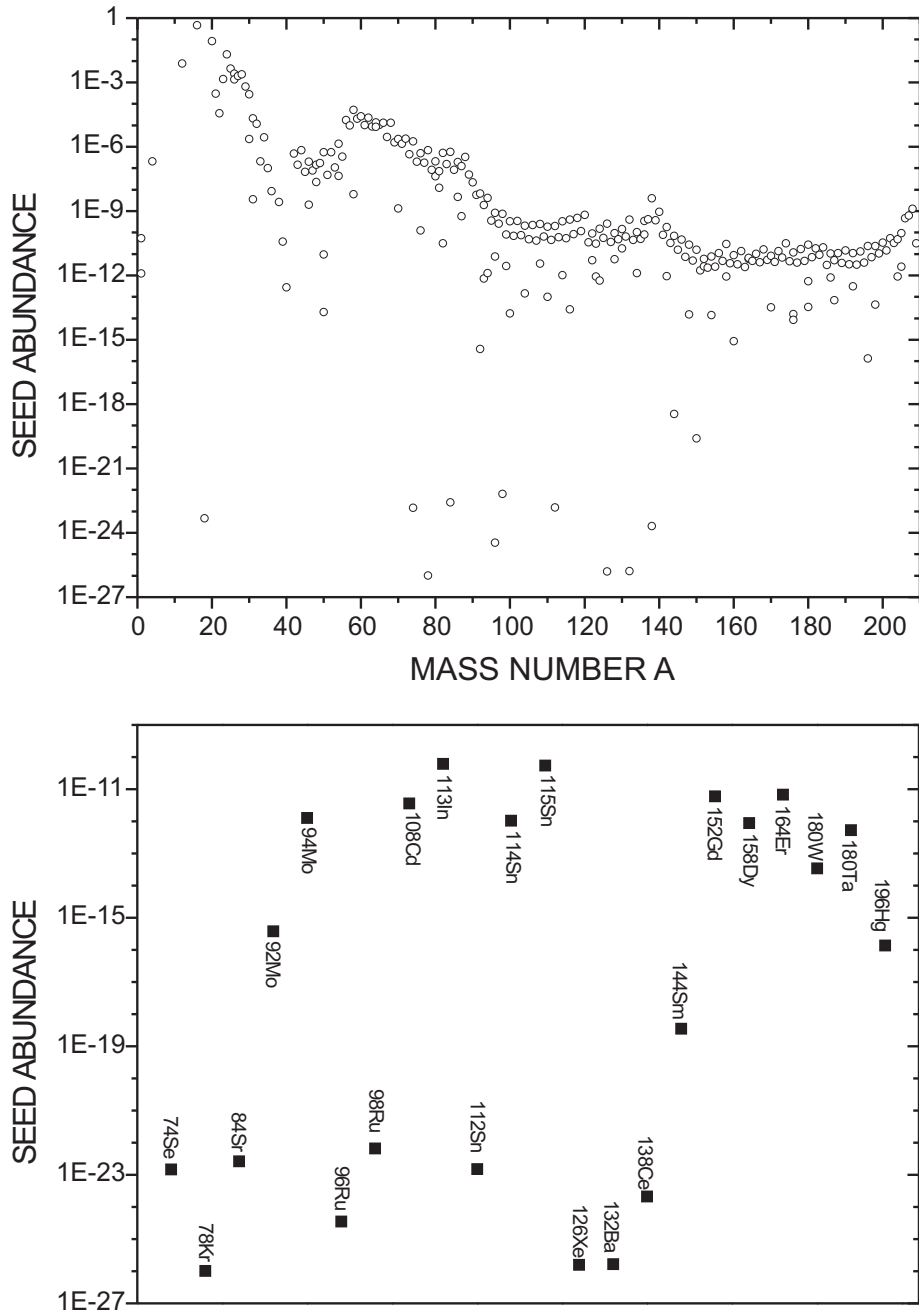
Figure 8.1: Initial seed abundances used in pProSim, corresponding to the s abundances in the supernova progenitor star of [6, 11]. Top: All isotopes. Bottom: Only p isotopes.
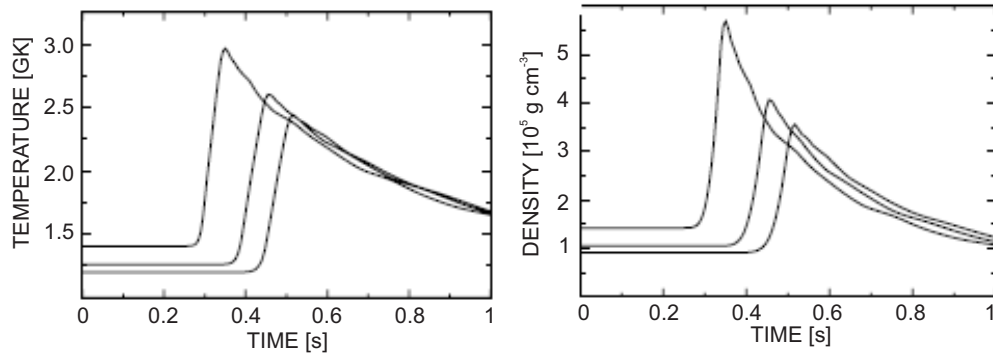
Figure 8.2: Temperature and density profiles for three p-process layers of the supernova shock front. Picture taken from [38].
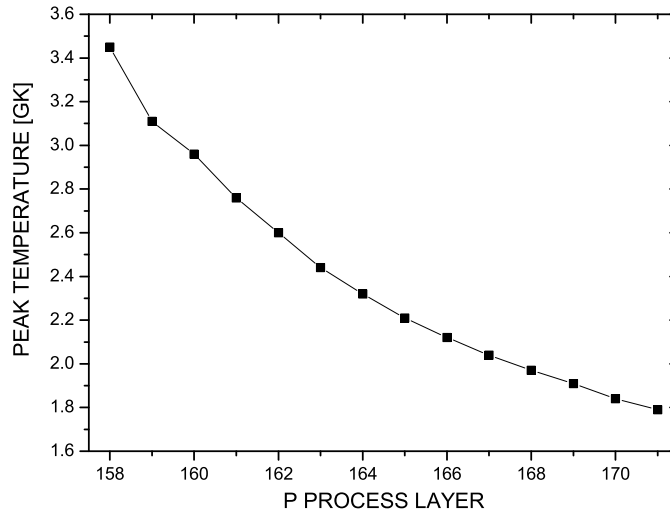

Figure 8.3: Peak temperatures of the single p-process layers used in these simulations.

8.2   Results

For this thesis p-process simulations with the previous and the updated reaction library were carried out and the influence of the implementation of experimental neutron capture rates (and also the derived new (γ, n) rates) is examined. The top part of Fig. 8.4 shows the influence of these changes on the normalized overproduction factor $<F_i>/F_0$ for the 35 p isotopes. As can be seen, no overproduction factor is changed significantly. The previous averaged overproduction factor was F_0=86.28, whereas with the updated reaction library this factor only decreases by less than 1% to F_0=85.78.

The influence for each p isotope becomes more visible in the bottom part of Fig. 8.4 where the ratios of the normalized overproduction factors (filled squares) and the respective Maxwellian averaged cross sections at $kT=$ 30 keV (open triangles) are shown. For $92\leq A \leq 144$ and $A>170$ the updated experimental cross sections of the p nuclei are predominantly smaller than the previous theoretical predictions from NON-SMOKER [22]. However, this change is not that strongly reflected in the ratio of the normalized overabundance factors which scatter around unity.

For the six p isotopes between mass $A=150\text{-}170$ (^{152}Gd, ^{156}Dy, ^{158}Dy, ^{162}Er, ^{164}Er, and ^{168}Yb) one observes an anti-correlated trend: the updated cross sections are larger than before, and the overproduction factors calculated with the updated reaction library are smaller. The overproduction factor $<F_i>$ versus peak temperature in each layer is given in Fig. 8.5. As can be seen, the largest difference arises from the layers with $T_{peak}=2.1\text{-}2.3$ GK (layers 165 and 166) where changes up to a factor of 60 are observed with the updated reaction library.
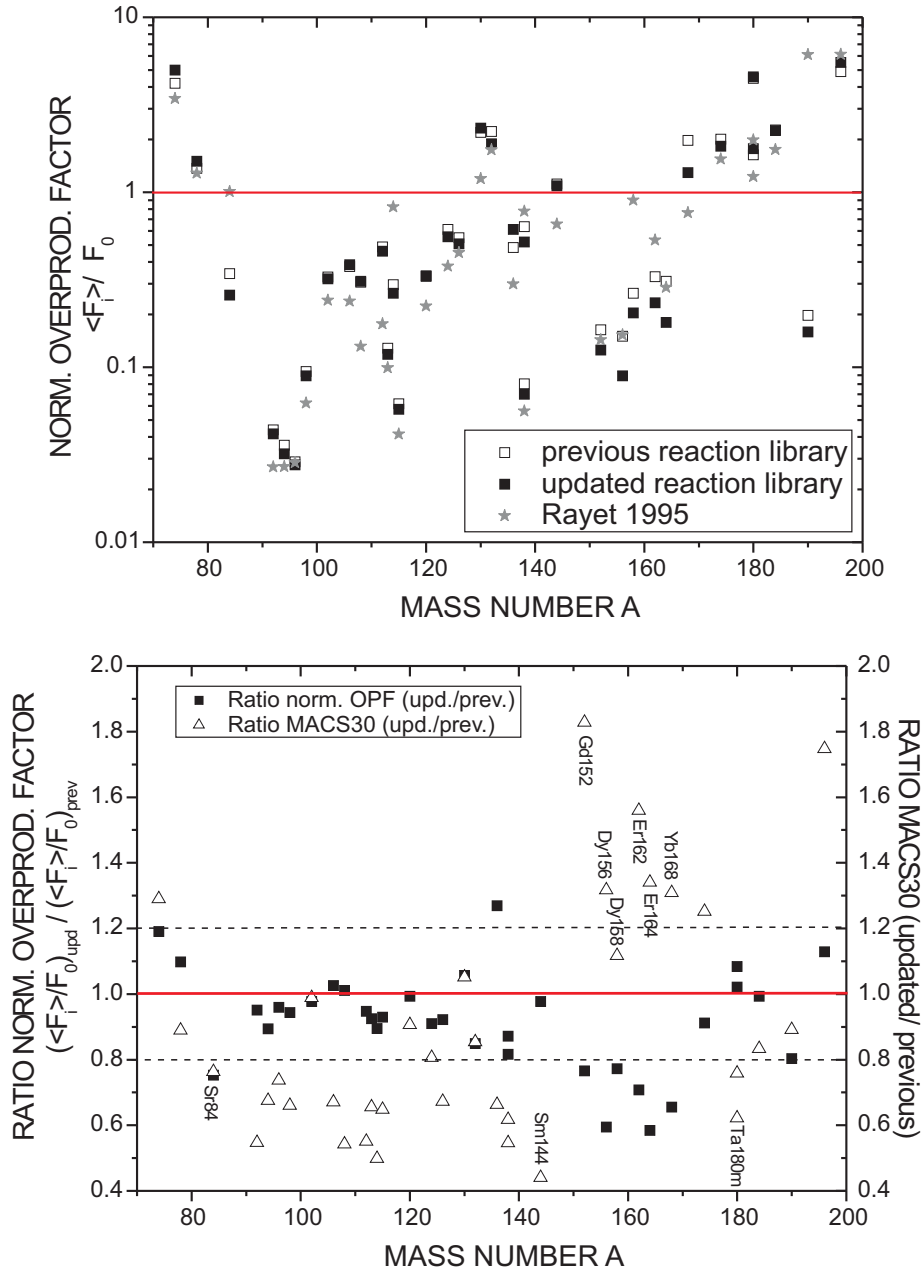
Figure 8.4: Top: Normalized overproduction factors derived with the previous (open squares) and the updated (full squares) reaction library. Additionally the values from a $25 M_\odot$ star model of Rayet et al. [6] are given for comparison (gray stars). Bottom: Ratio between the normalized overproduction factors in comparison with the ratio of previous and newly implemented MACS at $kT=30$ keV.
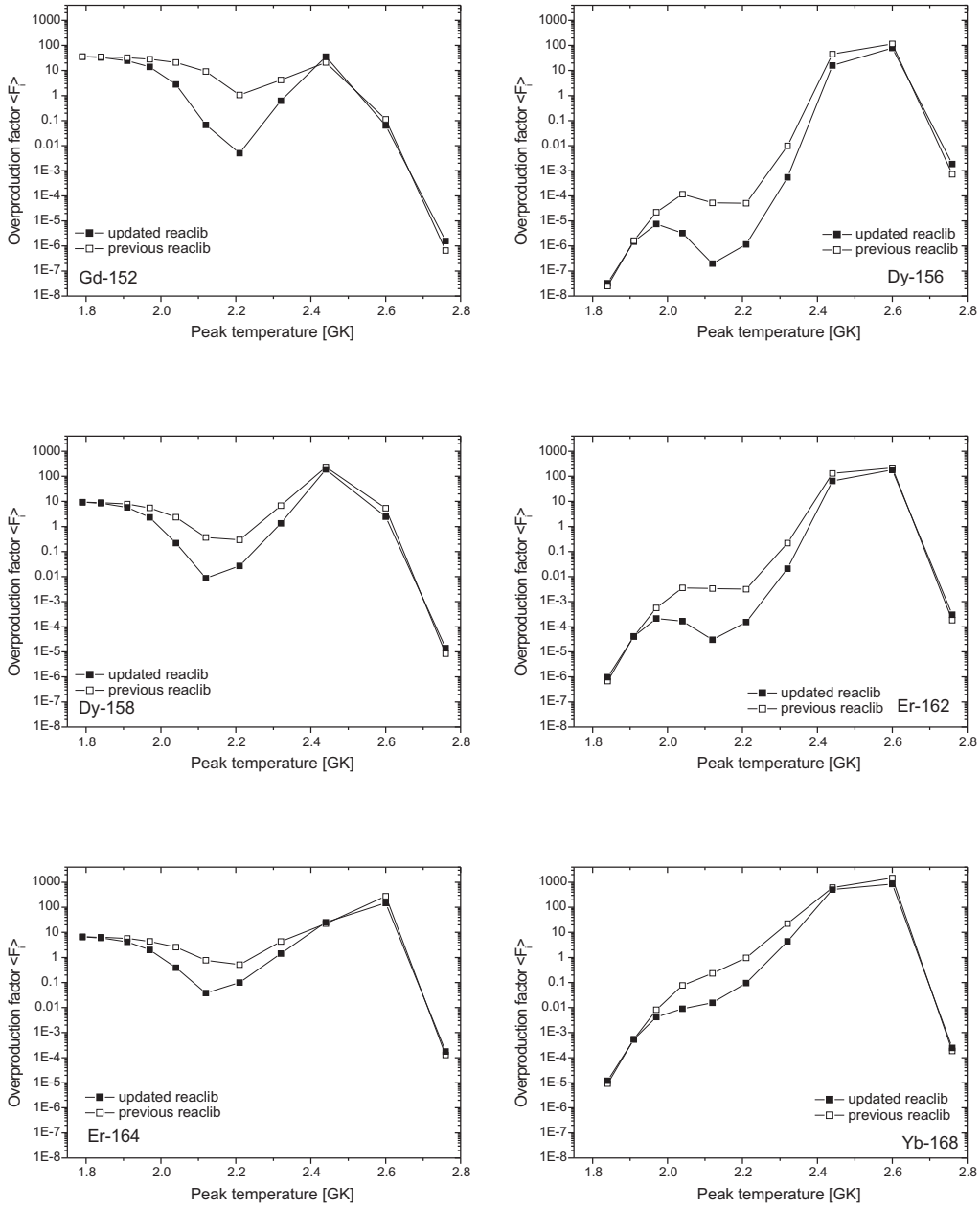
Figure 8.5: Overproduction factors for ^{152}Gd, ^{156}Dy, ^{158}Dy, ^{162}Er, ^{164}Er, and ^{168}Yb. Shown are the peak temperatures (corresponding to Ne/O layers) at which they are produced.

8.3 Discussion

These surprising results have been investigated further. Reaction flux plots for both layers were integrated over 1 s (Fig. 8.6) and reveal –as expected for the γ process– that the main reaction flow comes down from the Pb region to lighter masses. The line thicknesses here indicate different flow strengths of 10^{-2}, 10^{-4}, and 10^{-6} compared to the strongest reaction flux in that mass region, ^{208}Pb$(\gamma, n)^{207}$Pb. The direction of the reaction flow is shown in detail in Fig. 8.7 where one sees that the main flow in this region proceeds via (γ, n) and (γ, α) reactions but also via (n, γ) and (n, α) reactions. In the top part of Fig. 8.7 one can see that the strongest reaction flows are ^{152}Gd$(n, \gamma)^{153}$Gd, ^{158}Dy$(n, \gamma)^{159}$Dy, ^{164}Er$(n, \gamma)^{165}$Er, and ^{169}Yb$(\gamma, n)^{168}$Yb, so the experimental (n, γ) cross sections of the p isotopes included in the updated reaction library directly have an influence on their production and destruction. Comparisons show that the "new" reaction flow is up to a factor of 60 less compared to the flow simulated with the previous library.

However, since the strength of these flows is strongly dependent on the chosen initial seed abundances (see Fig. 8.1) no direct conclusion can be draw which reaction is really the most important one for this mass region. Therefore the simulations were repeated with unified seed abundances Y_i for all isotopes starting from ^{56}Fe. The respective value for Y_i was calculated from the mass fractions X and the mass number A via $Y_i = \frac{\Sigma X_i}{\Sigma A_i}$ and yielded $Y_i = 5.035 \times 10^{-7}$. The resulting reaction flow is shown in the bottom part of Fig. 8.7. Now one sees that the (n, γ) reactions play a crucial role for the destruction of the above mentioned six isotopes, and (γ, n) reactions only for the destruction of ^{152}Dy. However, this reflects only the situation in the layers 165 and 166 and might be different for higher and lower temperatures.

Thus a part of the lower production of the p isotopes could be explained by the stronger (n, γ) destruction channel but not all. The abundance evolution versus time for all 32 p isotopes in layers 165 and 166 (Fig. 8.8 and 8.9), as well as the abundance evolution versus temperature (Fig. 8.10) show that for all p isotopes and all layers the production with the updated reaction library is lower. From the temperature-dependent abundance evolution in Fig. 8.10 it is also confirmed that light p nuclei are produced at higher temperatures ($T_{peak} >3$ GK), whereas for heavier p nuclei the production curve is shifted to lower temperatures ($T_{peak}=2.2$-2.4 GK). For the dip occurring for light p isotopes in layer 164 ($T_{peak}= 2.4$ GK) there is up to now no plausible explanation.

The lower production of all p isotopes with the updated reaction library seems to be (more or less) independent from the direct changes made in the (n, γ) cross sections of the respective p nuclei. This brings us back to the question which other changes might have such a global influence. The mechanism of the γ process leads us to heavier seed nuclei (see Fig. 8.1). Corresponding to lower cross sections at the closed neutron shells, we see the well-known s-process peaks at $A=90$ ($N=50$), $A=138$ ($N=82$), and $A=208$ ($N=126$). By comparison with the renormalization factors f^* in Table 7.2 one realizes that in these regions the previous theoretical cross sections have overestimated the cross sections by up to a factor of 5 (for ^{89}Y). In the Pb-Bi region, where $\approx 75\%$ of the total abundance for isotopes beyond ^{144}Sm
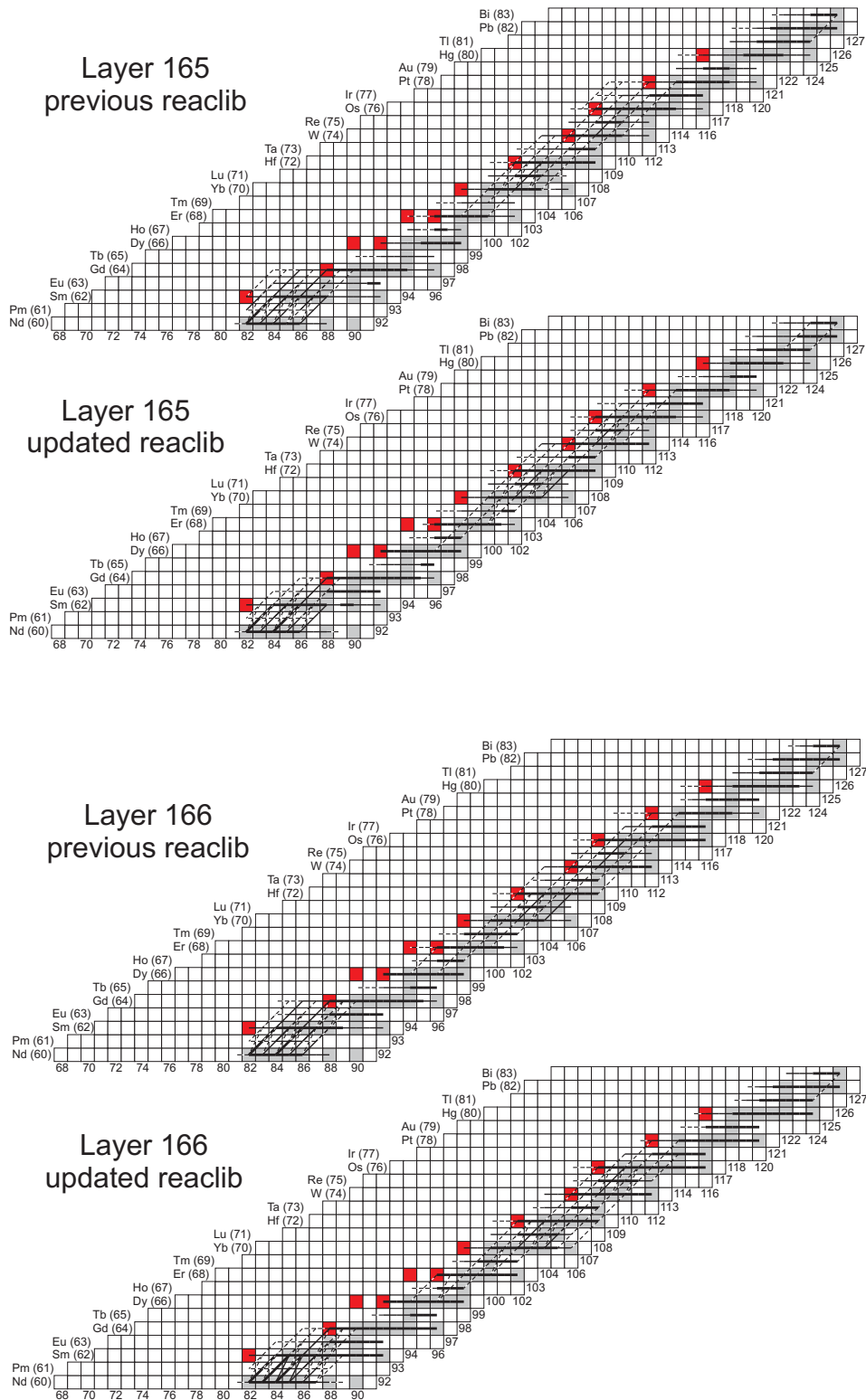
Figure 8.6: Reaction flux in layers 165 and 166. The line thicknesses correspond to flow strengths of 10^{-2} (thick line), 10^{-4} (thin line), and 10^{-6} (dashed line) compared to the strongest reaction flux in this mass region, $^{208}\text{Pb}(\gamma, n)^{207}\text{Pb}$.
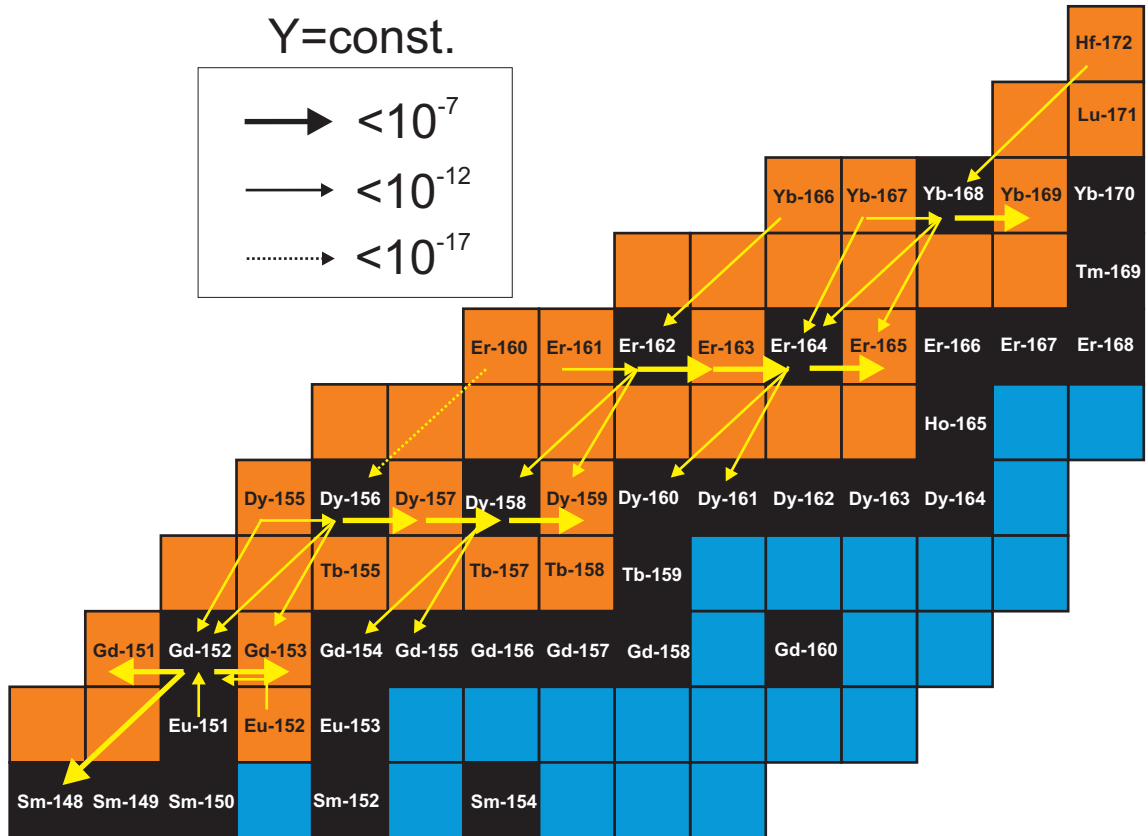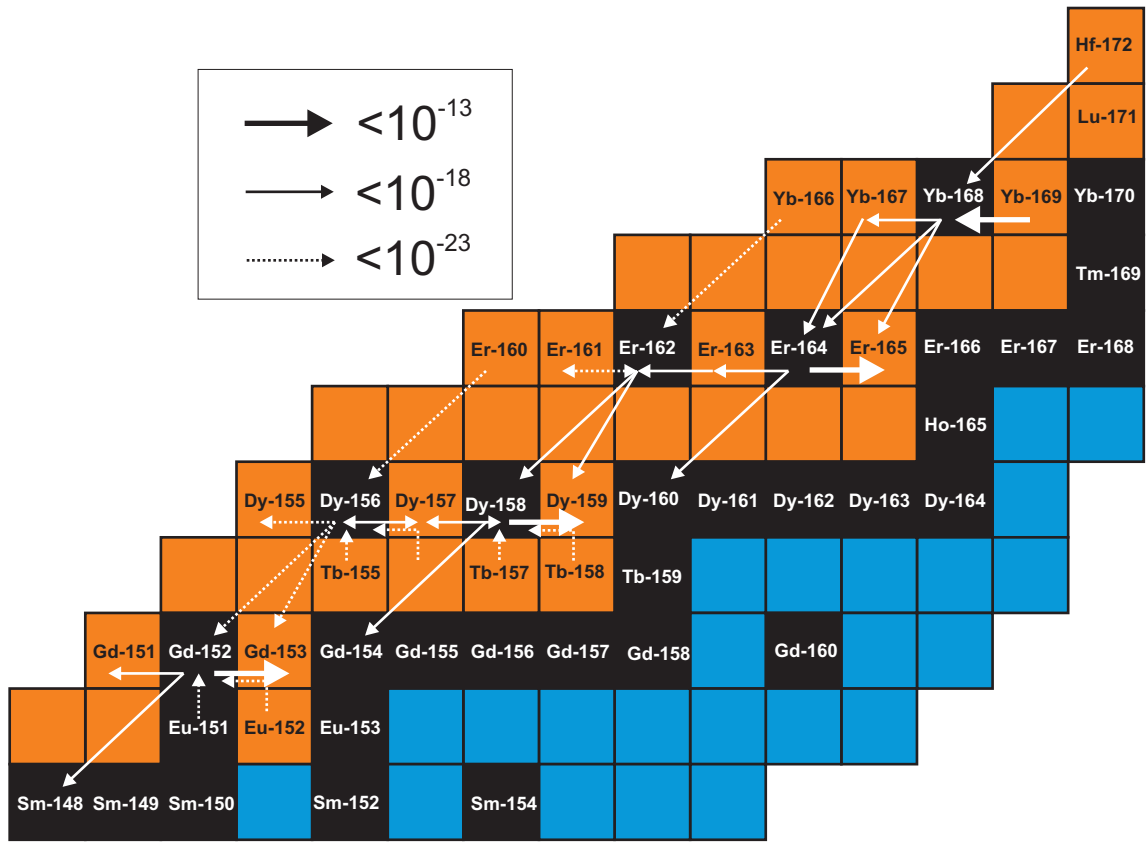
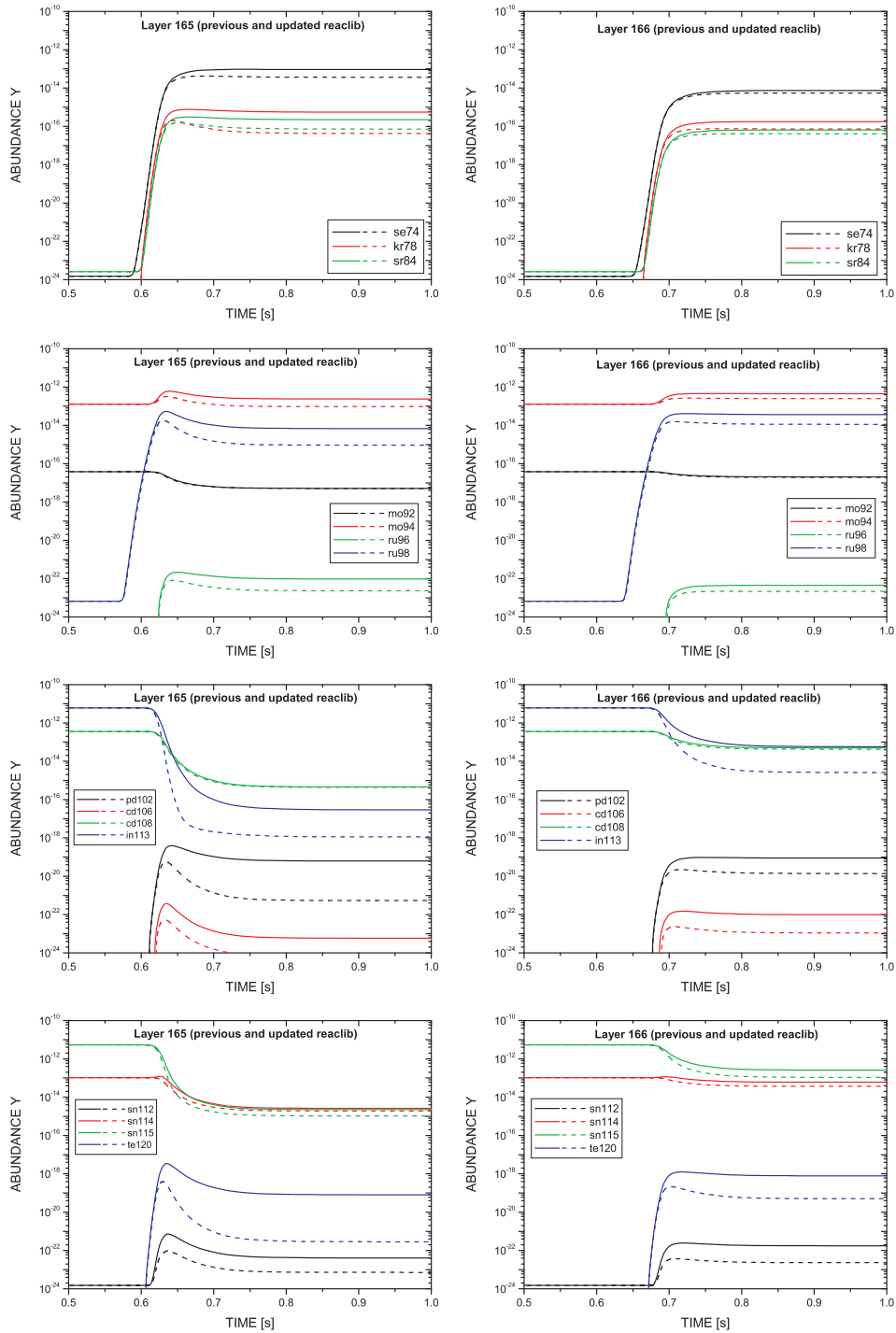Figure 8.7: Construction and destruction flows for $A \geq 150$.

Figure 8.8: Abundance evolution versus time for p isotopes between ^{74}Se and ^{120}Te in layers 165 (left) and 166 (right). Solid line: previous reaction library. Dashed line: updated reaction library.
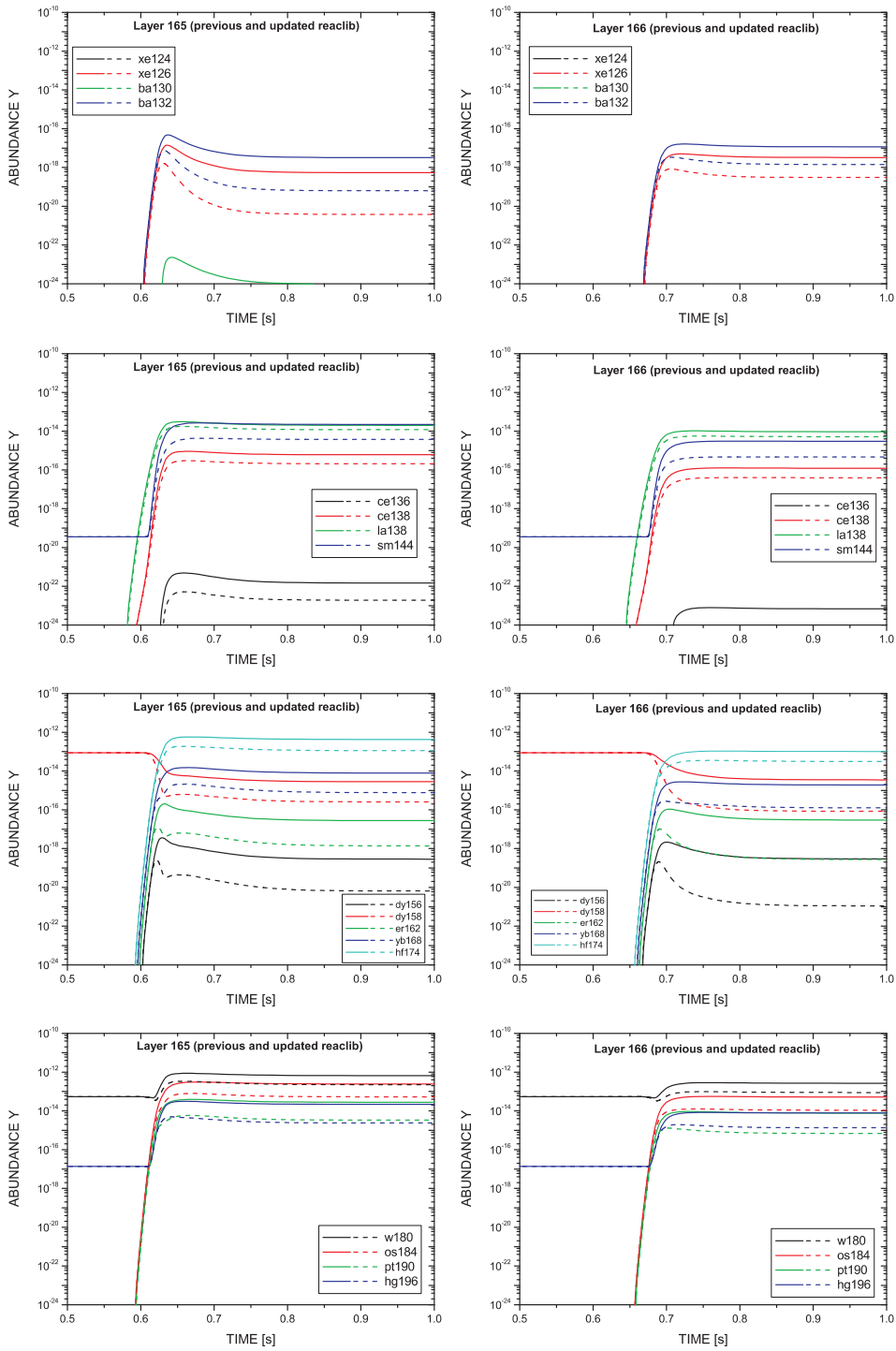
Figure 8.9: Abundance evolution versus time for p isotopes between ^{124}Xe and ^{196}Hg in layers 165 (left) and 166 (right). Solid line: previous reaction library. Dashed line: updated reaction library.
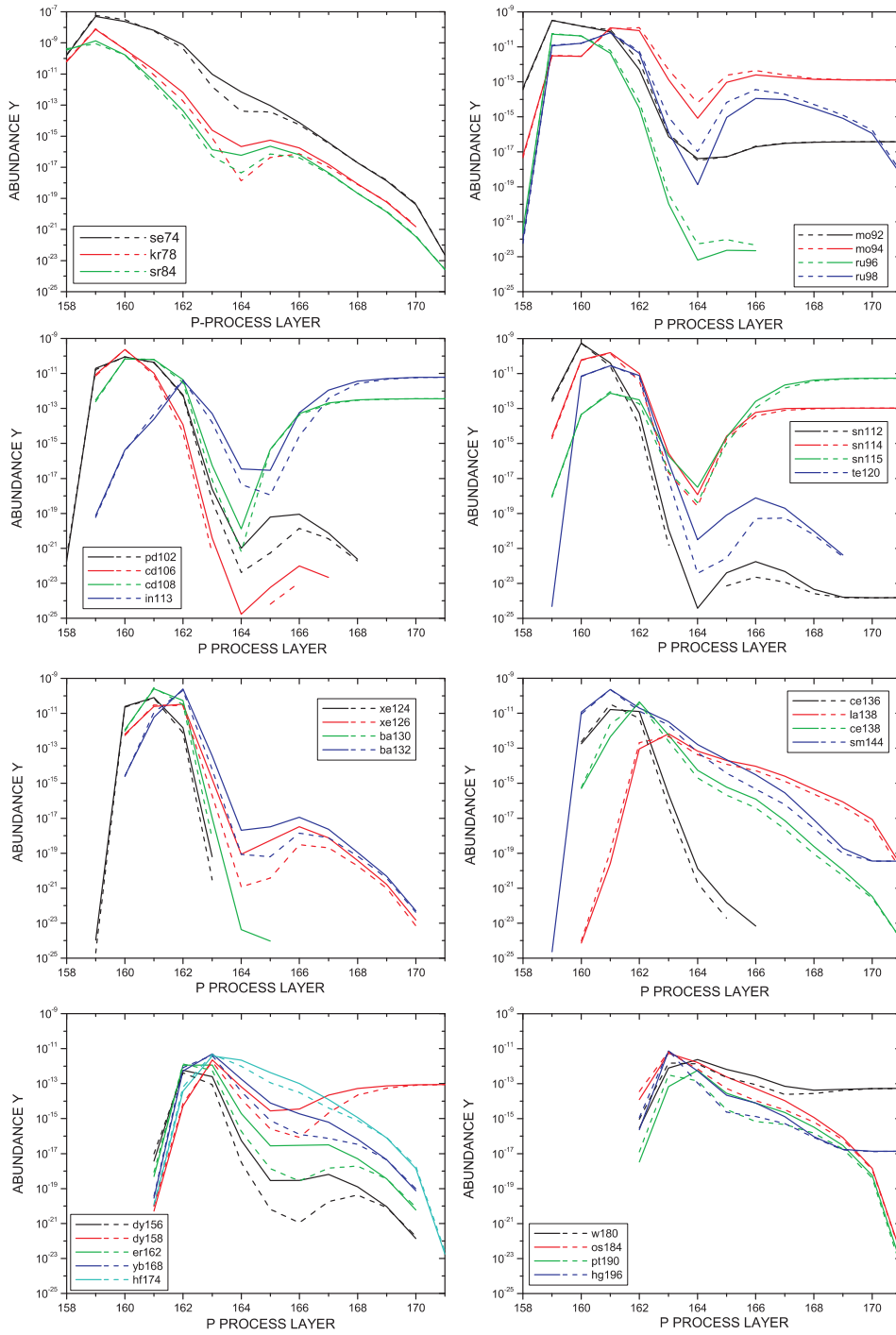
Figure 8.10: Abundance evolution versus temperature for all 32 p isotopes. Solid line: previous reaction library. Dashed line: updated reaction library.

is located, the (n, γ) cross sections of ^{206,207,208}Pb and ^{209}Bi were overestimated by a factor up to 3. This is one drawback we have to live with when we use statistical model predictions for cross sections where no experimental information is available. One reason is, as explained in Sec. 2.3.1, that the level densities at shell closures become too low, which results in an overestimation of cross sections. This can be clearly seen in Fig. 8.11. Plotted in this figure are only experimental results versus the respective previous NON-SMOKER prediction at kT=30 keV. Another reason is that the microscopic corrections for the FRDM [134] are too strong at shell closures but N-dependent corrections are possible (see semi-empirical estimates in the Bao et al. compilation [26]). One should also be careful because our comparison is made at kT=30 keV, but the predictive power of the NON-SMOKER code might become better at higher energies. The scattering in the region between the shell closures can be attributed to deformed nuclei. Mavericks to higher ratios, that means higher experimental cross sections, originate mostly from 30 year old time-of-flight measurements which might have underestimated scattering and capture in the detectors used and thus have determined higher cross sections. This systematic difference to previous activation measurements has been observed in the meantime for many light and medium-mass nuclei. For the cases where the statistical model can be applied, the average NON-SMOKER uncertainty for stellar (n, γ) cross sections is only $\pm 30\%$ or even better.

The observed global underproduction of p isotopes will not be restricted to the presently used star mass (25 $M_\odot$) but also reflected in all following simulations with different star masses. As can be seen in Fig. 2.4 [6, 31] the influence of a variation in the star mass is different for each p isotope. The light isotopes ^{74}Se, ^{78}Kr, and ^{84}Sr are strongly influenced by the progenitor star mass, whereas the abundances of isotopes like ^{102}Pd, ^{106}Cd, ^{174}Hf, and ^{180}W are not significantly changed.

In Fig. 8.12 is shown how much our p-process simulations contribute to the production of the so-called p isotopes. This can be calculated from the respective seed abundance before and after the simulations (see Fig. 8.1). Here clearly can be seen that ^{158}Dy, ^{180}Ta, and ^{180}W have already some s-process contributions and are not completely produced in the p process. ^{180}Ta is a special case, as already discussed in Sec. 2.2. Observed can only the long-lived isomeric state, but in the calculation also the short-lived ground-state is considered. This ground state decays via electron capture (86$\pm$3%) into ^{180}W which could explain that only 88% of the abundance are produced in the p process.

Significantly stronger destroyed than produced in our simulations are the nuclides in the bottom part of this figure, e.g. ^{152}Gd and ^{164}Er. This is consistent with previous work finding large s-process contributions to these nuclei. Also, the two odd-A isotopes ^{113}In and ^{115}Sn are not produced. The latter underproduction problem is known since a long time (see Fig. 2.4) [31, 6]. The initial seed abundances of ^{113}In and ^{115}Sn are destroyed by the γ process, since the destruction channel is much stronger than the production channel.

Nemeth et al. [137] determined the contributions for ^{113}In, and ^{115}Sn with the (outdated) classical s-process approach to be very small (less than 1% for both cases). These calculations in the Cd-In-Sn region are complicated since many isomeric states
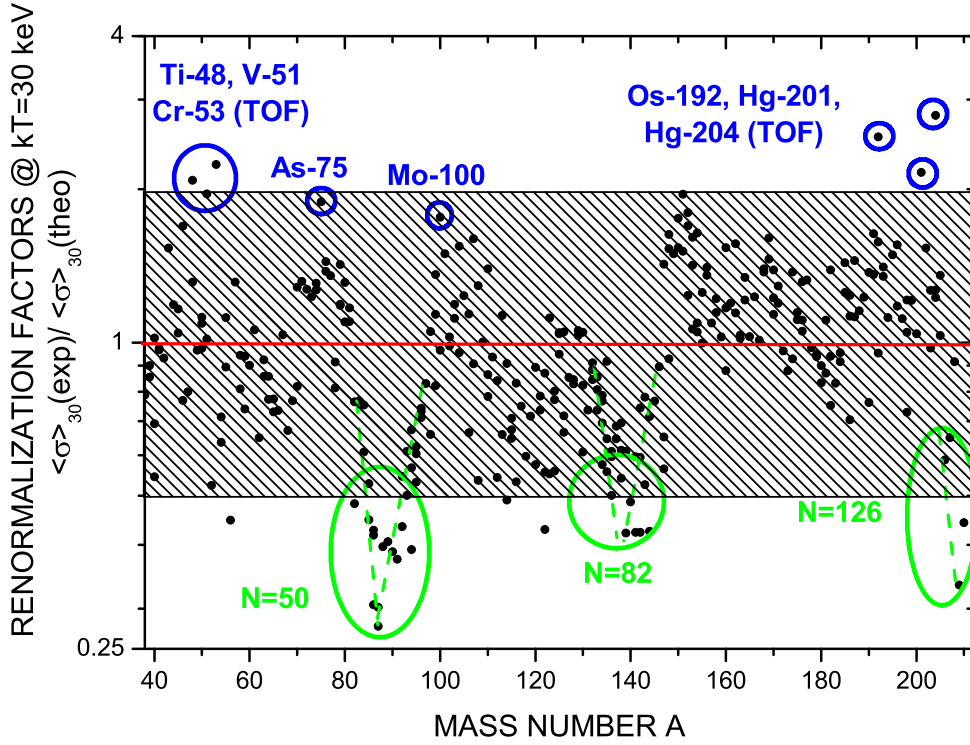
Figure 8.11: Renormalization factors for experimental (n, γ) cross sections compared to NON-SMOKER predictions versus A. Clearly seen can be the overestimation of statistical predictions around shell closures. For the largest part of the nuclides the agreement is within a factor of 2 (shaded area).

have to be considered, and the r-process may contribute to the abundances of ^{113}Cd and ^{115}In. Although these two isotopes have quasi-stable ground-states, the β-decays of r-process progenitor nuclei can proceed via isomeric states: $^{113g}Ag \rightarrow$ $^{113m}Cd \rightarrow {}^{113}$In and ^{115g}Cd $\rightarrow^{115m}In \rightarrow {}^{115}$Sn. In [137] only part of the missing abundances could be ascribed to post-r-process β-decay chains, leaving rather large residues for other production mechanisms. In view of the progress achieved in s-process calculations using the TP-AGB star model, and with the availability of an improved set of (n, γ) cross sections it appears worth while to update these older calculations. The new reaction library KADoNiS v0.2 [88] includes the latest Maxwellian averaged cross sections from very accurate time-of-flight measurements for the Cd and Sn isotopes [138, 139, 103, 102] and will soon be complemented by a measurement of the partial neutron capture cross section to the 14.1 y isomeric state in the s-process branching isotope ^{113}Cd with the activation technique, which is underway at Forschungszentrum Karlsruhe. With this additional information new calculations are expected to provide more accurate s- and r-contributions for
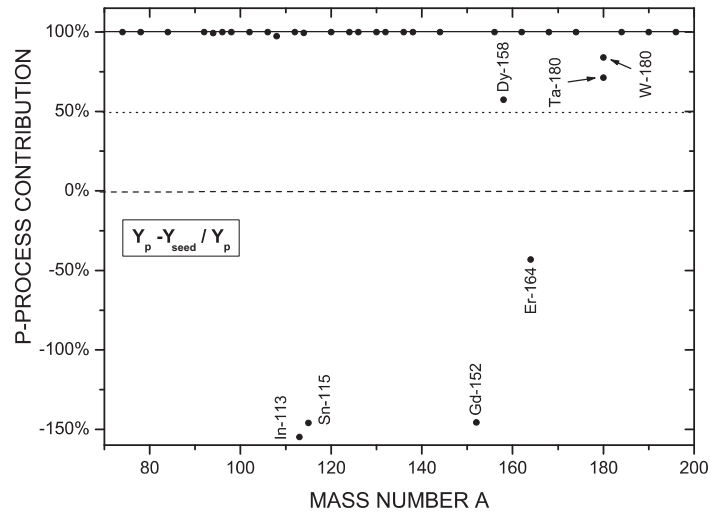
Figure 8.12: p-process contributions deduced from our simulations. It seems that ^{113}In, ^{115}Sn, ^{152}Gd, and ^{164}Er are not produced for this star mass by the p process.

^{113}Cd and ^{115}In. Based on these results, the p-contributions can be estimated as the residual via $N_p = N_\odot - N_s - N_r$.

Thus, it appears as if the nuclides ^{152}Gd, ^{164}Er, ^{113}In, and ^{115}Sn have strong contributions from other processes and it is conceivable that they even may not be assigned to the group of p nuclei. This means that in future we might have to speak about "30 p isotopes" (if we consider also the possible different contributions to the abundance of ^{180}Ta) rather than 32 or 35 isotopes. This statement should be check in following simulations with different star masses.

Chapter 9

Outlook

9.1 Parameter refitting

For isotopes with known experimental energy-dependences, e.g. as deduced from time-of-flight measurements with the Karlsruhe 4π BaF$_2$ detector, at ORELA (Oak Ridge Electron Linear Accelerator) and GELINA (Geel Electron Linear Accelerator), or most recently at CERN/n_TOF, it makes more sense to refit the data points and to deduce completely new coefficients.

Activation measurements, as discussed in Chapter 4, in most cases are only carried out at one energy and have to be extrapolated to lower and higher energies by either normalizing to the energy-dependence given in Bao 2000 [26], or by taking their dependence from a database. In the first case, for those isotopes for which only semi-empirical estimates were given, the energy-dependence corresponds to the normalized theoretical dependence from NON-SMOKER. The second case is a little bit more complicated. Since we get only a normalization factor for our experimental neutron distribution at kT=25 keV, we cannot – strictly speaking – use this factor for the whole energy region up to kT=100 keV (or even 260 keV for the p process). To use this normalization factor accurately, one would have to convert the resonances (e.g. in ^{130}Ba, Fig. 4.5, and ^{174}Hf, Fig. 4.7) to averaged cross sections, apply the normalization (in the proper energy region), and then recalculate every single resonance and its new width. This is easy for cases with few resonances, e.g. ^{102}Pd (Fig. 4.3), or if no resolved resonances are given, as for ^{120}Te and ^{132}Ba (Fig. 4.4 and 4.6). But for isotopes with many resonances, and if the resonances have an additional experimental uncertainty of 10-20%, as in most cases, this becomes a tedious task.

When the normalization factor indicates a large deviation between values from a published database and an experiment, this provides motivation for future TOF measurements and database evaluators. One nice example showing the necessity of refitting with experimental data is ^{22}Ne (see Fig. 9.1). In 2002 Beer et al. [95] performed a fast cycling activation measurement in which cross sections at kT= 52 keV, E$_n$= 149$\pm$20 keV, 180$\pm$20 keV, and 215$\pm$23 keV were measured. All of these measurements correspond to energies below the lowest (p wave) resonances starting at

266 keV. With these data points, calculations were carried out and Maxwellian averaged cross sections between $1 \leq kT \leq 250$ keV deduced. This data is plotted as reaction rate vs. T_9 in Fig. 9.1 (solid line). The normalized reaction library entry from [135] (dashed line) and the (not used) normalized NON-SMOKER entry [22] (dotted line) are shown for comparison. Nevertheless, as example for the refitting of the seven parameters, in Fig. 9.1 the data points from Beer et al. were extended towards the high temperature range above 3 GK with the normalized energy-dependence from [135]. The fit agrees rather well with the data points between 0.2 and 10 GK but deviates beyond that lower limit (corresponding to $kT < 17$ keV) significantly.

9.2 Future experiments for p-process studies

From the six remaining isotopes with only semi-empirical estimates, three can be easily determined by activation measurements: ^{168}Yb, ^{184}Os, and ^{196}Hg. This work is in progress at the Forschungszentrum Karlsruhe.

However, the activation technique is not applicable for ^{98}Ru, ^{138}La and ^{158}Dy. In these cases, only TOF measurements with enriched samples are possible. This is especially difficult for ^{138}La where no proper sample with enrichments $\geq 90\%$ exists because of its low natural abundance. However, since the ^{139}La cross section was recently measured at n_TOF, it might be possible to disentangle the respective ^{138}La resonances from ^{139}La resonances with a less enriched ^{138}La sample.

Concerning charged-particle reactions for p-process studies, in the last years much effort was undertaken from the groups at ATOMKI (Hungary), DEMOKRITOS (Greece) and also at FZK concerning (p, γ) and (α, γ) reactions on light nuclei. These attempts should also be supported and enlarged in the future, especially concerning α-induced reactions.

On the other hand, the direct determination of photodisintegration rates, as done by the groups at TU Darmstadt and Forschungszentrum Rossendorf in Germany, and at Kobe University in Japan provides important additional information for those cases which cannot be measured via the capture channel. However, up to now, mainly (γ, n) reactions on heavy targets were measured. It would be desirable to extend these measurements to medium-mass nuclei.

9.3 Systematic p-process studies

This work deals only with the first step forward to understand and solve the p-process puzzles. The next step should be the inclusion of the available proton- and α-induced reactions within or close to the the Gamow windows into the reaction library (see Sec. 6.2.2). Then, as soon as KADoNiS v1.0 is completed, one should re-calculate the s-process seed nuclei with these updated (n, γ) cross sections and again repeat the p-process simulations. Followed by this simulations over a wider range of initial star masses for SNII explosions should be carried out. Finally, also
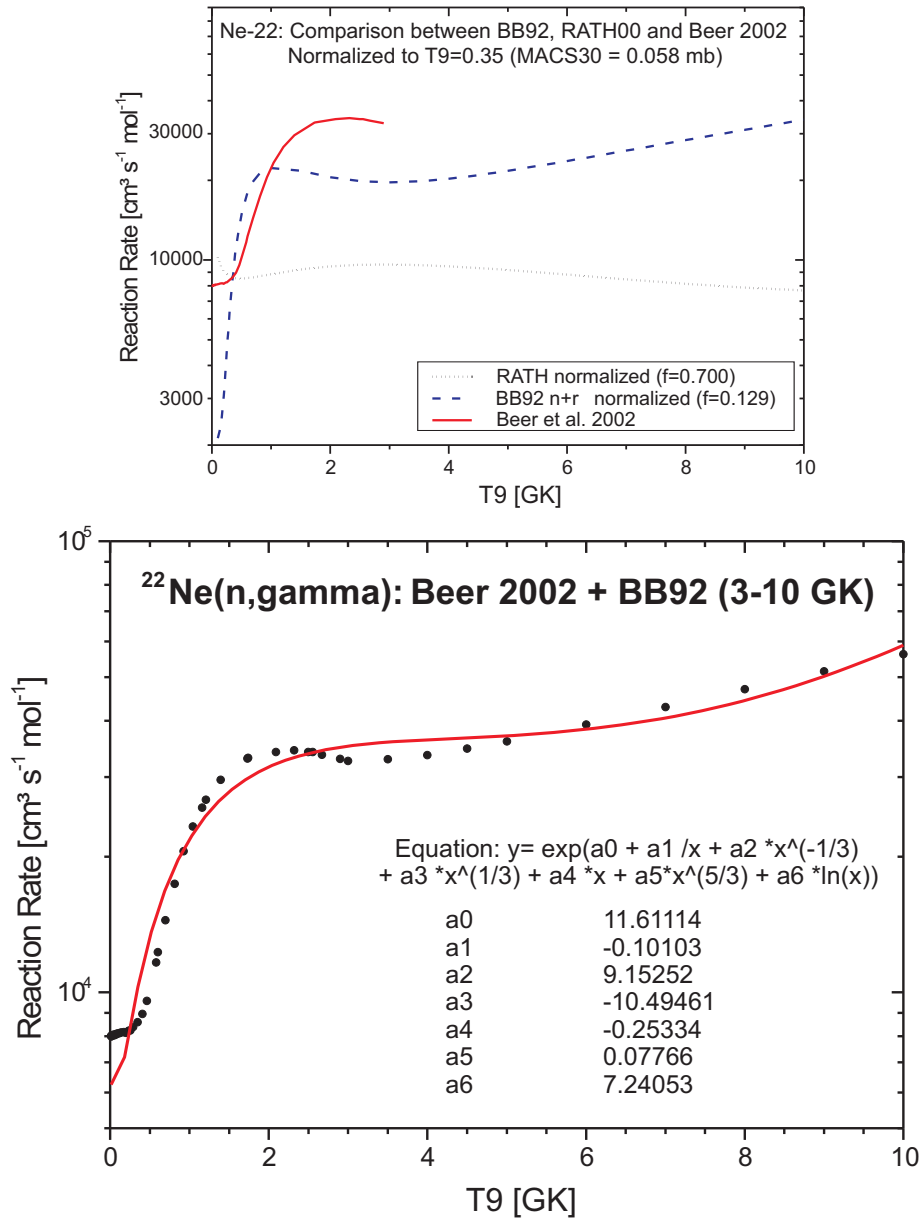
Figure 9.1: Top: Comparison of reaction rate predictions for ^{22}Ne. Bottom: Example for refitting of the ^{22}Ne(n, γ) rate by combination of the experimental data of [95] at lower energies with the normalized energy-dependence of [135] above T=3 GK.

abundances calculated with other astrophysical processes that might contribute to the p process should be included, e.g. the νp process.

Chapter 10

Summary

This Ph.D. thesis includes the experimental determination of stellar (n, γ) cross sections of the seven stable p-process isotopes ^{74}Se, ^{84}Sr, ^{102}Pd, ^{120}Te, ^{130,132}Ba, and ^{174}Hf at kT= 25 keV. All results are in perfect agreement with the previous recommended (predominantly semi-empirical) cross sections. Together with an update of the Bao et al. compilation [26], these new (n, γ) values are now available in the framework of the "Karlsruhe Astrophysical Database of Nucleosynthesis in Stars" project (http://nuclear-astrophysics.fzk.de/kadonis). The recommended cross sections from the most recent version KADoNiS v0.2 (status November 2006) are integrated in a reaction library and replace previous theoretical predictions. This updated reaction library was utilized to perform p-process network calculations with the program "pProSim". The results are compared with the previous data. The changes of the updated experimental (n, γ) rates on the overproduction factors, with exceptions of the rare earth metals ^{152}Gd, ^{156}Dy, ^{158}Dy, ^{162}Er, ^{164}Er, and ^{168}Yb of stable p isotopes lie within a factor of 1.5 ($\pm 20\%$). These isotopes exhibit now an even smaller overproduction factor, which is due to significantly lower cross sections in the Pb-Bi region. Thus, the observed underproduction of most p isotopes relative to the solar abundances is still existing, as well as the overproduction of ^{74}Se, ^{78}Kr, and for $A \geq 160$.

Furthermore we measured the proton-induced cross sections of Pd isotopes between 2.75 and 5 MeV, at the upper end of the respective Gamow window. We discovered a significantly smaller cross section for ^{102}Pd(p, γ) compared to a recent experiment of Özkan et al. [61], but in good agreement with NON-SMOKER calculations [22]. For all other cases, i.e. the total cross sections of ^{104}Pd(p, γ) and ^{105}Pd(p, n), and the partial isomeric cross sections of ^{105}Pd(p, γ), ^{106}Pd(p, n), and ^{110}Pd(p, n), there was no previous experimental data in the energy range relevant for the p process. The new experimental results agree within a factor of 2 with NON-SMOKER calculations.

Solution the p-process enigma still requires careful and dedicated efforts, both from experimentalists and theoreticians. The increasing amount of (p, γ), (α, γ), and particle-exchange (mainly (p, n)) data calls for a consistent integration into reaction libraries. The present work is the first step towards this overdue update, since all

previous p-process network calculations were based almost entirely on theoretical predictions with only some experimental information for light nuclei. For the case of (n, γ) rates it is advisable to re-check the list of implemented cross sections, if experimental energy-dependent cross sections (e.g. derived from time-of-flight measurements) are available. These dependencies should be favored over theoretical dependencies and the respective rates should be refitted.

However, it seems to become apparent that the reason for the discrepancy between the observed and the calculated solar p abundances is (not only) due to lack of experimental information but also due to the fact that a full understanding of the p-process mechanism and the astrophysical site obviously is still missing.

Chapter 11

Acknowledgements

Bibliography

[1] C.E. Rolfs and W.S. Rodney, *"Cauldrons in the Cosmos"*, The University of Chicago Press, (1988).

[2] E. Burbidge, G. Burbidge, W. Fowler, and F. Hoyle, Rev. Mod. Phys. **29**, (1957) 547.

[3] K. Langanke and M.C. Wiescher, Rep. Prog. Phys. **64**, (2001) 1657.

[4] S. Woosley and W. Howard, Ap. J. Suppl. **36**, (1978) 285.

[5] S. Woosley and W. Howard, Ap. J. **354**, (1990) L21.

[6] M. Rayet, M. Arnould, M. Hashimoto, N. Prantzos, and K. Nomoto, Astron. Astrophys. **298**, (1995) 517.

[7] T. Rauscher, A. Heger, R.D. Hoffman, and S.E. Woosley, Astrophys. J. **576**, (2002) 323.

[8] E. Anders and N. Grevesse, Geochim. Cosmochim. Acta **53**, (1989) 197.

[9] K. Lodders, Ap. J. **591**, (2003) 1220.

[10] R. Reifarth, M. Heil, F. Käppeler, F. Voss, K. Wisshak, F. Becvar, M. Krticka, R. Gallino, Y. Nagai, Phys. Rev. C **66** (2002) 064603

[11] M. Arnould and S. Goriely, Phys. Rep. **384**, (2003) 1.

[12] S.E. Woosley, D.H. Hartmann, R.D. Hoffman, W.C. Haxton, Ap. J. **356**, (1990) 272.

[13] S. Goriely, M. Arnould, I. Borzov, and M. Rayet, Astron. Astrophys. **375**, (2001) L35.

[14] A. Heger, E. Kolbe, W.C. Haxton, K. Langanke, G. Martinez-Pinedo, and S.E. Woosley, Phys. Lett. B **606**, (2005) 258.

[15] W. Howard, B. Meyer, and S. Woosley, Ap. J. **373**, (1991) L5.

[16] H. Schatz, A. Aprahamian, J. Görres, M.C. Wiescher, T. Rauscher, J. Rembges, F.-K. Thielemann, B. Pfeiffer, P. Möller, H. Herndl et al., Phys. Rep. **294**, (1998) 167.

[17] H. Schatz, A. Aprahamian, V. Barnard, L. Bildsten, A. Cumming, M. Oullette, T. Rauscher, F.-K. Thielemann, and M. Wiescher, Nucl. Phys. A **688**, (2001) 150c.

[18] K.S. Thorne and A.N. Zytkow, Ap. J. **212**, (1977) 832.

[19] C. Fröhlich, G. Martinez-Pinedo, M. Liebendörfer, F.-K. Thielemann, E. Bravo, W.R. Hix, K. Langanke, and N.T. Zinner, Phys. Rev. Lett. **96**, (2006) 142502.

[20] W. Hauser and H. Feshbach, Phys. Rev. **87**, (1952) 366.

[21] T. Rauscher, F.-K. Thielemann, and H. Oberhummer, Ap.J. **451**, (1995) L37.

[22] T. Rauscher and F.-K. Thielemann, At. Data Nucl. Data Tables **75**, (2000) 1.

[23] T. Rauscher and F.-K. Thielemann, At. Data Nucl. Data Tables **79**, (2001) 47.

[24] S. Goriely, *"Hauser-Feshbach rates for neutron capture reactions"* (version 09/12/02), http://www-astro.ulb.ac.be/Html/hfr.html.

[25] S. Goriely, *"Hauser-Feshbach rates for neutron capture reactions"* (version 08/26/05), http://www-astro.ulb.ac.be/Html/hfr.html.

[26] Z. Bao, H. Beer, F. Käppeler, F. Voss, K. Wisshak, and T. Rauscher, At. Data Nucl. Data Tables **76**, (2000) 70.

[27] P. Descouvemont and T. Rauscher, Nucl. Phys. A **777**, (2006) 137.

[28] T. Rauscher, F.-K. Thielemann, and K.-L. Kratz, Phys. Rev. C **56**, (1997) 1613.

[29] N. Bohr, Nature 137, (1936) 344.

[30] J. Holmes, S.E. Woosley, W. Fowler, B. Zimmerman, At. Data Nucl. Data Tables **18**, 305 (1976).

[31] M. Rayet, N. Prantzos, and M. Arnould, Astron. Astrophys. **227**, (1990) 271.

[32] S. Woosley, *"Nucleosynthesis and Chemical Evolution"*, eds. B. Hauck, A. Maeder, G. Meynet, Observatoire de Genève, p.1.

[33] N. Prantzos, M. Arnould, J.-P. Arcoragi, Ap. J. **315**, (1987) 209.

[34] R.R. Winters and R.L. Macklin, Ap. J. **329**, (1988) 943.

[35] H. Beer, P.V. Sedyshev, W. Rochow, P. Mohr, and H. Oberhummer, Nucl. Phys. A **705**, (2002) 239.

[36] T. Rauscher, Nucl. Phys. A 758, (2005) 549c.

[37] W. Rapp, Report FZKA 6956, Forschungszentrum Karlsruhe (2004).

[38] W. Rapp, J. Görres, M. Wiescher, H. Schatz, and F. Käppeler, Ap. J. 653, (2006) 474.

[39] M. Heil, S. Dababneh, A. Juseviciute, F. F. Käppeler, R. Plag, R. Reifarth, and S. O Brien, Phys. Rev. C**71**, 025803 (2005)

[40] H. Beer and F. Käppeler, Phys. Rev. C **21**, (1980) 534.

[41] F. Käppeler, A.A. Naqvi, and M. Al-Ohali, Phys. Rev. C**35**, 936 (1987).

[42] W. Ratynski and F.Käppeler, Phys. Rev. C **37**,(1988) 595.

[43] K. Rosman and P. Taylor, Pure and Appl. Chem. **70**, (1998) 217.

[44] C.L. Smith, K.J.R. Rosman, and J.R. de Laeter, Int. J. Mass Spectrom. Ion Phys. **28**, (1978) 7.

[45] P.J. Patchett, Geochim. Cosmochim. Acta **47**, (1983) 81.

[46] S. Dababneh, N. Patronis, P.A. Assimakopoulos, J. Görres, M. Heil, F. Käppeler, D. Karamanis, S. O'Brien, and R. Reifarth, Nucl. Instr. Meth. A **517**, (2004) 230.

[47] S. Dababneh, *private communication*.

[48] CERN, Geant home page: *http://wwwinfo.cern.ch/asd/geant4/geant4.html* (2002).

[49] J.H. Hubbell and S.M. Seltzer, *"Table of X-Ray Mass Attenuation Coefficients and Mass Energy-Absorption Coefficients"* (v. 1.4), National Institute of Standards and Technology, Gaithersburg, MD; *http://physics.nist.gov/PhysRefData/XrayMassCoef/* (2004).

[50] A.R. Farhan and B. Singh, Nucl. Data Sheets **86**, (1999) 785.

[51] H. Sievers, Nucl. Data Sheets **62**, (1991) 271.

[52] D. de Frenne and E. Jacobs, Nucl. Data Sheets **93**, (2001) 447.

[53] T. Tamura, Nucl. Data Sheets **90**, (2000) 107.

[54] Yu.V. Sergeenkov, Yu.L.Khazov, T.W. Burrows, M.R. Bhat, Nucl. Data Sheets **72**, (1994) 487.

[55] R. Shaheen, Nucl. Data Sheets **75**, (1995) 491.

[56] Yu.V. Sergeenkov and V.M. Sigalov, Nucl. Data Sheets **49**, (1986) 639.

[57] M.S. Basunia, Nucl. Data Sheets **102**, (2004) 719.

[58] Z. Chunmei, Nucl. Data Sheets **95**, (2002) 59.

[59] S. Mughabghab, M. Divadeenam, and N. Holden, Neutron Cross Sections, BNL-325, 1st ed., Vol. 1 (1981).

[60] S.F. Mughabghab, Atlas of Neutron Resonances- Resonance Parameters and Thermal Cross Sections $Z=$ 1-100, 5th Edition, Elsevier (2006), ISBN 0444 52035X.

[61] N. Özkan, A.St.J. Murphy, R.N. Boyd, A.L. Cole, M. Famiano, R.T. Güray, M. Howard, L. Sahin, J.J. Zach, R. deHaan, J. Görres, M.C. Wiescher, M.S. Islam, and T. Rauscher, Nucl. Phys. A **710**, (2002) 469.

[62] D. de Frenne and E. Jacobs, Nucl. Data Sheets **105**, (2005) 775.

[63] D. de Frenne and E. Jacobs, Nucl. Data Sheets **72**, (1994) 1.

[64] D. de Frenne and E. Jacobs, Nucl. Data Sheets **89**, (2000) 481.

[65] K. Debertin and R.G. Helmer, "Gamma- and X-Ray Spectrometry With Semiconductor Detectors", North Holland (1989), ISBN 0444871071.

[66] J.F. Ziegler and J.F. Biersack, *"The stopping and range of ions in matter"*, SRIM-2003.26, http://www.srim.com

[67] Joint Evaluated Fission and Fusion General Purpose File, online: http://www.nea.fr/html/dbdata/JEFF/

[68] K. Shibata, T. Kawano, and T. Nakagawa, Japanese Evaluated Nuclear Data Library Version 3 Revision 3: JENDL 3.3, J. Nucl. Sci. Technol. **39**,(2002) 1125.

[69] National Nuclear Data Center, Brookhaven NH: ENDF/B-VI Release 8; Online: www.nndc.bnl.gov/exfor1/endf00.htm, (2004).

[70] JANIS, NEA, online: http://www.nea.fr/janis

[71] S. Sukhoruchkin, Z. Soroko, and V. Deriglazov, Landolt-Börnstein, Group I: Elementary Particles, Nuclei and Atoms, Vol. 16; Low Energy Neutron Physics - Subvolume B; edited by H. Schopper (1998).

[72] S. Igarasi, J. Nucl. Sci. Technol. **12**, (1975) 67.

[73] T. Bradley, Z. Parsa, M. Stelts, and R. Chrien, in *Nuclear Cross Sections for Technology*, edt. by J.L. Fowler, C.H. Johnson, and C.D. Bowman (National Bureau of Standards, Washington D.C.), (1979) 344.

[74] M.J. Trbovich et al., Int. Conf. on Nuclear Data for Science and Technology, Santa Fe/ NM, USA (2004), AIP Conf. Proc. **769**, (2005) 949.

[75] C. Vockenhuber, I. Dillmann, M. Heil, F. Käppeler, N. Winckler, W. Kutschera, A. Wallner, M. Bichler, S. Dababneh, S. Bisterzo, and R. Gallino, Phys. Rev. C **75**, (2006) 015804.

[76] K. Wisshak, F. Voss, F. Käppeler, and L. Kazakov, Phys. Rev. C **73**, (2006) 045807.

[77] I. Dillmann, M. Heil, F. Käppeler, T. Rauscher, and F.-K. Thielemann, Phys. Rev. C **73**, (2006) 015803.

[78] B. Allen, J. Gibbons, and R. Macklin, Adv. Nucl. Phys. **4**, (1971) 205.

[79] S.E. Woosley, W. Fowler, J. Holmes, B. Zimmerman, At. Data Nucl. Data Tables **22**, 371 (1978).

[80] M. Harris, Astrophys. Space Sci. **77**, 357 (1981).

[81] Z. Zhao, D. Zhou, D. Cai, Nuclear Data for Science and Technology, edited by S. Igarasi (Saikon, Tokyo), 513 (1988).

[82] W. Rapp, M. Heil, D. Hentschel, F. Käppeler, R. Reifarth, H.J. Brede, H. Klein, and T. Rauscher, Phys. Rev. C **66**, (2002) 015803.

[83] V.G. Batij, E.A. Skakun, Ju. N. Rakivnenko, and O.A. Rastrepin, Proc. 36th Conference on "Nucl. Spectr. and Nucl. Struc.", Kharkov/USSR, (1986) 280.

[84] H. Bitao, P.P. Zarubin, U.U. Juravlev, Eur. Phys. J. **A**2, (1998) 143.

[85] C.H. Johnson, A. Galonsky, C.N. Inskeep, Oak Ridge Natinal Laboratory Reports ORNL-2910, (1960) 25.

[86] Z. Bao, and F. Käppeler, At. Data Nucl. Data Tables **36**, (1987) 411.

[87] H. Beer, F. Voss, and R. Winters, Ap. J. Suppl. **80**, (1992) 403.

[88] I. Dillmann, M. Heil, F. Käppeler, R. Plag, T. Rauscher, and F.-K. Thielemann, AIP Conf. Proc **819** (2006) 123; online at http://nuclear-astrophysics.fzk.de/kadonis

[89] I. Dillmann, M. Heil, F. Käppeler, T. Faestermann, G. Korschinek, K. Knie, A. Wallner, and T. Rauscher, Proc. "Nuclei in the Cosmos-IX", CERN, Geneva, Proceedings of Science PoS(NIC-IX)089 (2006).

[90] R. Reifarth, M. Heil, F. Käppeler, F. Voss, K. Wisshak, F. Becvar, M. Krticka, R. Gallino, and Y. Nagai, Phys. Rev. C **66**, (2002) 064603.

[91] R. Reifarth, C. Arlandini, M. Heil, F. Käppeler, P.V. Sedishev, A. Mengoni, M. Herman, T. Rauscher, R. Gallino, and C. Travaglio, Ap. J. **582**, (2003) 1251.

[92] K. Wisshak, F. Voss, F. Käppeler, M. Krticka, S. Raman, A. Mengoni and R. Gallino, Phys. Rev. C **73**, (2006) 015802.

[93] K. Wisshak, F. Voss, C. Arlandini, F. Käppeler, M. Heil, R. Reifarth, M. Krticka, and F. Becvar, Phys. Rev. C **69**, (2004) 055801.

[94] E. Uberseder, M. Heil, F. Käppeler, J. Görres, and M. Wiescher, *submitted to Phys. Rev. C* (2006).

[95] H. Beer, P.V. Sedyshev, W. Rochow, P. Mohr, and H. Oberhummer, Nucl. Phys. A **705**, (2002) 239.

[96] K. Guber, P.E. Koehler, H. Derrien, T.E. Valentine, L.C. Leal, R.O. Sayer, and T. Rauscher, Phys. Rev. C**67**, (2003) 062802.

[97] K. Guber, R.O. Sayer, T.E. Valentine, L.C. Leal, R.R. Spencer, J.A. Harvey, P.E. Koehler, and T. Rauscher, Phys. Rev. C**65**, (2002) 058801.

[98] L. Coquard, F. Käppeler, I. Dillmann, A. Wallner, K. Knie, and W. Kutschera, Proc. 9th Conf. "Nuclei in the Cosmos", Geneva/Switzerland (2006), Proceedings of Science (pos.sissa.it), PoS(NIC-IX)274.

[99] P.E. Koehler, R.R. Winters, K.H. Guber, T. Rauscher, J.A. Harvey, S. Raman, R.R. Spencer, J.C. Blackmon, D.C. Larson, D.W. Barayan, and T.A. Lewis, Phys. Rev. C**62**, (2000) 055803.

[100] G. Tagliente and the n_TOF Collaboration, Proc. 9th Conf. "Nuclei in the Cosmos", Geneva/Switzerland (2006), Proceedings of Science (pos.sissa.it), PoS(NIC-IX)227.

[101] F. Gunsing, A. Lepretre, C. Mounier, C. Raepsaet, A. Brusegan, and E. Macavero, Phys. Rev. C**61**, (2000) 054608.

[102] K. Wisshak, F. Voss, F. Käppeler, and L. Kazakov, Phys. Rev. C**66**, (2002) 025801.

[103] P.E. Koehler, J.A. Harvey, R.R. Winters, K.H. Guber, and R.R. Spencer, Phys. Rev. C**64**, (2001) 065802.

[104] N. Patronis, S. Dababneh, P.A. Assimakopoulos, R. Gallino, M. Heil, F. Käppeler, D. Karamanis, P.E. Koehler, A. Mengoni, and R. Plag, Phys. Rev. C**69**, (2004) 025803.

[105] S. O'Brien, S. Dababneh, M. Heil, F. Käppeler, R. Plag, R. Reifarth, R. Gallino, and M. Pignatari, Phys. Rev. C**68**, (2003) 035801.

[106] S. Marrone and the n_TOF Collaboration, Phys. Rev. C**73**, (2006) 034604.

[107] K. Wisshak, F. Voss, F. Käppeler, and L. Kazakov, Report FZKA 6961, Forschungszentrum Karlsruhe (2004).

[108] C. Domingo-Pardo, and the n_TOF Collaboration, subm. to Phys. Rev. C (2006).

[109] C. Domingo-Pardo, and the n_TOF Collaboration, Phys. Rev. C 74,(2006) 055802.

[110] M.R. Anderson, S.R. Kennett, Z.E. Switkowski, D.G. Sargood, Nucl. Phys. A**316**, (1979) 471.

[111] F.K. McGowan, P.H. Stelson, W.G. Smith, Phys. Rev. **133**, (1964) 907.

[112] J.L. Zyskind, J.M. Davidson, M.T. Esat, M.H. Shapiro, R.H. Spear, Nucl. Phys. A**331**, (1979) 180.

[113] M.S. Basunia, E.B. Norman, H.A. Shugart, A.R. Smith, M.J. Dolinski, and B.J. Quiter, Phys. Rev. C**71**, (2005) 035801.

[114] Zs. Fülöp, A.Z. Kiss, E. Somorjai, C.E. Rolfs, H.P. Trautvetter, T. Rauscher, and H. Oberhummer, Z. Phys. A **355**, (1996) 203.

[115] Gy. Gyürky, G.G. Kiss, Z. Elekes, Zs. Fülöp, E. Somorjai,A. Palumbo, J. Görres, H.Y. Lee, W. Rapp, M. Wiescher, N. Özkan, R.T. Güray, G. Efe, and T. Rauscher, Phys. Rev. C**74**, (2006) 025805.

[116] E. Somorjai, Zs. Fülöp, A.Z. Kiss, C.E. Rolfs, H.P. Trautvetter, U. Greife, M. Junker, S. Goriely, M. Arnould, M. Rayet, T. Rauscher, and H. Oberhummer, Astron. Astrophys. **333**, (1998) 1112.

[117] G.A. Krivonosov, B.A. Nemashkalo, O.I. Ekhichev, et al., 24th Conf. on Nuclear Spectroscopy and Nuclear Structure, Kharkov/ USSR 1974, p. 352.

[118] C.W. Cheng, J.D. King, Can. Journ. of Phys. 58, (1980) 1677.

[119] G.A. Krivonosov, B.A. Nemashkalo, O.I. Ekhichev, et al., Izv. Rossiiskoi Akademii Nauk, Ser. Fiz. 41, Issue 10, (1977) 2196.

[120] C.W. Tingwell, L.W. Mitchell, M.E. Sevior, D.G. Sargood, Nucl. Phys. A439, (1985) 371.

[121] M.E. Sevior, L.W. Mitchell, M.R. Anderson, C.W. Tingwell,D.G. Sargood, Austr. Jour. of Phys. **36**, (1983) 463.

[122] S. Qiang, Ph.D. thesis, University of Kentucky, Lexington/USA (1990).

[123] M.T. Esat, R.H. Spear, J.L. Zyskind, M.H. Shapiro, W.A. Fowler, J.M. Davidson, Phys. Rev. C**23**, (1981) 1822.

[124] Gy. Gyürky, Zs. Fülöp, E. Somorjai, M. Kokkoris, S. Galanopoulos, P. Demetriou, S. Harissopulos, T. Rauscher, and S. Goriely, Phys. Rev. C**68**, (2003) 055803.

[125] Gy. Gyürky, E. Somorjai, Zs. Fülöp, S. Harissopulos, P. Demetriou, and T. Rauscher, Phys. Rev. C**64**, (2001) 065803.

[126] S. Galanopoulos, P. Demetriou, M. Kokkoris, S. Harissopulos, R. Kunz, M. Fey, J.W. Hammer, Gy. Gyürky, Zs. Fülöp, E. Somorjai, and S. Goriely, Phys. Rev. C**67**, (2003) 015801.

[127] P. Tsagari, M. Kokkoris, E. Skreti, A.G. Karydas, S. Harissopulos, T. Paradellis, and P. Demetriou, Phys. Rev. C**70**, (2004) 015802.

[128] C.E. Laird, D. Flynn, R.L. Hershberger, and F. Gabard, Phys. Rev. C35, (1987) 1265.

[129] F.R. Chloupek, A.S.J. Murphy, R.N. Boyd, A.L. Cole, J. Görres, R.T. Güray, G. Raimann, J.J. Zach, T. Rauscher, J.V. Schwarzenberg, P. Tischhauser, and M.C. Wiescher, Nucl. Phys. A **652**, (1999) 391.

[130] S. Harissopulos, E. Skreti, P. Tsagari, G. Souliotis, P. Demetriou, T. Paradellis, J.W. Hammer, R. Kunz, C. Angulo, S. Goriely, and T. Rauscher, Phys. Rev. C**64**, (2001) 055804.

[131] T. Sauter and F. Käppeler, Phys. Rev. C**55**, (1997) 3127.

[132] J. Bork, H. Schatz, F. Käppeler, and T. Rauscher, Phys. Rev. C**58**, (1998) 524.

[133] F.-K. Thielemann, M. Arnould, and J.W. Truran, in *Advances in Nuclear Astrophysics*, edts. by E. Vangioni-Flam et al., (Editions Frontière, Gif-sur-Yvette),(1987) 525.

[134] P. Möller, J.R. Nix, and K.-L. Kratz, At. Data Nucl. Data Tables **66**, (1997) 131.

[135] T. Rauscher, J.H. Applegate, J.J. Cowan, F.-K. Thielemann, and M. Wiescher, Ap. J. **429**, (1994) 499.

[136] T. Yoshida and M. Hashimoto, private communication to W. Rapp (2002)

[137] Zs. Nemeth,F. Käppeler, C. Theis, T. Belgya, and S.W. Yates, Ap. J.**426**, (1994) 357.

[138] K. Wisshak, F. Voss, C. Theis, F. Käppeler, K. Guber, L. Kazakov, N. Kornilov, and G. Reffo, Phys. Rev. C**54**, (1996) 1451.

[139] K. Wisshak, F. Voss, and F. Käppeler, Phys. Rev. C**54**, (1996) 2732.

Chapter 12

Curriculum vitae

Name:	Iris Dillmann
Geburtstag:	16.02.1978
Geburtsort:	Bad Homburg v.d.H./ Deutschland
Nationalität:	deutsch
Familienstand:	verheiratet

Schulausbildung:

1984-1988	Grundschule Usingen/ Deutschland
1988-1990	Förderstufe Usingen
1990-1997	Gymnasium Usingen
1997	Abitur (Leistungskurse Deutsch und Chemie)

Universitätsausbildung:

10/1997- 12/2002	Chemiestudium (Diplom) an der Universität Mainz/ Deutschland
4/2002- 12/2002	Diplomarbeit über "Kernspektroskopische Untersuchungen am N=82 r-Prozess 'Waiting-Point' Nuklid ^{130}Cd" am Institut für Kernchemie, Universität Mainz
1/2003-12/2006	Promotion an der Universität Basel bei F.-K. Thielemann und T. Rauscher
1/2003-2/2004	Experimentelle Arbeit am Institut für Kernchemie, Universität Mainz
3/2004-12/2006	Experimentelle Arbeit am Institut für Kernphysik, Forschungszentrum Karlsruhe